FRONT AND BACK CAPTURE
IN HIGH GRADIENT MAGNETIC SEPARATION

by

M. Hollingworth

A Thesis Submitted to the
Faculty of Graduate Studies and Research
in Partial Fulfilment of the Requirements for the Degree of
Master of Engineering.

Department of Mining and Metallurgical Engineering
McGill University
Montreal, Canada

ABSTRACT

A Frantz Isodynamic Separator was modified in order to carry out a single wire study of a longitudinal high gradient magnetic separator (hgms). Manganese dioxide and hematite were used under a variety of test conditions with the build-up profiles recorded photographically. Experiments using laboratory scale hgms were also carried out in conjunction with the single wire study.

It was seen that the Loading Number, N_L , predicts front and total capture very well using ε as a data fitted constant. The magnetic velocity to fluid velocity ratio, $\frac{V_M}{U_\infty}$, appeared to determine the relative amount of front to back capture. The variation in back capture profiles was qualitatively correlated with the flow characteristics in the wake behind the wire.

It was seen that a spaced matrix in a hgms caused up to twice the mass of material to be captured than on a closed matrix. It was suggested that the open matrix acted more closely to a matrix of single wires.

Résumé

On a modifié un séparateur isodynamique Frantz afin d'étudier dans un système à un fil les séparateurs magnétiques à haut gradient (SMHG) longitudinal. Des alimentations de dioxyde de manganèse et d'hématite furent employées pour déterminer photographiquement les profils de chargement sous différentes conditions d'opération. En parallèle à ces études, on a également complété des essais de concentration avec un SMHG de laboratoire.

On a observé que le nombre de chargement, N_L, prédit très bien la masse capturée frontale et totale, si ε est ajusté aux données expérimentales. Le rapport V_m/U_∞ déterminerait apparemment l'importance relative des captures frontale et arrière. On a pu également correler qualitativement les profils de capture arrière avec les caractéristiques hydrodynamiques du sillage à l'arrière du fil.

On a constaté qu'une matrice espacée pouvait récupérer jusqu'au double de la masse d'une matrice serrée, dans un SMHG. On a suggéré qu'une matrice espacée se comportait comme une matrice de fils isolés.

OBJECTIVE

Previous studies of high gradient magnetic separation (hgms) have led to such concepts as the dimensionless magnetic velocity to fluid velocity ratio, V_M/U_∞ (11), and the Loading Number, N_L, (2) both of which are of use in predicting conditions for particle capture and build-up. These groups were derived by making reasonable assumptions about capture but without any definite knowledge of the actual capture process on the wires.

Consequently, this work attempts to examine the build-up process on a single wire longitudinal hgms and determine photographically the capture mechanisms and profiles under various test conditions.

TABLE OF CONTENTS

NOMENCLATURE

SECTION: 2.1 and 2.2

A	perturbation term for the magnetic field around a wire
a	wire radius
a_n	radius to nth particle layer
b	particle radius
C	fluid constant
$F = F_L$	volumetric packing fraction
Fmax	maximum build-up to wire ratio
$Ha = Ho$	applied magnetic field
K	Stokes number
Kf	universal fibre parameter
L	matrix length
L/Lm	ratio of loading to maximum possible wire loading
Mw	wire magnetisation. (emu/cm^3)
Ni	number of particles entering the separator
No	number of particles leaving the separator
N_L	loading number
$r_a = \frac{r}{a}$	relative particle accumulation radius
Rc	wire capture radius/wire radius
S	diameter of the major wire axis
Sn	width of fibre to the nth particle layer
U	outer flow velocity
V	build-up volume
$Vo = U_\infty$	free stream velocity
V_M	"magnetic velocity"
V_W	volume of the wire

SECTION 2.3

C_D	drag coefficients
d	diameter of the wire
$L^* = L/R$	length of wake to radius of wire ratio
n	frequency of vortex shedding
Re_w	Reynolds number of the wire
S	Strouhal number

v	flow velocity
γ_A	area load, cm^2 of particles/cm^2 of fully loaded wire
γ_M	mass loading, g of particles/g of fully loaded wire
γ_V	volume loading, cm^3 of particles/cm^3 of fully loaded wire
σ	nominal boundary layer thickness
σ_{99}	σ over which flow has regained 99% of U
ε	packing fraction
ξ	A capture radius for the mechanical entrainment of particles
η	fluid viscosity (absolute), g/cm-s
θ_A	angle of boundary layer separation
κ	volume particle susceptibility, emu/cm^3 - O_e
μ	magnetic permeability
υ	fluid viscocity (Kinematic), cm^2/s

LIST OF FIGURES

LIST OF TABLES

I. INTRODUCTION

High Gradient Magnetic Separation (hgms) utilizes a filamentary matrix of ferromagnetic material magnetised by a background field to capture particles from a flowing fluid. The high fields and gradients resulting along the edges of the filaments provide very effective regions for trapping even fine weakly magnetic particles (Figure 1).

The use of hgms is becoming more widespread in industry and a great variety of applications have been tested on a laboratory and pilot-plant scale.(3) For example:

a) The treatment of both municipal and industrial waste waters.(4,5)

b) Treatment of hot rolling mill scale and cold rolling mill emulsion has been successfully tested and has been applied successfully in a number of Japanese steel mills.

c) In polishing of recirculating waters in power and steam generation systems. Hgms is used here because it can operate under conditions of high temperature and pressure as well as a hostile chemical environment. By reducing the metal oxide content of these waters, critical surfaces within the system are protected from particulate build-up and good heat transfer is maintained.

d) Magnetic seeding and flocculation of municipal wastes which permits removal of non-magnetic material from water.

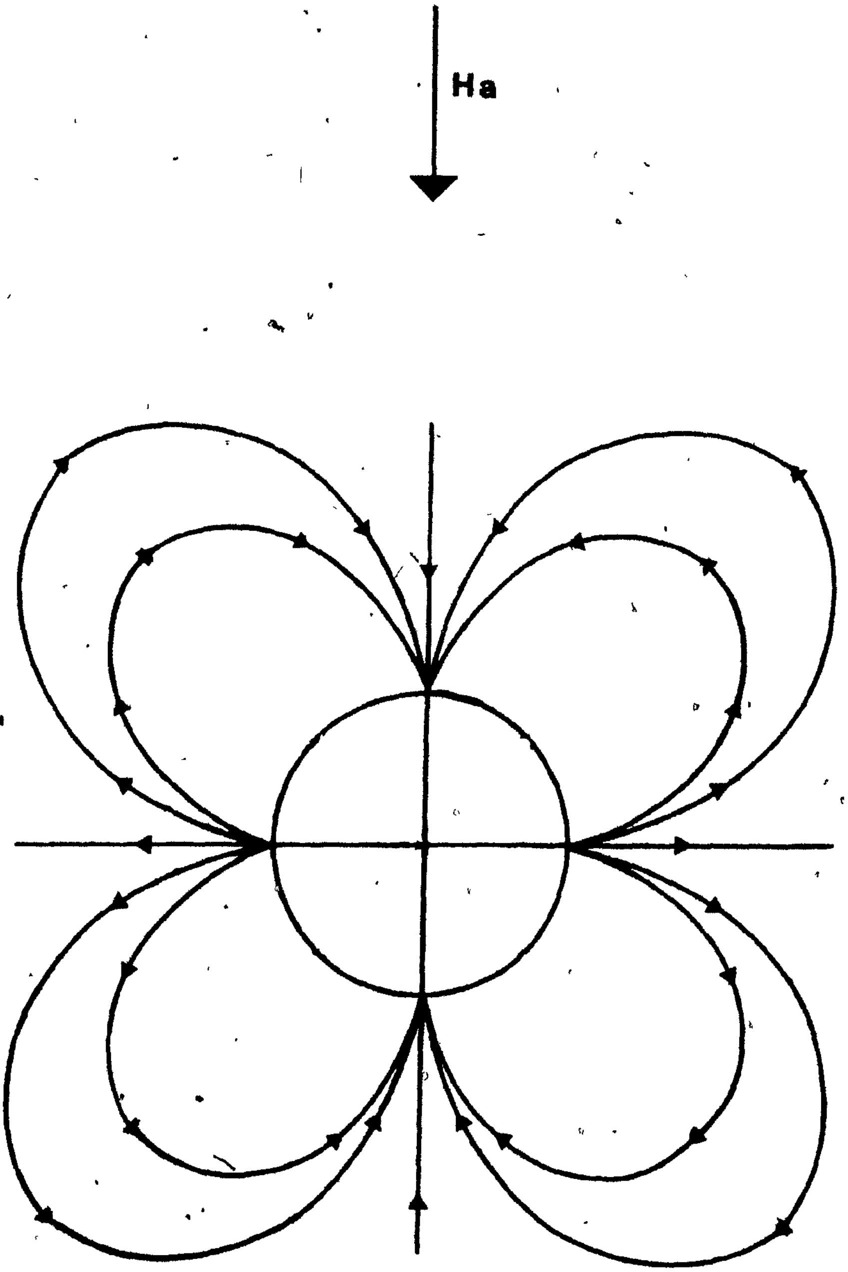

Fig. 1   Magnetic force contours for an infinite ferromagnetic cylinder immersed in a uniform magnetic field. The contours indicate the forces which act on a small paramagnetic particle in the region surrounding the cylinder.

e) The removal of the discolouring iron stained anataze (TiO_2) from Kaolin clay in order to obtain a high brightness.(6,7)

The above mentioned have all been examples of batch (cyclic) type hgms where the field has to be switched off in order to recover the magnetic material.

A carousel-type hgms has enabled a fully continuous separator to be developed which is generally used where slurries contain too large a fraction of magnetic particles to be efficiently processed in a cyclic device without a large decrease in duty cycle. In this device, sections of matrix rotate through a magnetic field region and a flushing station in turn, so avoiding the necessity for the magnet to be turned off (Figure 2).

Applications of the continuous hgms include beneficiation of weakly magnetic iron ores such as hematite, goethite and iron silicates. Also, 75% of the sulphur content of coal may be removed by hgms, due to much of the sulphur forming paramagnetic iron compounds in the coal.(3)

The fact that hgms requires little floor space, is simple to maintain, has a low energy requirement and is easily scaled-up from a small laboratory device ensures that the separation technique will be increasingly used for a wide variety of purposes in the near future.

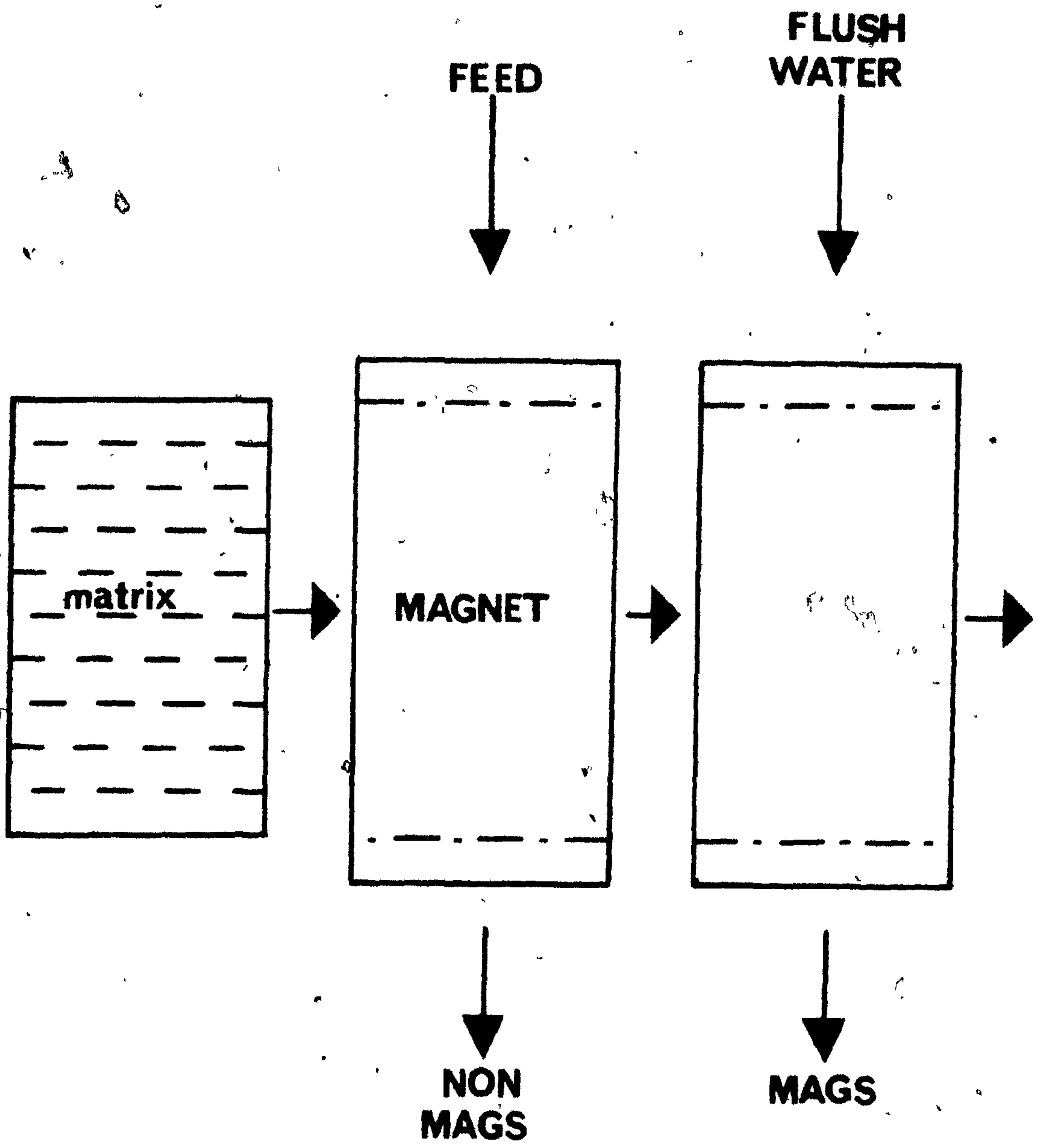

Fig.2 A Diagrammatic Representation of a Carousel-Type H.G.M.S.

II. BACKGROUND THEORY

Accompanying the development of equipment and applications of hgms, has been a considerable mathematical modelling effort. These models may be divided into two categories:

a) Trajectory (or dynamic) models, which involve predictions of particle trajectories and capture radii.

b) Build-up (or static) models which predict the extent of build-up of these particles once they have reached the fibre.

Obviously a complete description of behaviour in the system requires a combination of these approaches. Consequently the following will include both, in addition to a description of the fluid flow about a cylindrical wire.

2.1 Trajectory Models

When studying particle motion under magnetic forces, Watson(1) adapted Zebel's(9) work on electrostatic precipitation. This was possible because magnetic and electrical energy interact with a body in an analogous manner. By considering only magnetic and Stokesian fluid drag forces, he found that the trajectories of paramagnetic particles in the vicinity of the wire were dependent on the parameter, $\frac{V_M}{U_\infty}$, where V_M is the 'magnetic velocity' i.e. the terminal velocity of the spherical particle in a stationary fluid when acted on by a uniform magnetic field gradient, and U_∞ is the undisturbed fluid velocity far from the wire.

The ratio is given by (in the cgs system):

$$V_M/U_\infty = \frac{4b^2 \; \kappa \; H_a^2 \; A}{9a \; \eta \; U_\infty} \tag{1}$$

where b = particle radius, κ = volume susceptibility, H_a = applied magnetic field, A = a perturbation term $(1-2\pi\, M_W/H_a)$, a = wire radius and η = absolute fluid viscosity.

The concept of a limiting particle trajectory is used in defining, Rc, a dimensionless capture radius. This assures that all particles passing within a capture cross-section of 2Rca where a is the wire radius, will be ultimately captured by the fibre (Figure 3).

However, Watson's work did not take into account a decreasing capture radius as particle build-up occured on the wire. This was accounted for by Luborsky and Drummond$^{(10)}$ who also confirmed that the particle trajectory was dependent on V_M/U_∞ .

Watson determined that the ratio of particles leaving a separator to those entering could be expressed as (for a clean wire):

$$\frac{N_o}{N_i} = \exp\left(\frac{-4F\ Rc L}{3\pi a}\right) \tag{2}$$

where F = volumetric packing fraction , L = length of matrix, while Luborsky and Drummond, considering the more practical ribbon - like fibre rather than cylndrical ones, obtained the expression:

$$\frac{N_o}{N_i} = \exp\left(\frac{-f\ {}^{F}L}{3S}\ (Rc + \xi)\right) \tag{3}$$

where S = diameter of the major wire axis, f = capture efficiency and ξ = capture radius for mechanical entrainment of particles, f and ξ being data fitted constants.

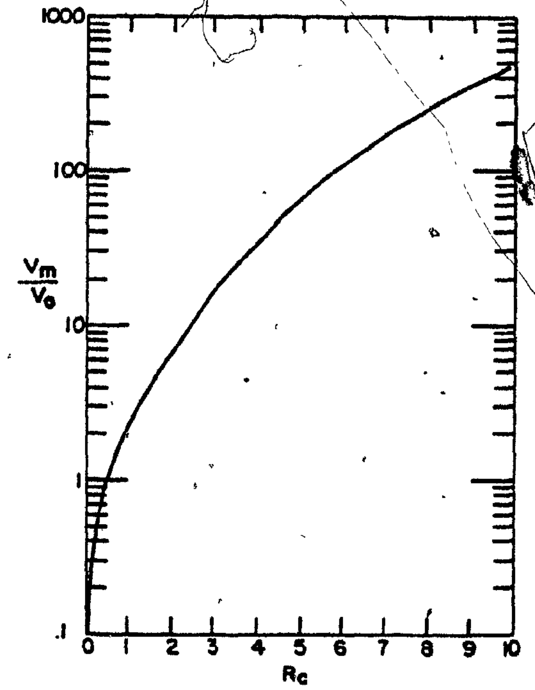

Fig.3 Watson's Dependence of Rc on V_M/U_∞ (V_M/V_0).

Luborsky and Drummond's approach was criticized by Watson as they had not considered the stability of the accumulated particles on the wire. In later work$^{(11)}$ Watson took this into account which produced a small improvement in the correlation between experimental and theoretical results.

Cummings, Prieve and Powers$^{(12)}$ approached the study assuming creeping flow rather than potential flow. They found the value of Rc was considerably reduced due to the effect of the hydrodynamic force being felt by the particles further upstream. The fact that the no-slip criterion is associated with creeping flows means a physically more correct model is obtained than the previous ones.

Particle trajectories predicted by using both potential and creeping flow are seen in Figure 4.

At low Reynolds numbers, Clarkson, Kelland and King$^{(13)}$ accounted for the viscous and inertial fluid body terms by superimposing a boundary layer on the solution for potential flow with elliptical fibre shapes. By also considering gravitational and near field magnetic effects, a recovery equation was developed as:

$$\frac{N_o}{N_i} = \exp\left(\frac{-2 \quad Kf \quad F \quad RcL}{\pi \ ab'}\right) \qquad (4)$$

where Kf, a universal fibre parameter, allowed for random fibre-fibre orientation effects; $\pi ab'$ is the cross-sectional area of the fibre.

After fitting Kf, the analysis produced good experimental and theoretical correlation $^{(14)}$. They concluded that the assumption of potential flow was acceptable for particle sizes greater than 5μm

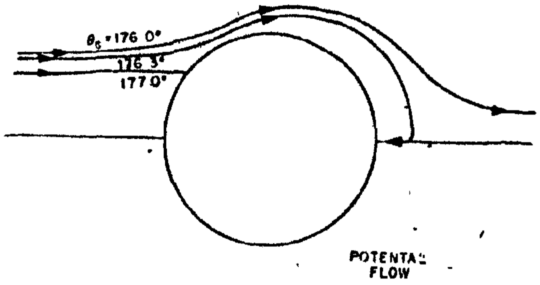

Particle trajectories for potential flow. Note that the trajectories are nearly flat until very near the collector.

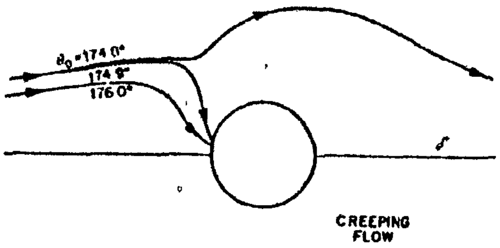

Particle trajectories for creeping flow. Note that the trajectories diverge from the axis much farther upstream than in potential flow.

Fig.4 Cummings, Prieve and Powers predicted that capture could occur on the back of the wire if the fluid flow was considered to be potential flow. In a H.G.M.S. creeping flow must be assumed in close proximity to the wires a condition under which they predicted no back capture to occur.

providing there was little physical trapping. Below this size, the shielding effects of the boundary layer on the particles from the otherwise large near-wall drag forces of potential flow become increasingly significant and should be included.

Simons, Lawson and Treat(15) examined the dynamics of particle attraction about a cylindrical wire assuming potential flow. They considered inertial effects, gravitational effects and near field magnetic forces and established conditions where the aforementioned could be neglected in calculating the capture cross-section (Rc). They found:

a) For a Stokes number ($K = \frac{2b^2 \rho p U_\infty}{9a\eta}$), a measure of particle inertia to viscous flow greater than unity, inertia could be accounted for. For small K(< 1.0) gravity may be neglected.

b) If $\frac{V_M}{U_\infty} < 10$ and for low K, inclusion of a short range magnetic force term has a positive and increasing effect on Rc.

Within these limits they found that the relationship of Rc and $\frac{V_M}{U_\infty}$ is correct as described by Watson.

In their many calculated trajectories for particles around the wire, back capture was never obtained (Figure 5). It was assumed this was due to the particles having to pass through the repulsive sector where they were forced too far from the wire to be caught at the back.

Stekly and Minervini(16) studied the shape effects of cylindrical and elliptical fibres on Rc and determined that it was the projected frontal area of the wire and not the aspect ratio of the major

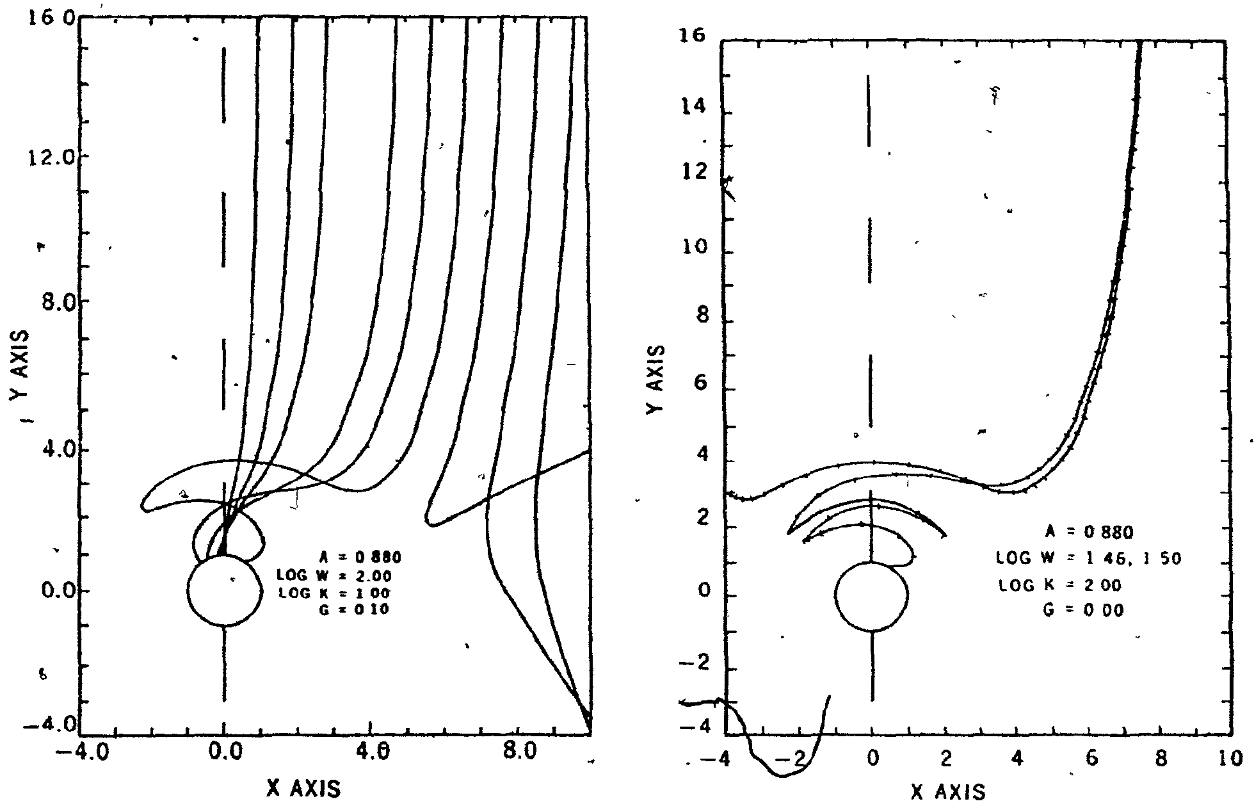

Fig.5 Simons, Lawson and Treat examined 5 µm particle trajectories in air and found that although the particles oscillated enormously around the wire, under no conditions studied did back capture occur,

to minor axis that affected Rc. This conclusion, although applied to cylindrical wires may be applied to filamentary type wires as it suggests only the wire dimensions perpendicular to the field and flow affect the capture cross-section.

They determined that with strong magnetic interaction, there were regions about the elliptical wires where capture could and could not occur. A large region behind the wire is seen where particles would be captured (Figure 6) if they could be transported there.

In a study by Cummings, Himmelblau, Oberteuffer and Powers(17) equations were developed to describe the capture of small paramagnetic particles on bare wires at low flow velocities. They considered inertial magnetic fluid and gravitational forces, arriving at seven dimensionless groups to describe the system. One such group, N_M, used to describe the magnetic field strength, was defined as:

$$N_M = \frac{\mu \quad H_o^2}{\rho f \quad U_\infty^2}$$

where μ = magnetic permeability, H_o = field strength, ρf = fluid density and U_∞ = flow velocity. This group was varied in order to achieve various capture conditions. By drawing out the calculated particle trajectories (Figure 7) it is seen that back capture is feasible under certain conditions.

Birss, Dennis and Gerber(18) carried out a single wire study of particle capture for a non-axial configuration. The situation can be conveniently described in cylindrical co-ordinates where a wire is placed along the Z-axis and an external field (H_o) is applied in the

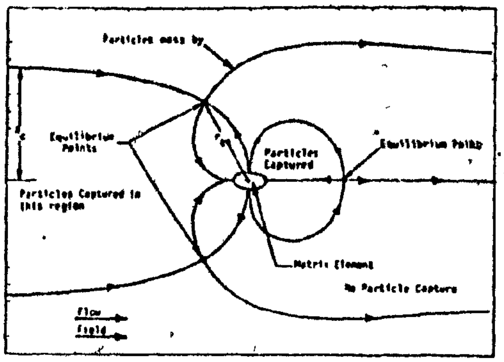

Particle Capture Regions in a Strong Interaction Showing Three Equilibrium Points.

Fig.6 Stekly And Minervini, in their study of the shape effect of the wire on capture, determined that particles would be caught at the back of the wire.

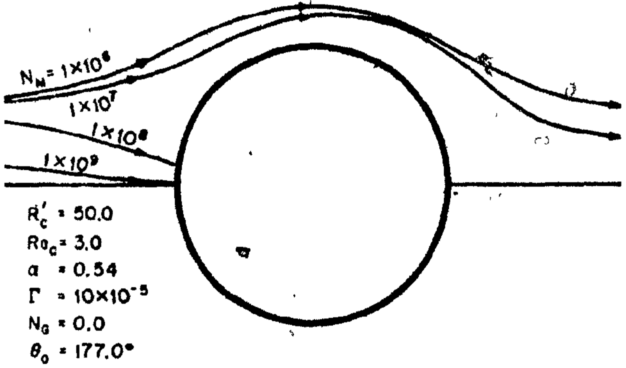

Effect of magnetic field strength on particle trajectories. All particles started at the same location.

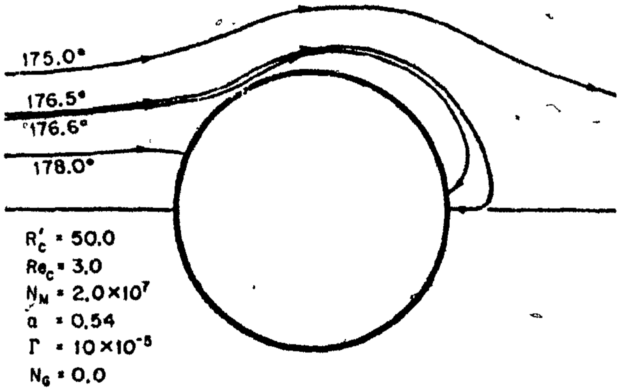

Fig. 6. Back side capture.

Fig.7 Conditions in both diagrams may be seen to be similar.It would appear that the starting position of the particle would determine whether it reached the back of the wire.

(rθ) - plane at the angle θ = 0. A fluid flows with a velocity, V_0 toward the wire along a direction which lies in the (rθ) plane, making an angle α with the magnetic field (Figure 8). The results show that the capture radius, Rc can be expressed in a simple form as:

$$Rc = C_1 \sqrt[3]{|V_M/V_\infty|} - Co \qquad (5)$$

where C_1 and C_o are constants independent of α.

The calculated trajectories show that for high values of α, capture occurs on both sides of the wire, whereas for low values of α (and in particular α = 0) the capture occurs only on the upstream side of the wire (α = 0, represents the configuration of the longitudinal hgms considered here). However, computer simulation of particles brought out of their expected upstream positions into the void regions around the wire (cf Luborsky and Drummond$^{(11)}$) does allow back capture to occur at position α = 0 as shown in Figure 9.

An investigation by Hayashi and Uchiyama$^{(19)}$ considers the particle trajectory and capture efficiency for a two-layer high gradient filter. By considering the magnetic and drag forces only, trajectories of particles arriving at the second layer of wires are changed substantially from those arriving at the front wires, due to the disturbances caused by the front wire (Figure 10). However, it was found that the capture radius was scarcely changed by the front wires providing the back wire was not masked geometrically by the first.

In an abstract published by Watson$^{(20)}$, he discusses the effect of the vortices at the rear of the wire on the build-up. In the region

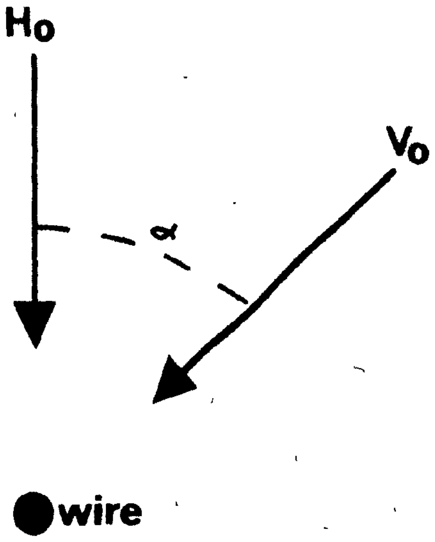

Fig.8 The Layout Of Birss , Dennis And Gerber's H.G.M.S. Study.

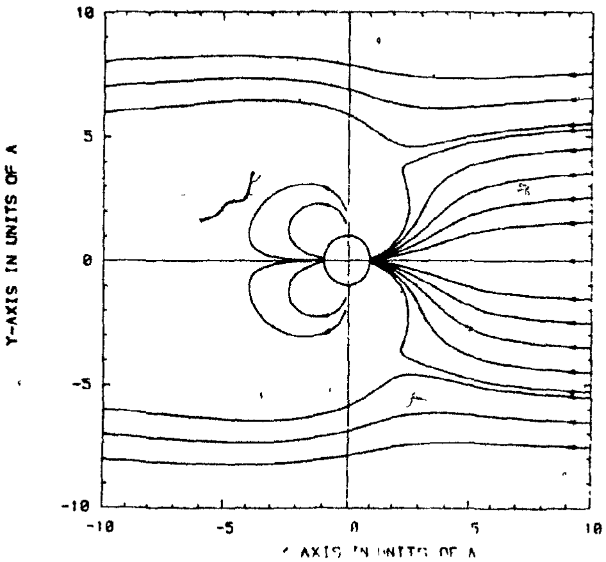

Fig.9 . The Resulting Trajectories of the Particles.Note the Back Capture Occurs Only if Particles Reach the Void Regions at the Side of the Wire.

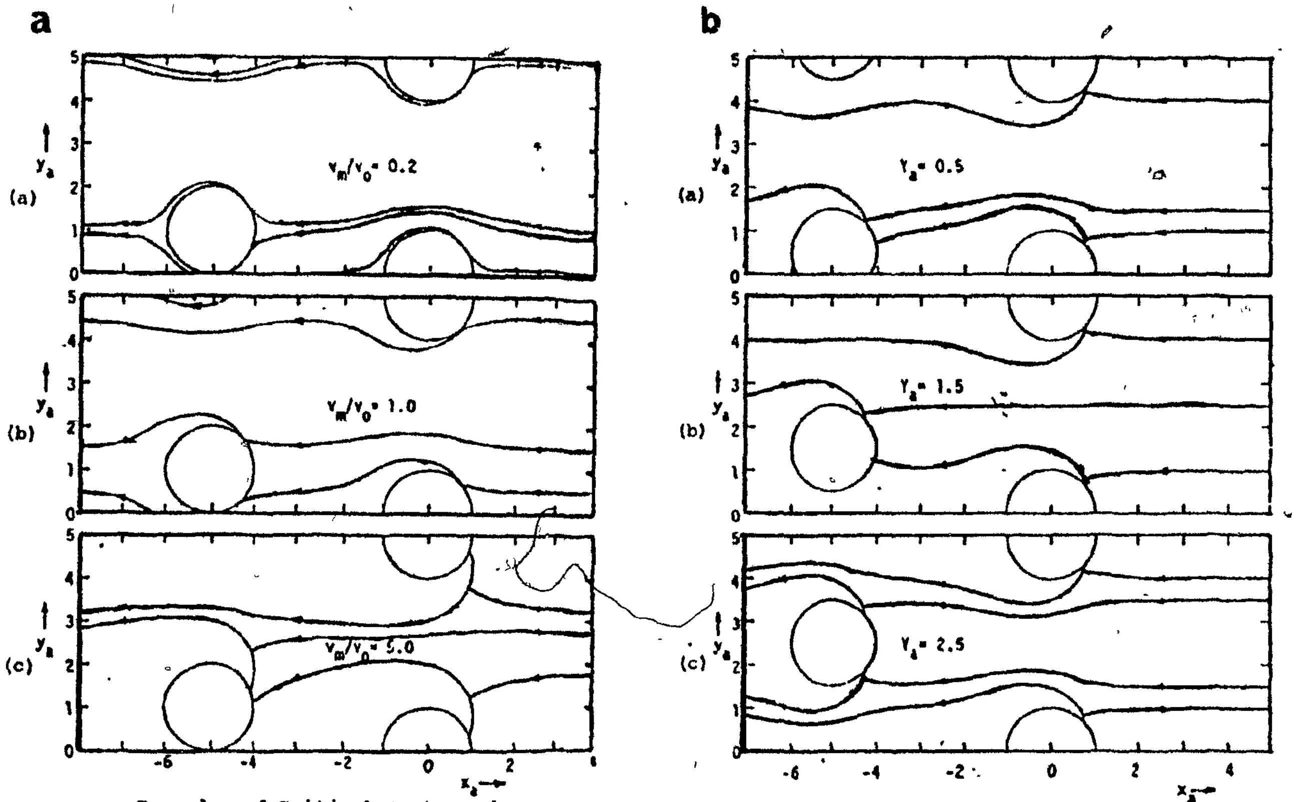

Examples of Critical Trajectories ($Y_a = 1$ for every figure)

Examples of Critical Trajectories ($v_m/v_0 = 2$ for every figure)

Fig.10

a/ Shows the effect of increased V_M/V_o on particle trajectories around many wires.

b/ Shows the effect of increasing Ya on the trajectories , where Y = the displacement in the Y-axis and a = the wire radius.

of Reynolds Number $6 < Re < 30$, a large amount of downstream magnetic capture was predicted due to the standing vortices at the downstream side of the wire.

If particles are flowing with the fluid of velocity V_o far from the wire, capture only occurs on the front side of the wire. No particle trajectories take the particles to the rear of the wire unless K(Stokes Number) ≈ 1.0. Watson assumes $K < 1.0$ based on the large fields used in the koalin industry. If this is the case, particles will not be caught at the back of the wire due to two general situations:

i) If $\frac{V_M}{V_o} > 1.0$, the repulsive sector around the wire moves the particles too far from the wire to be captured.

ii) If $\frac{V_M}{V_o} < 0.1$, the magnetic forces do not repel the particles far from the wire but at the fluid separation point the particles are swept around the vortex region and are not captured.

2.2 Longitudinal Hgms Build-up Models

The trajectory models, as described in the previous section, produce initial capture cross-sections with all particles entering this area assumed to be captured on the wire. Build-up models predict the profile of the accumulated material. Knowledge of the profile is necessary as it has an effect on the capture cross-section of particles approaching partially loaded wires. The second function of the build-up models is to determine the maximum loading capability of a wire and consequently the total mass recovery potential of the hgms device.

Luborsky and Drummond's early work(10) involved choosing suitable profiles and subsequently determining the effect of the profiles on particle trajectories and the capture cross-section. They considered two possible profiles (Figure 11) based on the theoretical observations of Himmelblau(21). The fluid was assumed to see a changing radius "a_n" for each layer of build-up 'n' such that:

$$a_n = a + 2bn$$

where a = bare wire radius and b = particle radius. They determined that Rc decreased as:

$$Rc = \frac{V_M}{2U_\infty}\left(\frac{a}{a_n}\right)^2 \qquad (6)$$

for case a) provided $\frac{V_M}{U_\infty} \leqslant 2^{\frac{1}{2}} \left(\frac{a_n}{a}\right)^2$ and as:

$$Rc = \frac{V_M}{2U_\infty}\left(\frac{a}{a_n}\right)^3 \quad \text{for case b)} \qquad (7)$$

To achieve reasonable experimental agreement with the theory, they introduced 'f' and 'ξ', as described previously for fibre efficiency and mechanical trapping respectively. In their later study they made two new assumptions in order to limit the mode of particle capture on the wire. On the upstream side of the ribbon-like wires the build-up was considered stable provided a) the magnetic force on a particle was radially attractive, and b) the magnetic force exceeded the Stokesian drag tangentially. The outer flow velocity was reduced by a value of $\frac{b}{\sigma_{99}}$ (σ_{99} = boundary layer thickness) to account for a decreased velocity in that boundary layer. σ_{99} was assumed to be greater than 2b and it

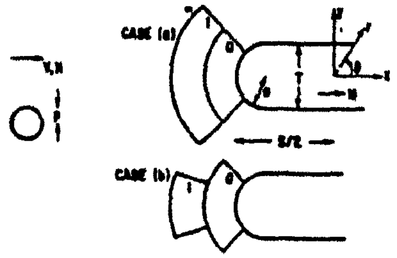

Schematic of ribbon-like fiber, infinite in z-direction, with approaching particle, showing two possible modes of build-up of particle layers; case (a) and (b).

Fig.11 The Two Starting Profiles Used By Luborsky and Drummond.

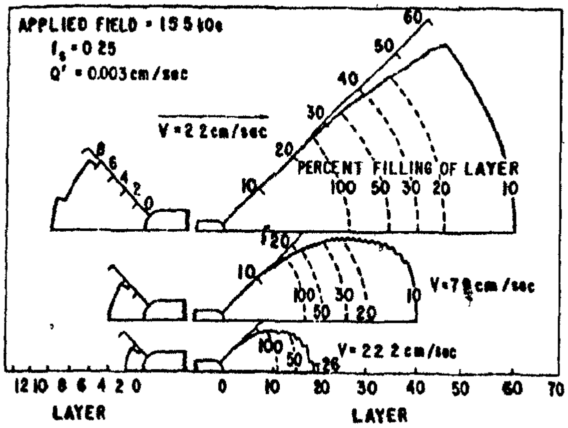

Buildup of particles calculated for (a) upstream and (b) downstream edge of fiber [half scale of (a)].

Fig.12 Luborsky and Drummond predicted large amounts of capture at the back of the wire.

was approximated over the 90° region of interest by (Schlicting[22]).

$$\sigma_{99} = \pi^{\frac{1}{2}} \left(\frac{\pi \quad a_n}{\mu \quad \rho f} \right) \tag{8}$$

Thus giving the fluid sheer force as:

$$b \quad u^{3/2} \quad \rho f \quad \eta^{\frac{1}{2}} \tag{9}$$

where η = viscosity, ρf = density of the fluid, b = particle radius and u = flow velocity.

The critical angles, where the components of tangential force are exactly balanced, were then calculated for each successive layer of particles; the loci of these angles describing the ultimate build-up profile of the captured material.

By balancing the radial components of the magnetic and shear forces, back capture was also modelled in a similar fashion. It was suggested that the particles arrived at the back of the wire either by being swept off the front edge of the build-up or by being caught up in the turbulent wake of the fiber. It was assumed that the capture of the particles occured with the same geometry as on the upstream side. Similar criteria to those on the upstream edge were then applied to determine the fraction of the particles remaining and their configuration. In this case the boundary layer thickness is taken as equivalent to that at the end of a flat plate i.e.:

$$\sigma_{99} = 5(\eta \; Sn/V_\rho)^{\frac{1}{2}} \tag{10}$$

where Sn, the width of the ribbon, is a function of n, given as $Sn = S + 2nb$ where b = particle radius.

The results showed that a much greater amount of retained material could be expected at the downstream side of the wire than at the upstream (Figure 12). The prediction of large amounts of back capture was unexpected and made the method seem inadequate for such calculations, as no observation had been made of such extensive back build-up.

In a series of papers, Watson (1,2,3) determined the initial capture radius, Rc, to be solely dependent on $\frac{V_M}{U_\infty}$ and that it would remain constant as the volume of build-up increased. This is in contrast to the assumptions of Luborsky and Drummond. Using a numerical approach, Watson considered a tangential balance of magnetic Stokesian drag and friction- like dissipative forces in order to determine whether a particle would remain or be swept away from the wire. By considering this, over the whole profile, the probability of retention, P, and a total effective capture cross-section 2 Rc P could thus be determined. He showed that the critical value of $\frac{V_M}{U_\infty}$ would determine whether the capture cross-section increased or remained constant:

i) Below $\frac{V_M}{U_\infty} = 1$, and with a small volume of captured material, the value of Rc was small but would tend to increase as build-up progressed.

ii) Above $\frac{V_M}{U_\infty} = 1$, and with greater amounts of captured material, the value of Rc would remain constant.

Recently Watson$^{(24)}$ added several modifications to allow growth to proceed non-uniformly, by allowing growth to occur independent of its surroundings starting at a bare wire condition. He also used the boundary layer adjustment of Luborsky and Drummond to calculate the probability of retention in each surface element. This created a new profile for the build-up and a new flow distribution over it. The model predicted a continuous fan-shaped build-up extending to the area of repulsive radial magnetic force where a final rapid development of growth was suggested (Figure 13).

In this modified model, once again the effective Rc showed an initial increase at low $\frac{V_M}{U_\infty}$ and as the volume, V_M, of build-up increased, the effective Rc declined much as in Luborsky and Drummond's model and gave a similar relationship:

$$Rc_{eff} = \frac{Rc_{initial}}{\left(1 + \frac{4V}{V_w}\right)} \qquad \text{where } V_w = \text{volume of wire} \qquad (11)$$

From Figure 13, it is seen that Watson's model supports a fan-shaped build-up profile and therefore supports the model of Luborsky and Drummond (10).

In addition to investigating the effect of wire shape on Rc, Stekly and Minervini(16) also considered material accumulation on the upstream side of the wire. By assuming the profile build-up was elliptical they deduced that for both circular and elliptical wires the capture cross-section, Rc, shows an initial decrease followed by a levelling off as build-up progresses. The fully loaded profile of the wire was not considered.

The approach of Clarkson and Kelland contrasts markedly with that above, in that Rc is assumed to be zero at maximum build-up volume. While also assuming back capture was zero, this allowed for the influence of wire loading by adjusting the flow patterns (to an elliptical shape) on the upstream side of the wire. The resulting capture radii were allowed to decrease exponentially toward zero as a function of $\frac{L}{L_M}$, where L is the material capture and L_M = maximum possible material captured.

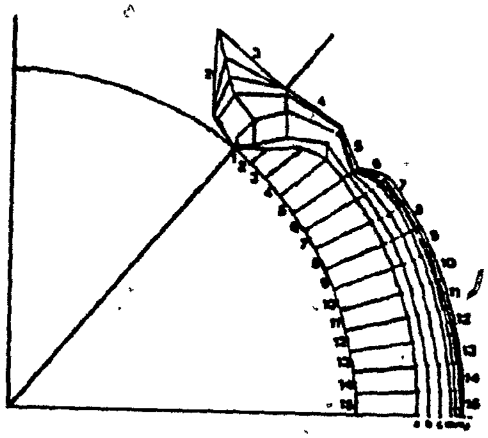

Fig. 13 Watson's Computed Surfaces For Growth Model.

The work of Friedlaender and his various associates has been in producing photographic evidence of build-up profiles and accumulation data for the three orientations of flow, field and wire of interest (Figure 14). In their early work, Friedlaender et al (25-28) used a hot wire anemometer to determine the build-up of particles on the wire at a specific rate by correlating build-up with heat loss from the wire. At the same time photographs were taken. Very uneven build-up was observed. A lack of closely sized material plus difficulties in obtaining clear photographs prevented comparison with the available models. Despite this, fan-shaped build-up rather than elliptical build-up was observed on the upstream side of the wire and some downstream collection occurred at high flow rates.

By modifying this equipment to employ the use of a video system, Friedlaender et al developed a system with much improved image resolution and one which was capable of continuous monitoring of particle accumulation on single wires (29-31).

Downstream capture was seen to increase with velocity, U_∞ and passed through a maximum while the upstream relative saturation accumulation radius, Ras, decreased continually with increased U_∞ (Figure 15). It may also be noticed that the sum of front and back Ras was found to be largely independent of fluid velocity over the range considered. This would seem to imply that recovery is not a function of U_∞, a fact not supported by published operating data.

Using a similar model to Luborsky and Drummond, Lui, Oak and Lin(32) developed arguements for neglecting the decrease in capture radius with increasing wire loading. Their model determined that maximum build-up volume was usually reached before an appreciably large

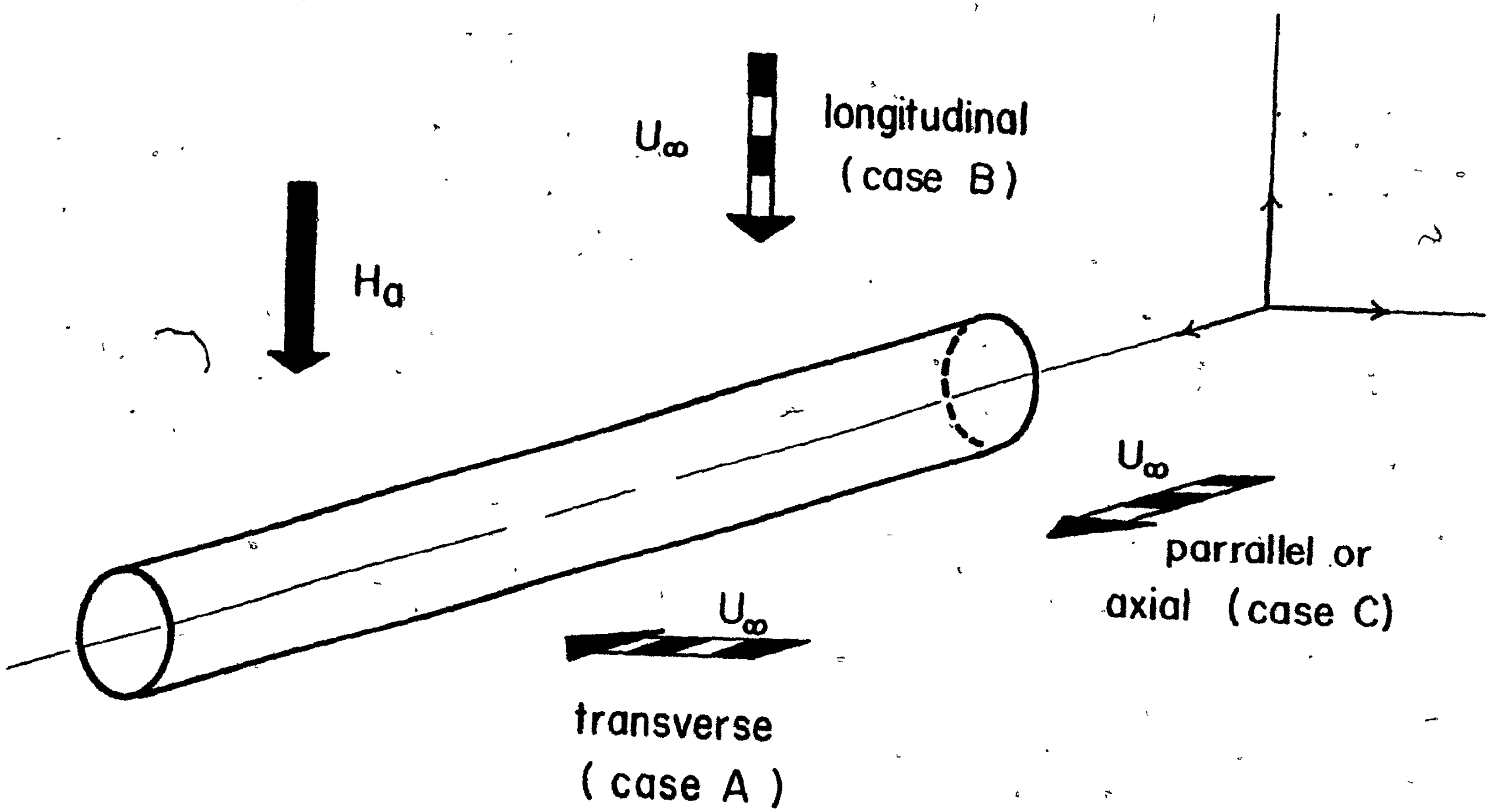

Fig.14 Principal Orientations Of H.G.M.S.

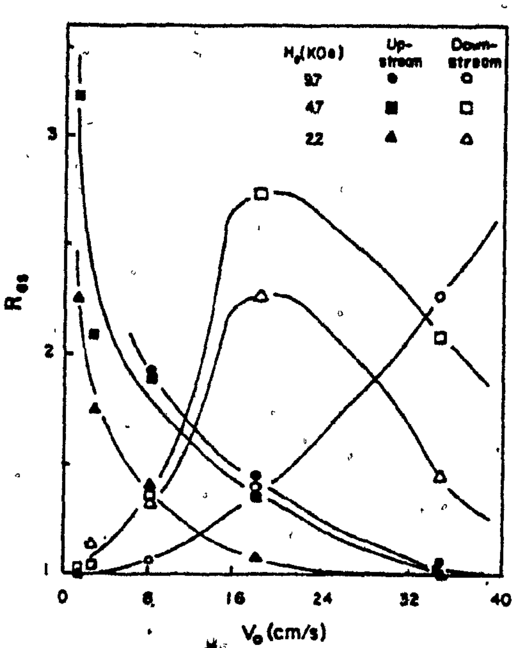

Saturation value of relative accumulation radius R_{as} of upstream and downstream collection is plotted versus slurry velocity $u_0(Mn_2P_2O_7, c = 0.4$ g/l).

Fig.15 R_{as} as a Function of U for Upstream and Downstream Build-up.

reduction in Rc occurred(cf Clarkson and Kelland).

Two cases of relative particle-wire size were considered in conjunction with the fluid drag forces:

i) $\frac{b}{a} \simeq 1$ where b = particle radius

ii) $\frac{b}{a} << 1$ a = wire radius

For large particles, case i) Stokesian drag was assumed as the carrier fluid may be presumed to have passed through the interstices of the build-up. From this approach, they obtained a relationship between the maximum relative build-up volume (f_{max}) and $\frac{V_M}{U_\infty}$ such that:

$$f_{max} \propto \left(\frac{V_M}{U_\infty}\right) \qquad \text{where } \frac{V_M}{U_\infty} \text{ has a minimum value of .5}$$

For case ii) Lui et al used an averaged boundary layer, similar to Luborsky and Drummond, and showed:

$$f_{max} \propto \left(\frac{V_M}{U_\infty}\right)^{.8} \propto \left(\frac{\sigma}{b}\right)^{.8} \qquad \text{where } \sigma = \sigma_{99} = \text{boundary layer thickness} \tag{12}$$

For case i) only, it was shown that the change in capture radii with build-up volume can be neglected since the capability of the wire matrix to capture particles remains high and practically unchanged up to build-up saturation. The effects of particle size, density and magnetic susceptibility were accounted for by considering the magnetic velocity distribution of the feed stream (cumulative weight percent vs. magnetic velocity). If $F(V_M)$ is the function describing the cumulative weight fraction of feed with magnetic velocity less than V_M, then $1 - F(V_M)$ corresponds to the fraction captured when subjected to the condition that all particles with a greater V_M are retained in the filter. This V_M is specified by the equilibrium wire loading (Figure 16).

Consequently, the total weight fraction received by the separator is determined by numerically integrating 1 - $F(V_M)$ for increments of feed.

Although Lui et al claim their approach is valid for all values of $\frac{V_M}{U_\infty}$, the range tested experimentally was always greater than 1.0. Thus, for instance, the postulation of a minimum value of $\frac{V_M}{U_\infty} = 0.5$ has not been tested.

By considering the magnetic, fluid shear and Blasius type forces acting on a single particle on the upstream side of a wire, Nesset and Finch$^{(2)}$ determined that:

$$(r_a)^2 = \frac{r}{a}^2 = \left\{ \frac{2b \quad Ha \quad \kappa \quad A}{\rho f \quad U_\infty^{3/2} \quad \nu^{1/2} \quad a^{1/2}} \right\} \quad \frac{1}{C}^{4/5} \qquad (13)$$

where r_a = relative particle accumulation radius A = field perturbation term = $\frac{2 M_W}{Ha}$ for cylinders perpendicular to Ha, M_W = the wire magnetisation, C = fluid constant = 2.5.

This may be rearranged to:

$$r_a^2 = \left(N_L \quad \frac{1}{C} \right)^{4/5} \qquad (14)$$

where:

$$N_L = \frac{2b \quad Ha^2 \quad \kappa \quad A}{\rho f \quad U_\infty^{3/2} \quad \nu^{1/2} \quad a^{1/2}} \qquad \text{(dimensionless)} \qquad (15)$$

and was termed the Loading Number. This represents the ratio of magnetic to shear forces at maximum build-up. The approach used was unique in that Blasius-type fluid shear is considered on particles at the bottom of an expanding cylinder as build-up progresses.

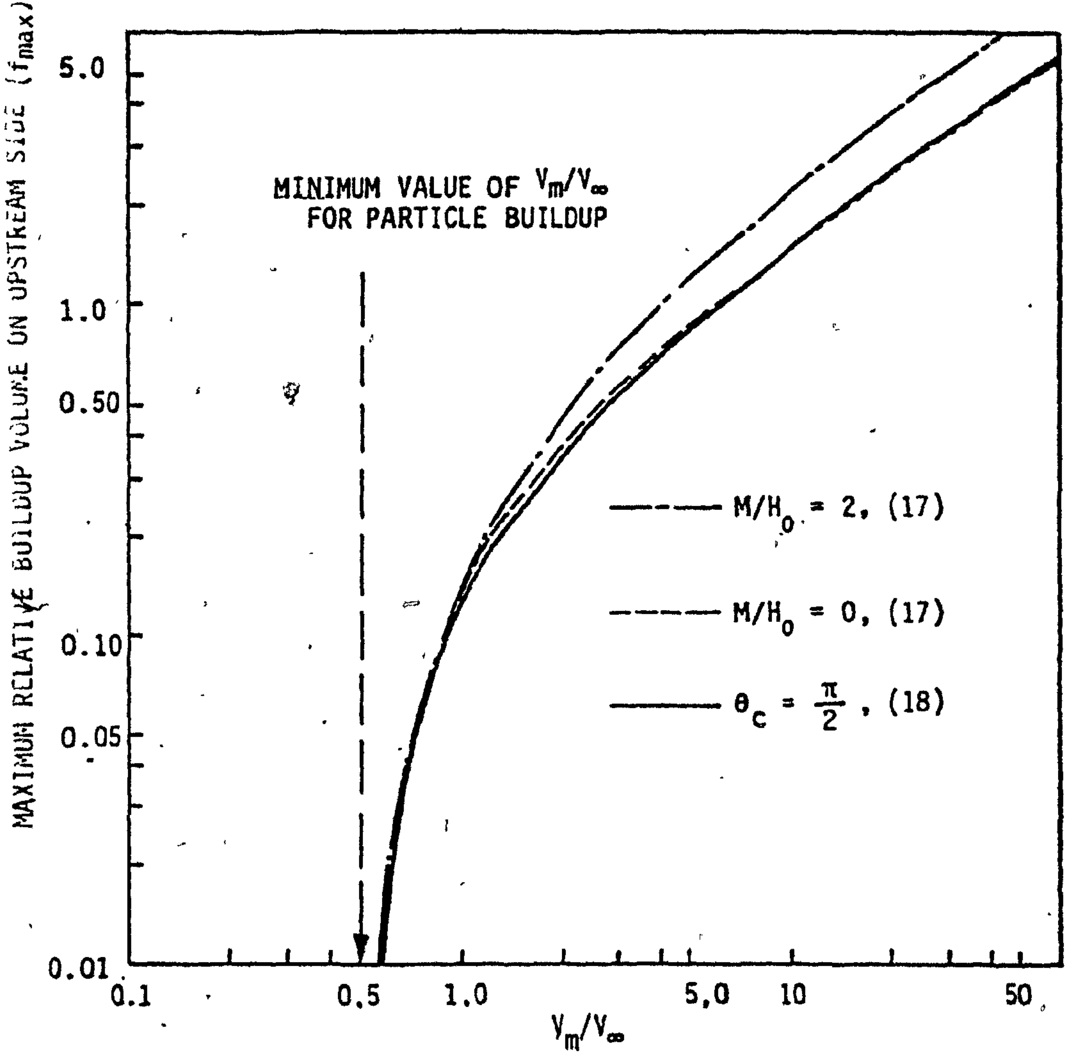

Fig.16 Lui et al's maximum relative build-up volume (Fmax) as a function of V_M/v_∞.

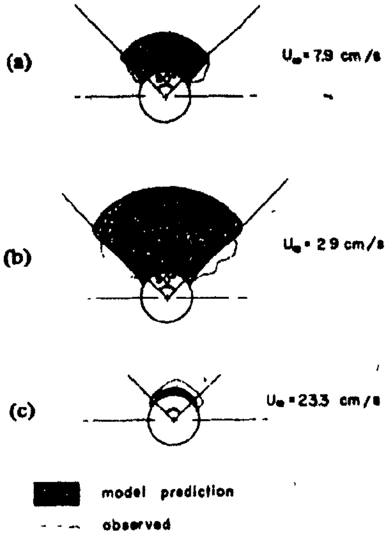

Fig.17 $Mn_2P_2O_7$ Upstream Build-up Profile , Measured From Fig.40 And Compared With The Predicted Build-up Profile Of Nesset(34).

The work consequently suggested that the loading of the wire could be quantified by just one dimensionless group, N_L. Experimental work carried out by the authors$^{(33)}$ supported this claim. In addition, the upstream build-up profiles predicted by Nesset and Finch appear to agree with those observed by Friedlaender et al (Figure 17)$^{(34)}$.

Assuming build-up occurs over the front 90^0 of the wire, the nominal build-up volume per unit length of wire, V_B, is given by:

$$V_B = \frac{\pi r^2}{4} - \frac{\pi a^2}{4} \tag{16}$$

This gives a nominal build-up volume to wire volume ratio as:

$$\frac{V_B}{\pi a^2} = \frac{\pi(r^2 - a^2)}{4\pi\ a^2} = \frac{1}{4}\ (r_a{}^2 - 1) \tag{17}$$

Converting from nominal to actual volume, γ_V, requires a packing fraction,

Therefore,

$$\gamma_V = \frac{\varepsilon}{4}\ (r_a{}^2 - 1) \tag{18}$$

On a mass basis this becomes

$$\gamma_M = \gamma_V \cdot \frac{\rho_p}{\rho_w} \tag{19}$$

where ρ_w and ρ_p are the wire and particle densities respectively.

By replacing $r_a{}^2$ from Equation 14 into Equations 18 and 19, γ_V and γ_M become:

$$\gamma_V = \frac{\varepsilon}{4}\left\{\left(\frac{N_L}{C}\right)^{4/5} - 1\right\} \tag{20}$$

$$\gamma_M = \frac{\varepsilon}{4}\left\{\left(\frac{N_L}{C}\right)^{4/5} - 1\right\}\frac{\rho_p}{\rho_w} \tag{21}$$

where $\varepsilon = 0.7$, (data-fitted from experimental results - ref. 33)

2.3 Downstream Fluid Flow Considerations

Theoretical and experimental investigations by numerous authors have revealed that various types of vortices, depending on the Reynolds number region, will occur downstream of the wire. The Reynolds number of the wire is given by:

$$Re_w = \frac{\rho f \; d \; v}{\eta} \tag{22}$$

where ρf is the density of the fluid, d = diameter of the wire, v = flow velocity, and η = fluid viscosity.

The phenomenon of boundary layer separation which produces the various vortices are intimately connected with the pressure distribution in the boundary layer, and is caused by the back flow of fluid around the wire (22).

Examining the flow about a cylinder (Figure 18) in frictionless flow, the fluid particles are accelerated on the upstream half from D to E, and decelerated on the downstream half from E to F. Hence, the pressure decreases from D to E and increases from E to F. When flow starts, the motion in the first instant is very nearly frictionless, and remains so as long as the boundary layer remains thin. Outside the boundary layer, there is a transformation of pressure into kinetic energy along DE, the reverse taking place along EF, so that a particle arrives at F with the same velocity as it had at D. A fluid particle which moves in the immediate vicinity of the wall in the boundary layer remains under the influence of the same pressure field as that existing outside, because the external pressure is impressed on the boundary layer. Owing to the

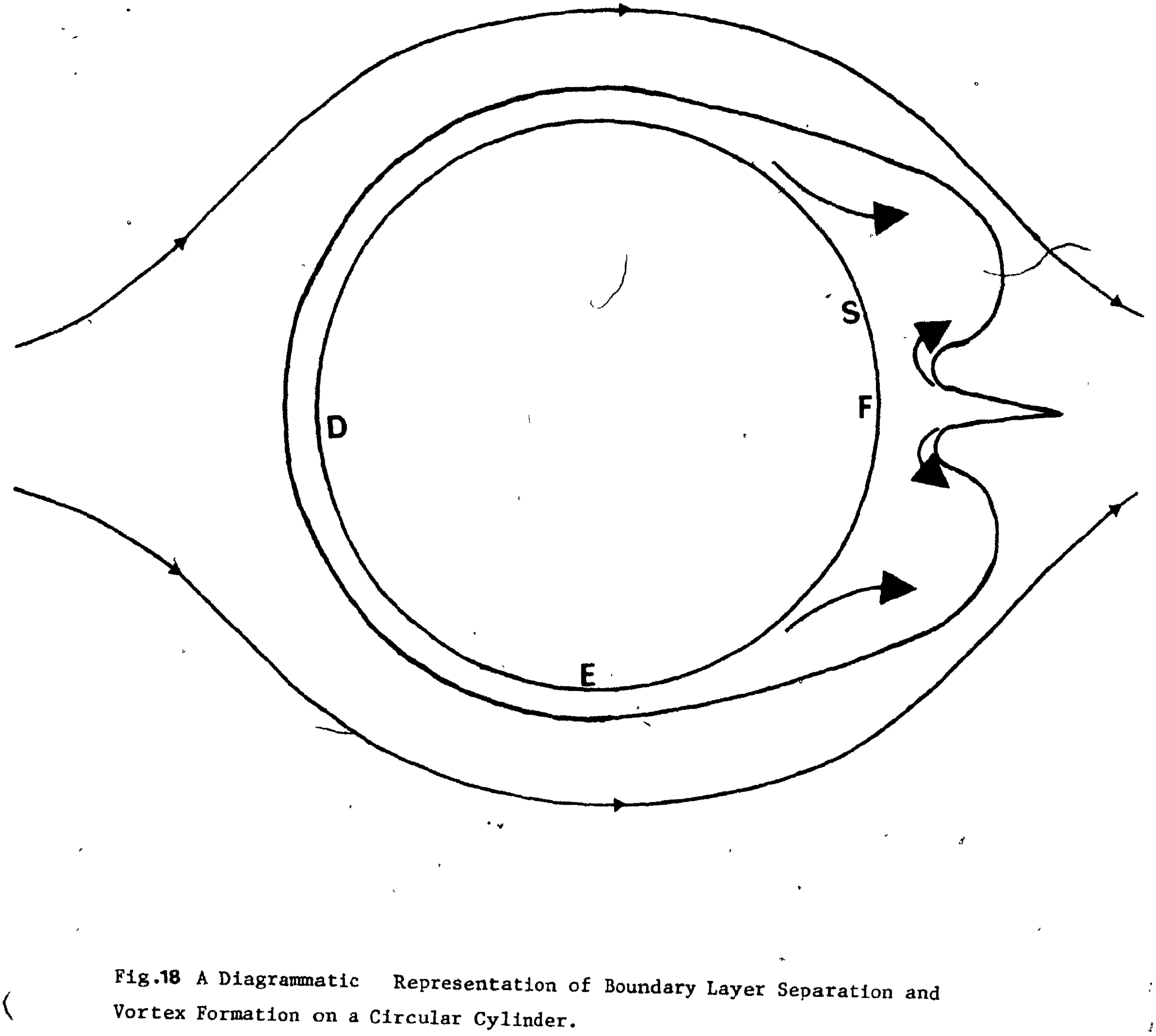

Fig.18 A Diagrammatic Representation of Boundary Layer Separation and Vortex Formation on a Circular Cylinder.

large friction forces in the thin boundary layer such a particle consumes so much of its kinetic energy on the path from D to E that the remainder is too small to surmount the "pressure hill" from E to F. Such a particle cannot move far into the region of increasing pressure between E and F and its motion is, eventually, arrested. The external pressure causes the particle then to move in the opposite direction. Under this reverse motion the particle penetrates a considerable distance forwards and thickening of the boundary layer occurs. The reverse motion then gives way to the formation of a vortex. This vortex continues to grow and separates to move away downstream. When separation occurs (at S) the field of flow in the wake is changed considerably, with the pressure distribution about the wire also changing dramatically. In the final state of motion there is considerable suction in the eddying region behind the cylinder producing a large pressure drag on the cylinder.

At a larger distance from the body, a regular pattern of vortices, which move alternately clockwise and anti-clockwise, may be seen which is known as Karman vortex street (35). The frequency with which vortices are shed in a Karman vortex street behind a cylinder may be calculated using the Strouhal number (36,37) which depends uniquely on the Reynolds number (Figure 19):

$$\frac{nD}{V} = S$$

where S = the dimensionless Strouhal number, D = diameter of the wire, V = velocity and n is the frequency of shedding.

The consideration of fluid flow behind the wire may be convienently divided into a number of sections, dependent on Re_w, which allows description of the drag coefficient and vortex formation.

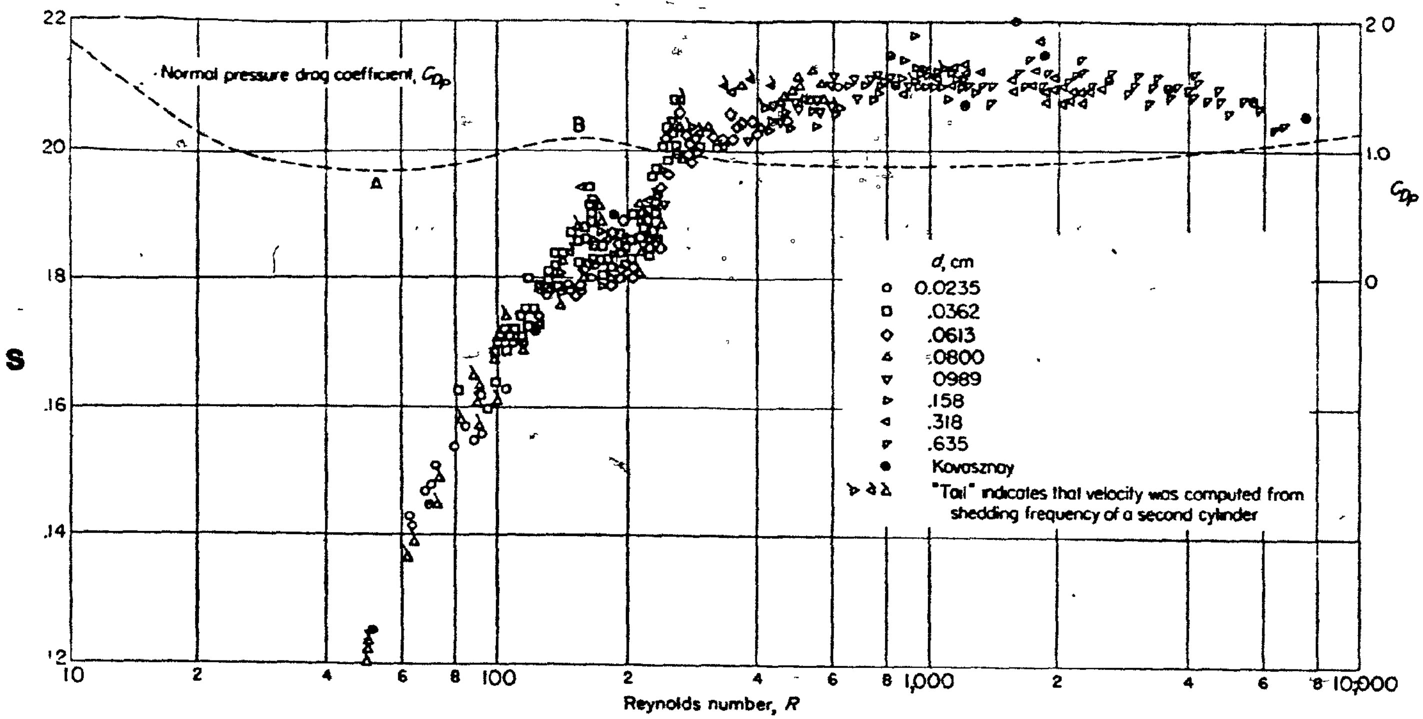

Fig.19 A Graph of Strouhal Number as a Function of the Reynolds Number.

For a $Re_w < 5$(38) or 6.23(39) there is no boundary separation behind the wire. The Drag Coefficient, C_D, for this region is given by:(38)

$$C_D = C_D' (1 + 0.147\ Re_w^{0.82}) \qquad (0.1 < Re_w < 5) \tag{23}$$

where: $$C_D' = 9.689\ Re_w^{-0.78} \tag{24}$$

Above a $Re_w \simeq 5$, a vortex formation with a stationary double vortex occurs in a stable position at the back of the wire. Oscillations of this wake become apparent at $Re_w \simeq 30$, with the wake shedding occuring above $Re_w \simeq 40$. To this point, C_D, may be represented by:

$$C_D = C_D' (1 + 0.227\ Re_w^{0.55}) \qquad (5 < Re_w < 40) \tag{25}$$

Karman vortex streets are visible above a $Re_w \simeq 70$ where the vortex is now termed an instationary double-vortex.

Above a value of $Re_w \simeq 160$, the instationary double-vortex breaks down and instationary single vortices form accompanied by turbulent velocity fluctuations.(37)

For the region from $40 < Re_w < 400$, the drag coefficient is given by:

$$C_D = C_D'(1 + 0.0838\ Re_w^{0.82}) \tag{26}$$

Empirical equations for the angle of separation and length of the vortex have been reported by Brauer:(39)

$$\theta_A = 40.4\ (\ln Re_w - 1.83)^{0.456} \tag{27}$$

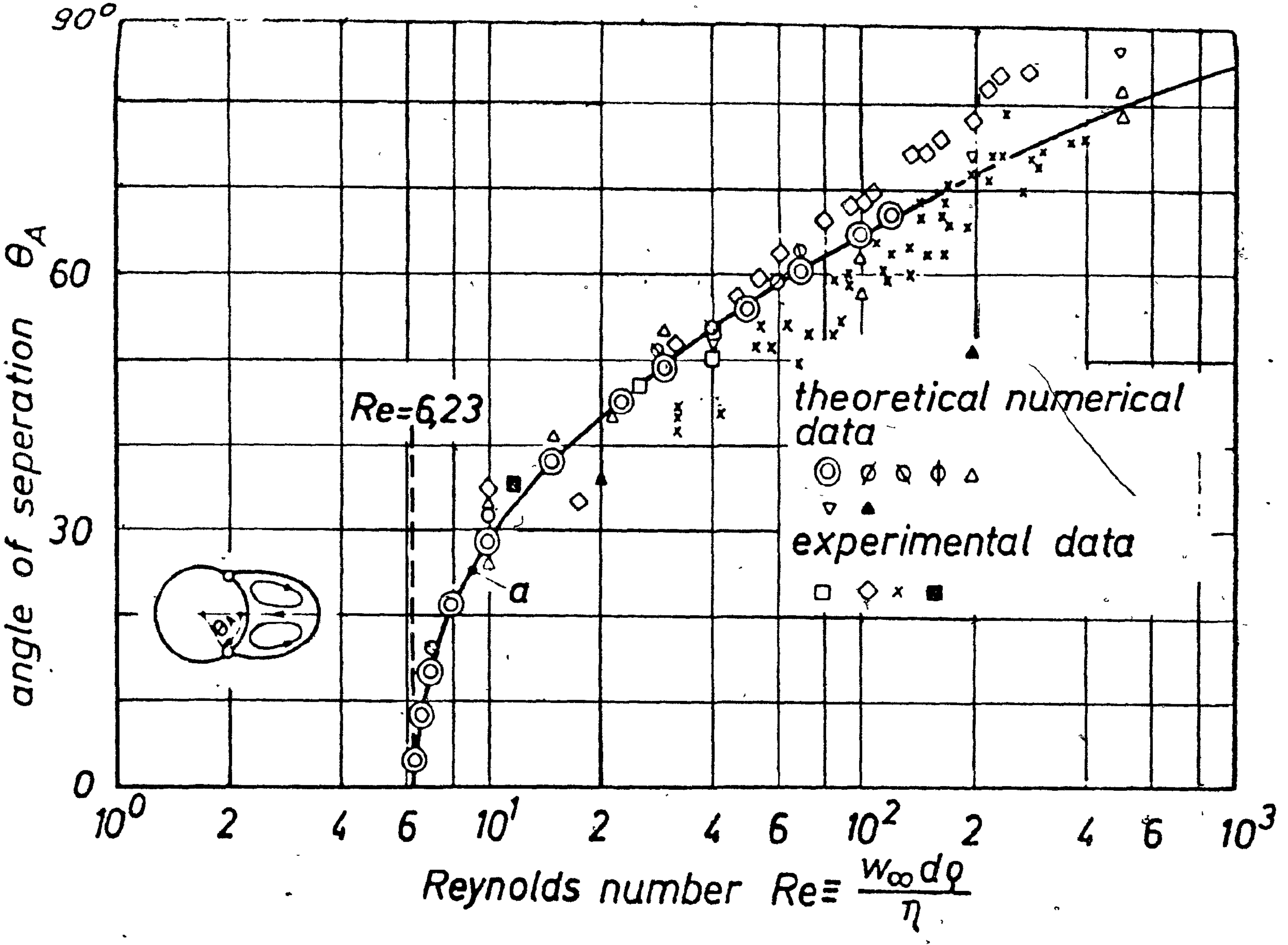

Fig.20 The Angle of Boundary Layer Separation Versus Reynolds Number for a Circular Cylinder.

where θ_A is the angle of separation from the y-axis (Figure 20). This has a range of application of $6.23 < Re_w < 1000$.

The length $L^* = \frac{L}{R}$ where L = length of wake and R = radius of wire is given by:

$L^* = 0.12\ Re_w - 0.748$ with a range of application of $6.23 < Re < 140$. (28)

This is far from a complete revue of the work done on fluid flow about a cylindrical wire but it is detailed enough to provide insight into the effect of the fluid flow on particle build-up on the downstream side of the wire.

III. DESIGN OF APPARATUS

3.1 Single Wire Study

The Frantz Isodynamic Separator is best known for its precise separation of minerals of different magnetic susceptibility. It, can, however, be used in other configurations utilizing its ability to provide a powerful magnetic field. It is used in this case, as a source of uniform field for a single wire study of a longitudinal type hgms (Figure 14, case b).

3.1.1 The Pole Pieces

In order to obtain the longitudinal configuration new pole pieces were required (Figure 21). They needed to be extended out horizontally from the existing plane of the Frantz, to enable a hole to be drilled through to incorporate the fluid system. Another requirement of the pole pieces was that a gap, wide enough to facilitate photography, was needed between them.

The effects of the wider gap and of the extension were unknown and raised a number of questions:

i) Would the field generated between the pole pieces be uniform?

ii) Would the hole through the pole pieces disturb the uniformity of the field?

iii) Would the distance required between the pole pieces for camera work allow a sufficiently large field for magnetic capture on the wire?

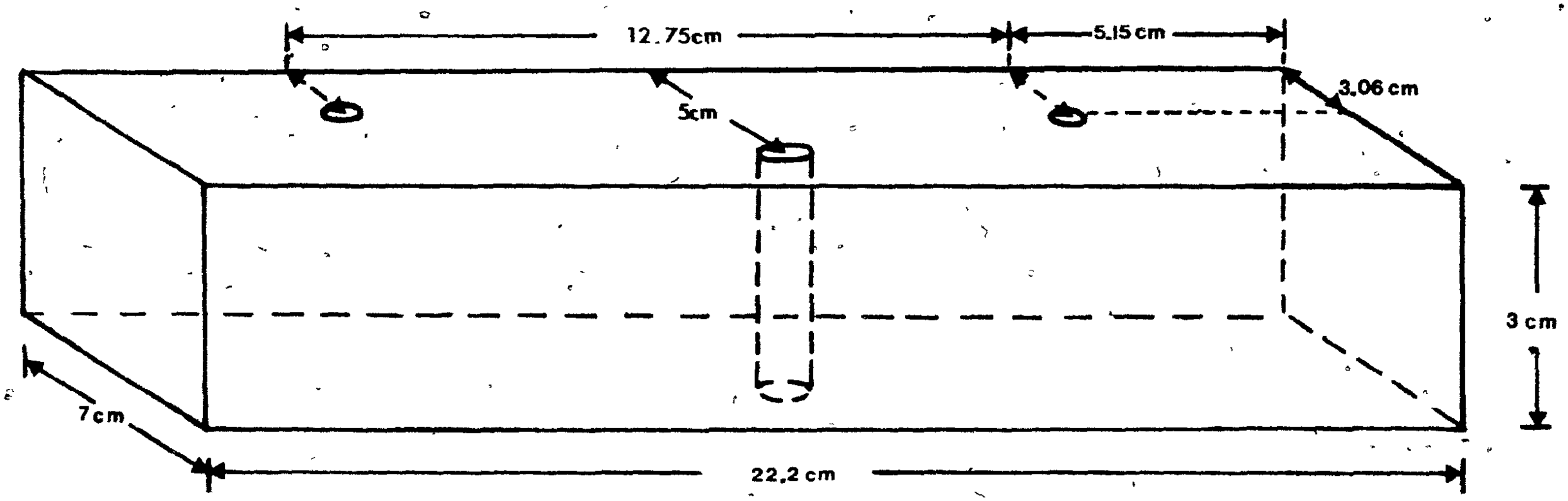

Fig21 The Design of the Single Wire Pole Pieces.

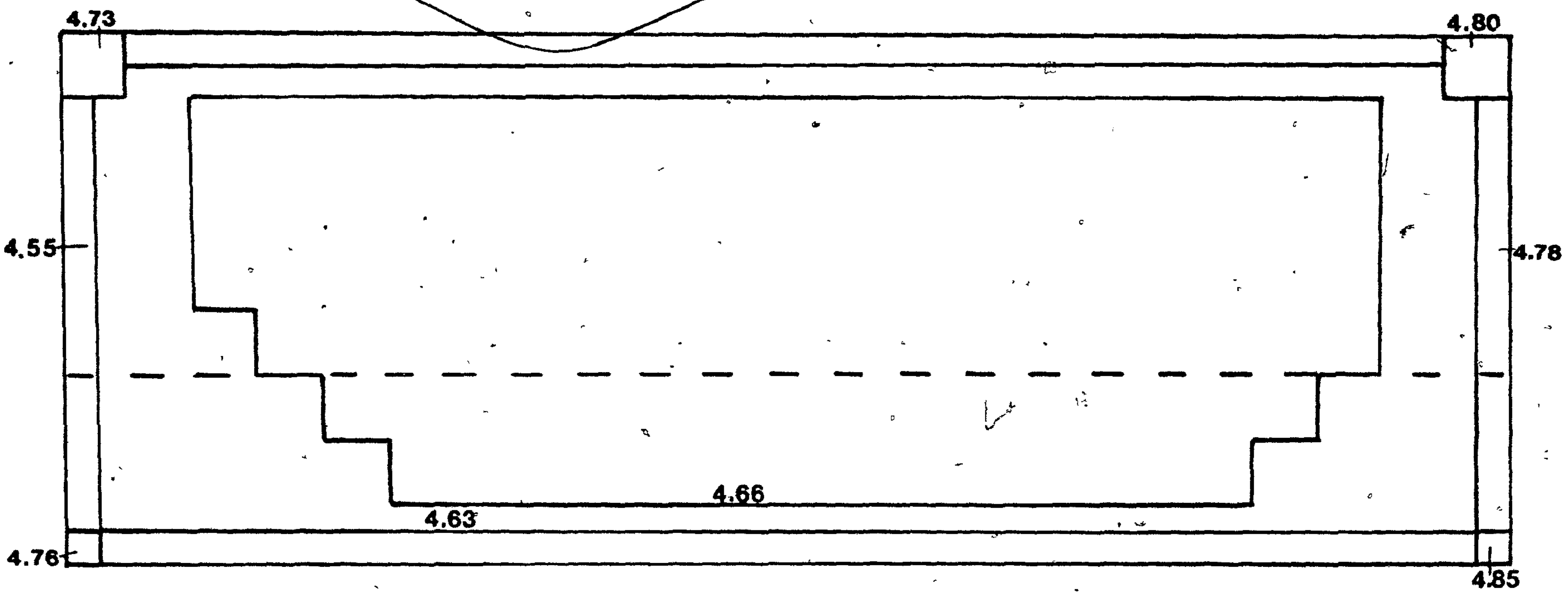

Fig.22 The Magnetic Field Profile Between the Pole Pieces (KOe) at a Current Setting of 1000 mA.

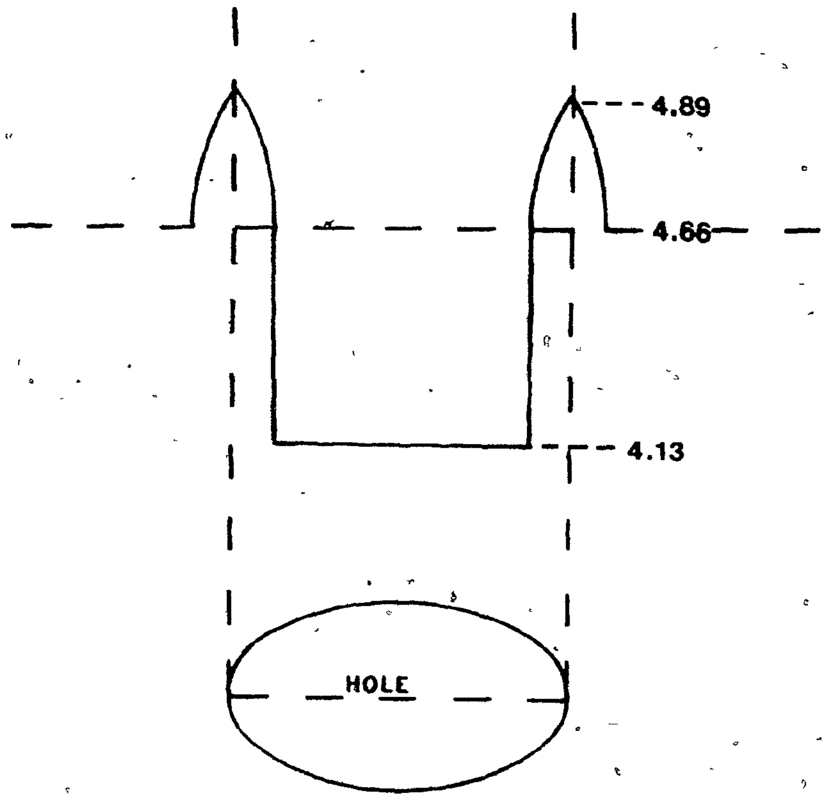

Fig.23 The Magnetic Field Profile in the Vicinity of the Wire. (KOe)

A Hall Probe was used to examine the field distribution between the pole pieces. This was carried out before and after drilling the hole (Appendix 1).

For the purpose of evaluating the field, the inside area of the pole pieces was divided into 1 cm squares; a reading with the probe was taken at the centre of each square. With the values obtained, isodynamic contours were drawn (Figure 22).

From Figure 22, it can be seen that the magnetic field was quite uniform to 0.5 cm of the edge of the pole pieces and that fields of over 4 KOe could be generated (with an input current to the Frantz of 1000mA).

A hole of 0.5 cm diameter and later 1 cm diameter, was drilled through the pole pieces. The field was again probed (Figure 23). It may be seen that the 1 cm hole has no effect on the uniformity of the field outside its own perimeter. The field increases slightly (5%) across the perimeter and decreases by about 11% across the centre of the hole. It was decided that the maximum hole diameter would be 1 cm to avoid further disturbance of the field. The system was then constructed.

3.1.2 <u>The Wire</u>

A galvanized mild steel wire of about .09 cm diameter was used for the experiments. After being cut to the required length, the ends were flattened on a grinding wheel. The wire end was located about $\frac{3}{4}$ of the distance across the fluid flow. This position was selected to ensure the end of the wire would not be in the slow moving boundary layer, and that the measured average velocity of the fluid would approximately equal the velocity at the tip of the wire.

The main problem was one of fixing the wire into position within the confines of the gap between the pole pieces.

Initially, plastic "Tygon" tubing was used so the wire could be inserted by simply puncturing the tube with the end of the wire. Unfortunately, the wire proved unstable in the tubing at both high flow rates and high fields. In addition, on taking photographs of the wire through the plastic, faults in the easily flexed tubing, obscurred much of the detail of the build-up profile. Consequently it was decided that a glass tube should be used for the fluid system.

By heating the glass tube, (15.0 cm length x 0.9 cm diameter) at a small, central position until slightly viscous, a hole could be produced by pulling this spot with the tip of a hot glass rod. The wire could then be inserted. To secure the wire initially, another small length of tubing was attached around this hole to support the wire and to facilitate glueing. But, when the photographs were taken of the wire, a "halo" image in the background where the tube had been attached obscurred the build-up detail once again. This method was therefore abandoned.

The problem of light being reflected unevenly on the heated glass, was overcome by spraying a layer of white paint onto a small area surrounding the hole to provide a suitable background for showing details of the build-up profile. A layer of insulation tape was then placed on top of the dried coat of paint. This was to prevent the paint peeling off when the glue used for securing the wire was applied. The glue was a thick layer of epoxy which also served to keep the hole watertight (Figure 24).

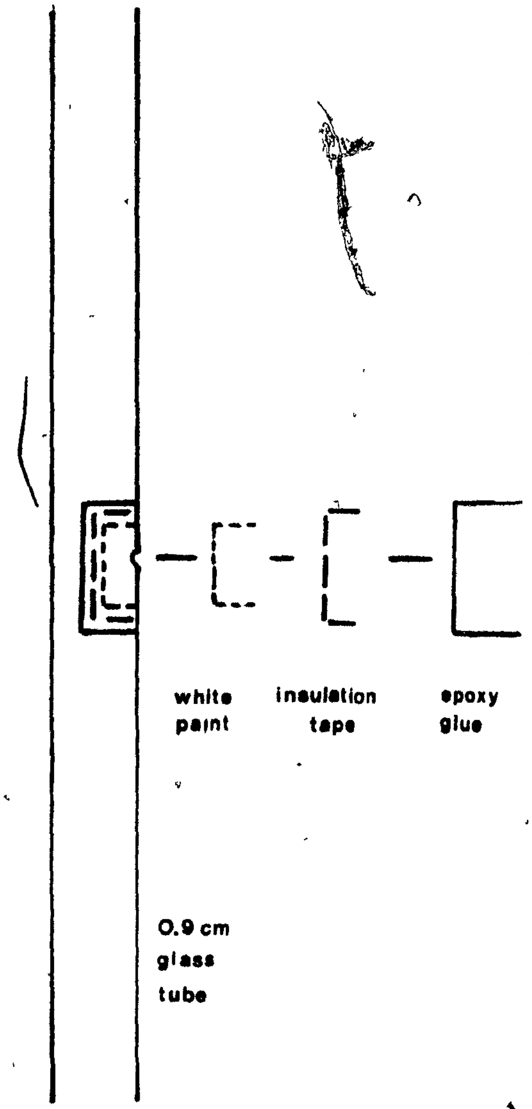

Fig.24 The Process Of Making The Single Wire.

The wire was introduced into the gap between the pole pieces before they were positioned in the Frantz. This was achieved by using supports between them which prevented the wire from being crushed whilst the pole pieces were inserted into position.

A "4 wire" single wire study was also carried out in order to see the effect of other wires on single wire build-up. This configuration was produced in exactly the same manner as the "1 wire" single wire. The resulting configuration of wires is shown in photograph P25.

3.1.3. The Fluid System

The fluid system was designed as a closed loop. This was achieved by using a peristaltic pump to return uncaptured particles back into the reservoir. The reservoir was a cylindrical separatory funnel positioned above the pole pieces. Valve 'A' was inserted into the system in order to incorporate a flushing cycle. This was used to collect the magnetically captured particles after completion of the run.

The completed single wire system may be seen diagrammatically in Figure 25 or in photograph P1.

3.2 High Gradient Magnetic Separation Study

3.2.1 Matrix

In many hgms the layers of matrix frequently rest on top of the one below. This is recommended for capturing fine particles(34). It was decided to construct matrices of different matrix spacing, in particular to determine if additional capture occurred which could be

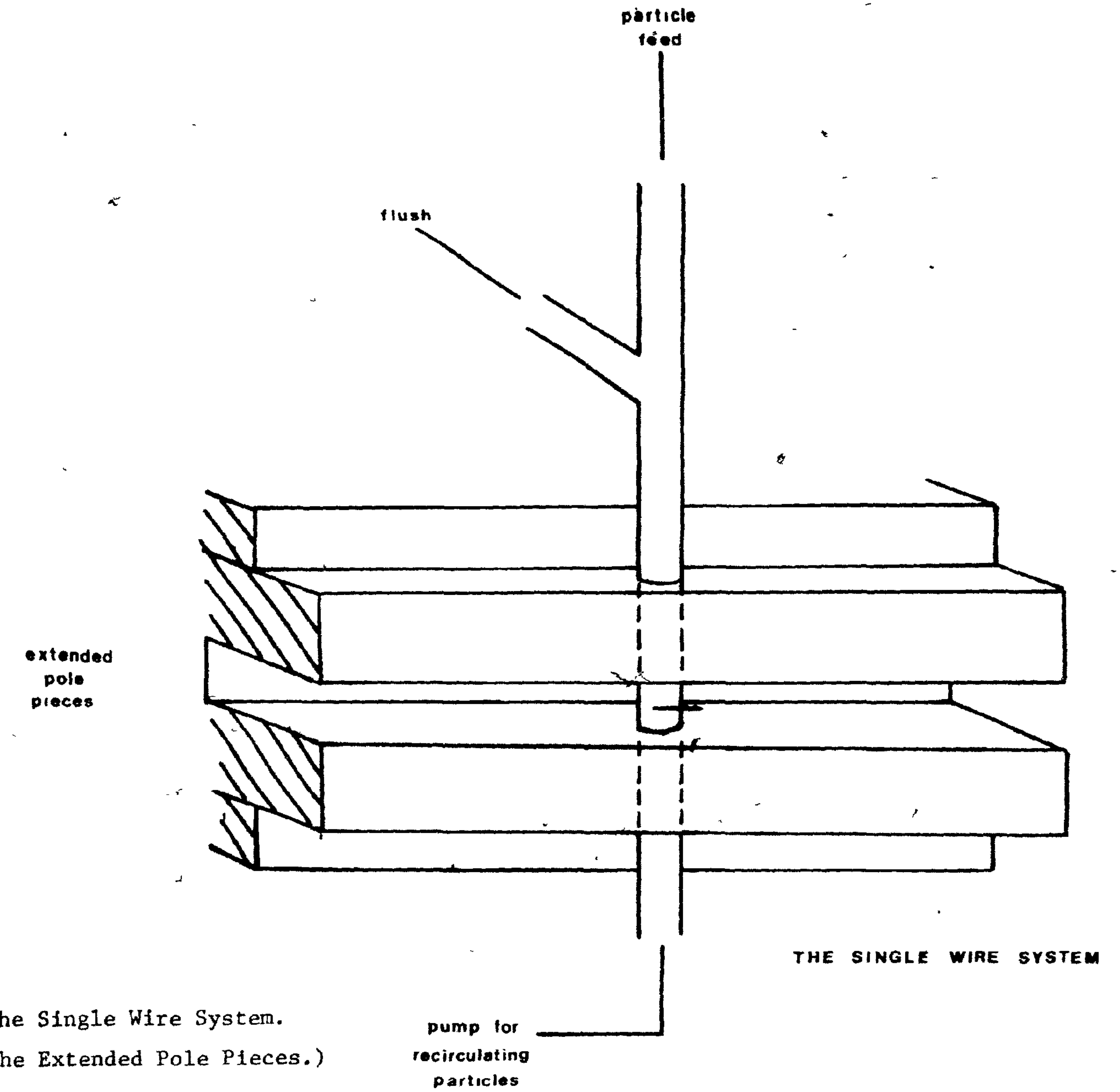

Fig.25 The Single Wire System.
(Showing the Extended Pole Pieces.)

attributed to downstream capture. Three matrices were made. One, termed the closed matrix, had no space between the layers of matrix. Open (1) had a gap of 0.4 cm between adjacent layers and open (2) which had a gap of about 1.1 cm between each layer (Figure 26). Two differently spaced open matrices were made in order to see if the distance apart of the matrices affected the capture capacity.

Each matrix consisted of four expanded stainless steel layers, with two layers at either end of expanded aluminum. This was to try to ensure that the first and fourth stainless steel layers interacted with the particles in a similar manner as the second and third layer.

To produce these matrices, a 13 cm length of cast acrylic tubing (I.D. 3.86 cm, O.D. 5.14 cm) was used as a cannister. The expanded stainless steel and aluminum were cut from sheets into circular pieces of 3.8 cm diameter in order to give a tight fit on insertion into the cannister. Expoxy glue was then used to secure these pieces into the cannister. Each piece was fixed into the cannister at 90° rotation to the adjacent one, as recommended (34).

To form the gap between the layers of matrix, plasticine was used as a support until the glue was hardened. The plasticine was then pulled out of the matrix with the aid of tweezers.

3.2.2. The Fluid System

The fluid system was made from unit conformity copper pipe which expanded to hold the cannister. A distance was left between the expansion and the matrix to minimize the effect of the expansion on the fluid flow profile (Figure 27).

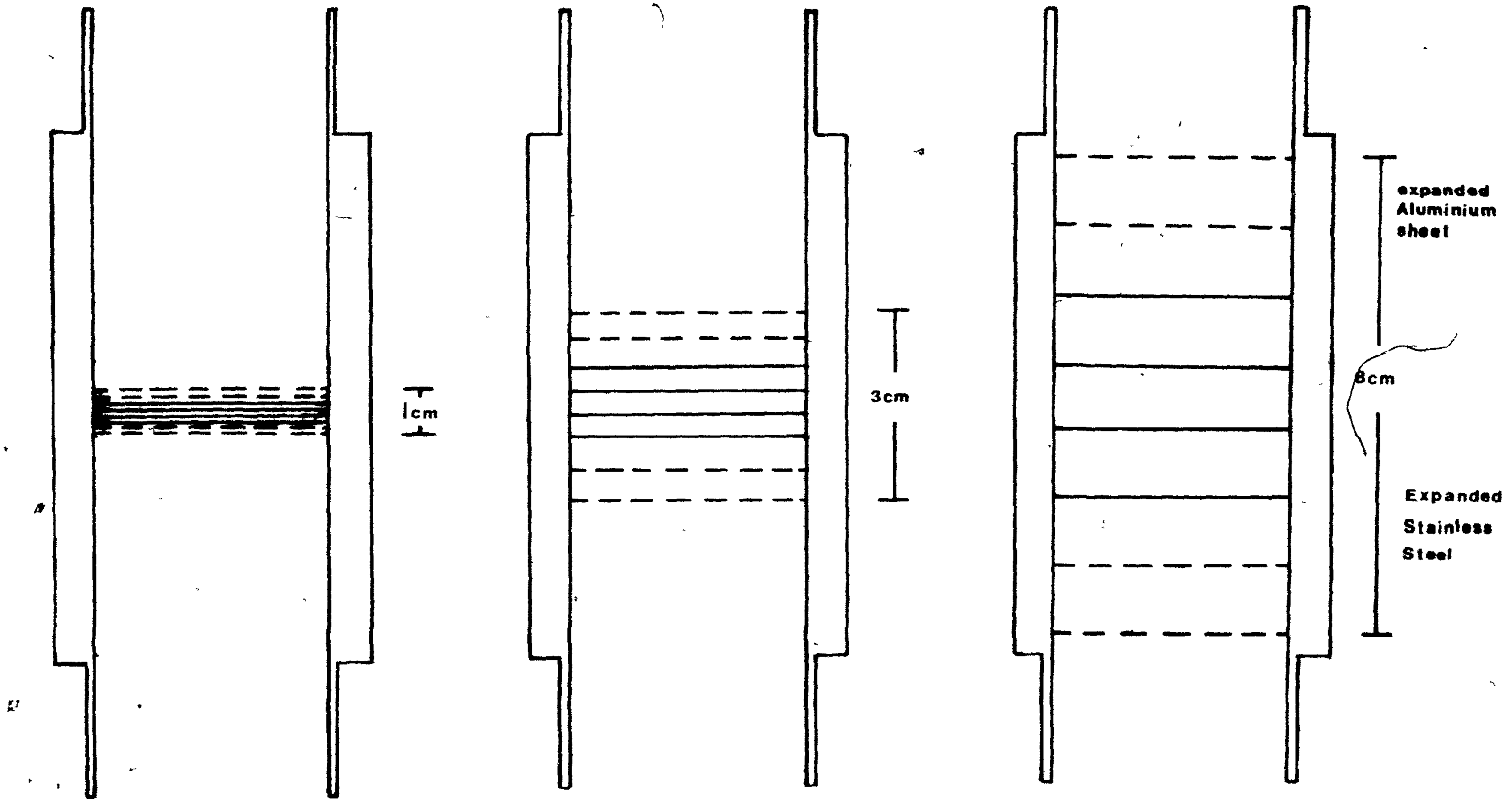

Fig.26 The Three H.G.M.S. Matrices.

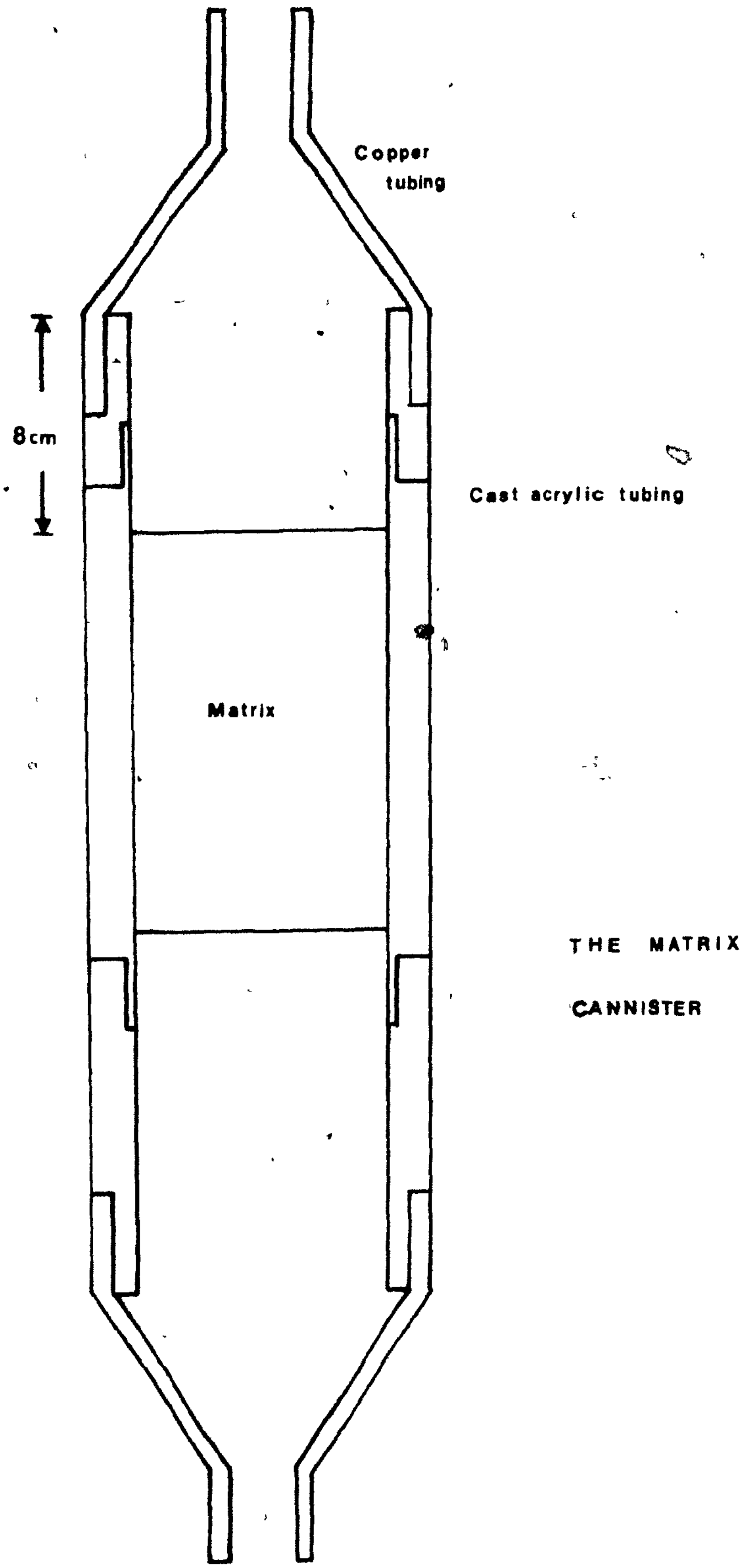

Fig.27 The H.G.M.S. Expanded Matrix Cannister.

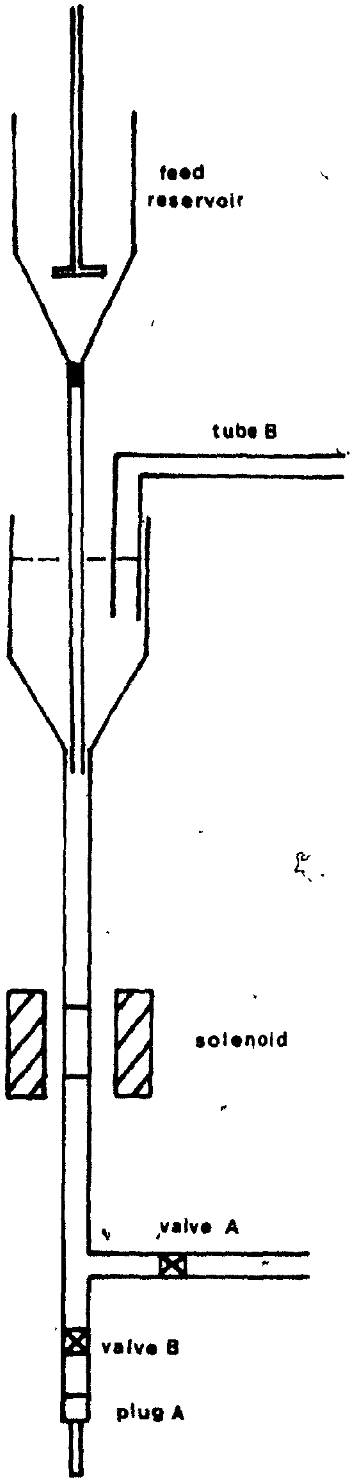

Fig.28 The H.G.M.S. Fluid System.

The system (Figure 28) was arranged so that back-filling was possible which prevented air being trapped, particularly in the matrix. Back filling was achieved by opening value 'A' in Figure 28 and was continued until the reservoir reached a predetermined height. During the experimental runs, this height was maintained by having a steady flow of water from tube 'B'.

The feed reservoir allowed the feed to enter into the system. once a steady flow had been achieved. The flow rate was determined by calibrated plugs 'A' inserted on the exit line (Table 1).

3.2.3. Magnetic Field Selection

The solenoid used in the experiments carried out at McGill could develop fields of 890 Oe or 1690 Oe depending on the D.C. current applied.

Seven field settings were available on the Sala Magnetics 10-15-20 laboratory hgms installed at the Ore Processing Laboratories, CANMET (See Table 1).

TABLE 1

Magnetic Field and Fluid Flow Rates

"Homemade" Apparatus

FIELDS (KOe) : .890; 1.690

FLOW (cm/s) : 0.81; 1.145; 2.17

Sala Magnetics 10-15-20 Laboratory Model

FIELDS (KOe) : 0.66; 1.76; 2.58; 4.2; 6.8; 9.1; 13.8; 21.4

FLOW (cm/s) : 0.89; 1.31; 2.37; 4.18; 7.69

(The underlined values are the only ones used in hgms experiment 1a)

IV. PARTICLE PREPARATION

In order to provide materials with a range of magnetic susceptibilities for the experiments, two different materials were prepared, viz. manganese dioxide and hematite.

The "Anachemia" copper oxide was taken as received and sized into five size fraction of approximately $\frac{1}{\sqrt{2}}$ using the Warman Cyclosizer (Appendix 2).

The manganese dioxide and hematite were sized similarly but after some preparation. 500 grams of manganese dioxide was initially wet ground in a small ball mill using steel balls for an hour. This was done to obtain a suitable size range for the experiments. The hematite was received as -400 mesh material with a small percentage of magnetite present. This was removed using the Davis tube (Appendix 3). The cleaned hematite was then sized. Material sized to 5 μm was obtained by using cone #5 Fe_2O_3 which had had the magnetite content previously removed. This was ground for four hours in a wet ball mill, and sized by settling and decantation (Appendix 4).

V. DESIGN OF EXPERIMENTS

5.1 Single Wire Studies

Experiment 1

This experiment was an attempt to remove the magnetically caught material on the wire in order to measure the mass. Cone #2 and #4 manganese dioxide and cone #4 hematite particles were used as test materials. Magnetic fields varying from 0.6 KOe to 4.6 KOe were used at flow rates of 0.62 cm/s and 7.1 cm/s.

For each test condition, the experiment was carried out for various periods of time in order to obtain a mass caught against time relationship for build-up.

Experiment 2

Cone #2 manganese dioxide was fed into the system with the magnet at two different field settings, 4.1 KOe and 2.4 KOe. Seven different flow velocities were used. Photographs were taken of the particle build-up on the wire after 15, 45 and 120 seconds of each run. It had been established that the equilibrium build-up was achieved after about 120 seconds.

The experiment was conducted in order to see if the shape of the top build-up on the wire predicted by Nesset(34) or other workers was seen. In addition, it enabled the correct photographic techniques to be determined for use in future experiments (Appendix 5).

Experiment 3

In this experiment an alternative material was used to manganese dioxide, to see if the same build-up profile was obtained. Cone #2 hematite was selected. Unfortunately on passing the particles through the system, capture occurred on the glass walls of the fluid system in addition to on the wire. This was due to the large field gradients at the rim of the hole drilled through the pole pieces. Consequently the view of the build-up profile on the wire was obscurred.

It was decided to build new pole pieces with a wider gap (2.5 cm instead of 1.5 cm), so that any build-up on the glass due to the rim of the hole would not obscure the view of the wire.

Therefore, a series of experiments with the new pole pieces and cone #2 hematite were carried out. A field value of 3.5 KOe was used for the runs, with various flow rates from 0.5 cm/s to 20 cm/s.

Photographs were also taken at oblique angles to the wire in order to see the extent of any end effects on the build-up.

Experiment 4

In this experiment, the same pole pieces were used as in the cone #2 Fe_2O_3 runs, but the feed material was -150 + 200 mesh manganese dioxide (geometric mean ~88 μm) in order to see the effect particle size had on the build-up profile.

Experiment 5

5μm hematite was used as the feed material in this experiment. Using this size of material would give a similar $\frac{V_M}{U_\infty}$ ratio as that of the cone #2 manganese dioxide (experiment 2). This experiment was carried out in order to see if the build-up profiles observed resembled those obtained with the 23μm manganese dioxide (Appendix XI).

A field of 3.5 KOe, with the same flow velocities as experiment four were used.

Experiment 6

Using the 4 wire 'single wire' apparatus, an attempt was made to observe the effect the presence of another wire had on the build-up profile.

Runs were carried out using both cone #2 manganese dioxide and cone #2 hematite. A variety of flow rates were used, with fields of 3.5 KOe and 4.1 KOe used for the hematite and manganese dioxide respectively.

5.2 H.G.M.S. Experiments

Experiment 1

Identical experiments were carried out using the three different matrices viz, closed, open (1) and open (2), in order to make a comparison of the mass of captured material in each case. Sufficient material was fed to the system to reach the fully loaded condition. This was determined by Nesset(33) to be about 20 x γ_M (the predicted mass of material to be caught, given by the loading equation).

On the completion of each run, the captured and uncaptured material was dried and weighed.

A variety of magnetic fields and flow rates were used in the tests using both the solenoid from the Davis tube as the source of the magnetic field and also the Sala Magnetics 10-15-20 laboratory unit at CANMET.

Experiment 2

Using a sample of cone #3 Fe_2O_3, a field of 1690 Oe and a flow rate of 2.8 cm/s, a range of feed masses were fed to the closed and open (1) matrices in order to see if the open matrix could capture more material when fed more than 20 x γ_m. Also observed was the capture behaviour before the fully loaded condition has been achieved.

Experiment 3

A sample of 50% Fe_2O_3: 50% Silica (both sized to cone #2 to give similar flow characteristics) was fed to the open (1) and closed matrices. This was carried out using a flow rate of 1.1 cm/s and 1690 Oe and repeated four times for each matrix. The resulting captured and uncaptured material was then assayed to obtain the grade and recovery of hematite for both matrices.

VI. EXPERIMENTAL PROCEDURES

6.1 Single Wire Study

6.1.1 Quantitative Analysis

The magnetic field was set at its required value using the variac on the Frantz. It was then switched off. Pump speed was similarly set by a variac; it too was then switched off (Appendix 6).

The feed was prepared by thorough wetting in a 0.1% Calgon solution. It was then poured into the funnel reservoir and stirred once more.

The magnetic field was switched on. After two minutes of stirring, the valve at the base of the reservoir was opened, the pump was switched on, which was recorded as time zero. The experiment was run for a specific period e.g. 30, 60 or 120 seconds. The pump and valve were then closed simultaneously in order to prevent flow of any more material from the reservoir on to the wire.

The 'Tygon' tubing running from the pump to the reservoir was removed from the reservoir and placed in a beaker. The magnetic field was switched off and the captured material was pumped into the beaker using the wash system.

The material in the beaker was then allowed to settle, the water decanted, and the material was dried and weighed.

This procedure was repeated for different values of time, field and flow rate.

6.1.2 Photographic Analysis

A similar procedure was carried out as in the quantitative experiments except photographs were taken at various times during each run. After the final photograph had been taken the field was switched off, the flow rate was increased and the captured material was carried back into the reservoir in preparation for another run with a different field and flow rate.

A blow-up of the print was analyzed using an electronic digitizer which calculated the area of the build-up shown on the wire (Appendix 7). Consequently, the extent of the front and back capture was easily determined. The area of build-up to area of wire ratio was determined, for testing against model predictions.

6.2 High Gradient Magnetic Separation

Again each sample was stirred in a Calgon solution (·1%) in order to thoroughly wet the particles.

The sample reservoir was filled with 500 ml of water and the matrix system was back-filled to a pre-determined level using valve 'A'. The valve 'B' at the base of the system was then opened and the water began to flow at the rate governed by the size of the plug. With the magnet on, the feed tube 'B' into the top of the matrix system was opened and the water level held constant at the original level. The magnet was switched on, and the material entered the system.

Valve 'B' was eventually closed at the end of the run, when no particles could be seen flowing through the clear acrylic tubing of the cannister. The magnet was then switched off. The plug controlling the flow was removed, valve 'B' opened and the system was emptied into a bucket. It was then back-filled and flushed twice to ensure all material was removed.

The particles were allowed to settle, the water was decanted off, and the material was dried and weighed.

Experiments were carried out with a zero magnetic field, in order to obtain a background reading of the physical capture on the matrix. This was done for each run.

Runs were also carried out using an empty cannister i.e. with no matrix, in case material was being caught magnetically on the sides of the tubing rather than on the matrix itself.

VII. RESULTS

7.1 The Single Wire

Experiment 1 - Quantitative Analysis

The weight of particles captured on the single wire under the various test conditions are seen in Table 2 and Appendix 8. The results show little correlation with the test conditions and on repeating a run vastly different results were obtained. This was due to the difficulty involved in flushing out the captured particles. The small mass of particles caught was often negligible in comparison to the amount of particles remaining in the fluid system on flushing. Consequently, the results obtained were unrelated to the amount of capture on the wire.

Experiment 2 - Cone #2 (23 μm) Manganese Dioxide

Photographs P2 - P12 illustrate that good definition of the build-up profile was achieved using the described photographic techniques (Appendix 5). The build-up profiles shown in the photographs (p.50) illustrate the range of build-up shapes obtained. Back capture appeared the dominant mode of particle capture, with very little front build-up observed under any of the test conditions.

The shape of the build-up appeared dependent on both the magnetic field strength and the fluid velocity (specifically the Reynolds number of the wire).

At low flow velocities (< 2.7 cm/s) the back capture has a rounded profile, which extends out from behind the wire, P2. As the

TABLE 2

Experiment One

Quantitative Single Wire Analysis

MATERIAL & CONE SIZE	FIELD KOe	FLOW cm/s	MASS COLLECTED (GMS)			
			30s	60s	90s	120s
MnO_2 #4	3.5	7.1	.0024	.0088	.0046	.0047
MnO_2 #2	4.6	7.1	.0071	.0057	.0150	.001100

flow rate was increased, the sides of the build-up became straighter, extending back behind the wire, e.g. P3. As the flow rate increases further, the sides of the build-up are straight, with the back build-up length decreasing with increased flow rate (Table 6).

At high field strength and low flow velocities, magnetic capture occurs on the glass wall obscurring the build-up profile (P5).

The area of back build-up obtained under the test conditions is seen in Tables 3 and 4. It may be seen that the area of the bare wire on the two Tables is different. This is due to the experiment being carried out in two stages. Consequently the camera position and the size of the photographic blow-up were changed. However γ_A may be compared between the two Tables, as this is a ratio of areas as given in equation (20):

$$\gamma_A = \frac{\text{Area of particle build-up}}{\text{Area of the bare wire}}$$

Figures 29 and 30 show γ_A plotted against N_L and $\frac{V_M}{U_\infty}$ respectively. It may be seen that both graphs produce a smooth curve. However, the Loading Number, N_L, has a theoretical minimum at $N_L = 2.5^{(2)}$ which is clearly violated. Also, for $N_L > 2.5$, γ_A is practically constant which does not agree with the form of the loading equation.

Table 5 shows the theoretical boundary separation angles (θ_A) and wake length (L*) given by Equations 27 and 28. Although at 0.62 cm/s, P2 does not show a build-up angle of $\approx 22^0$, at higher flow rates, the build-up angle may be seen to extend about an arc (i.e. 2θ) or $\approx 140^0$ which might indicate that the build-up is limited by the angle of separation. L* can be seen to be of too large a value to be the limiting factor in the build-up length. Indeed L* increases with Reynolds number whereas the

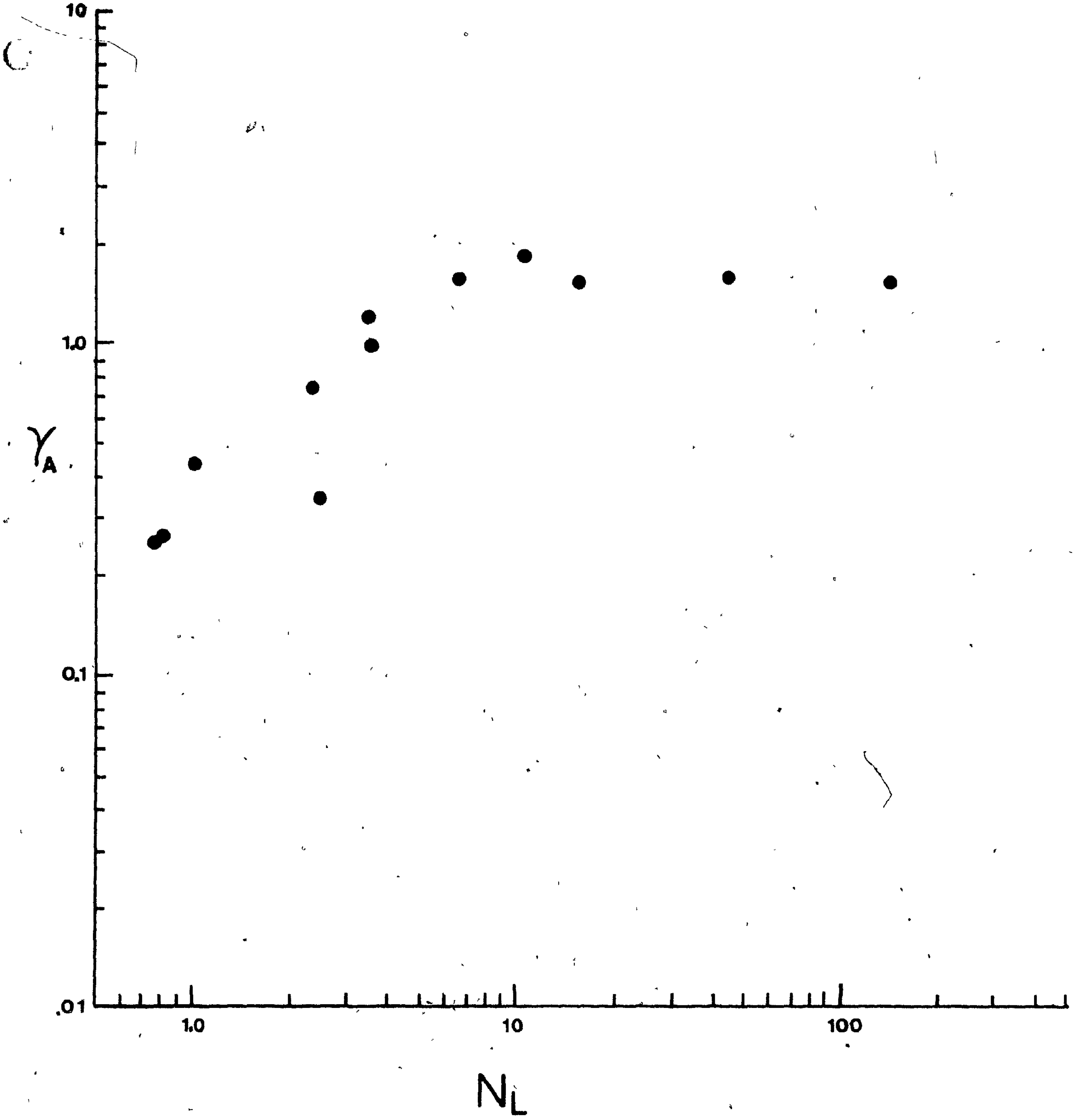

Fig.29 Graph Of Loading versus N_L For 23μm Manganese Dioxide.

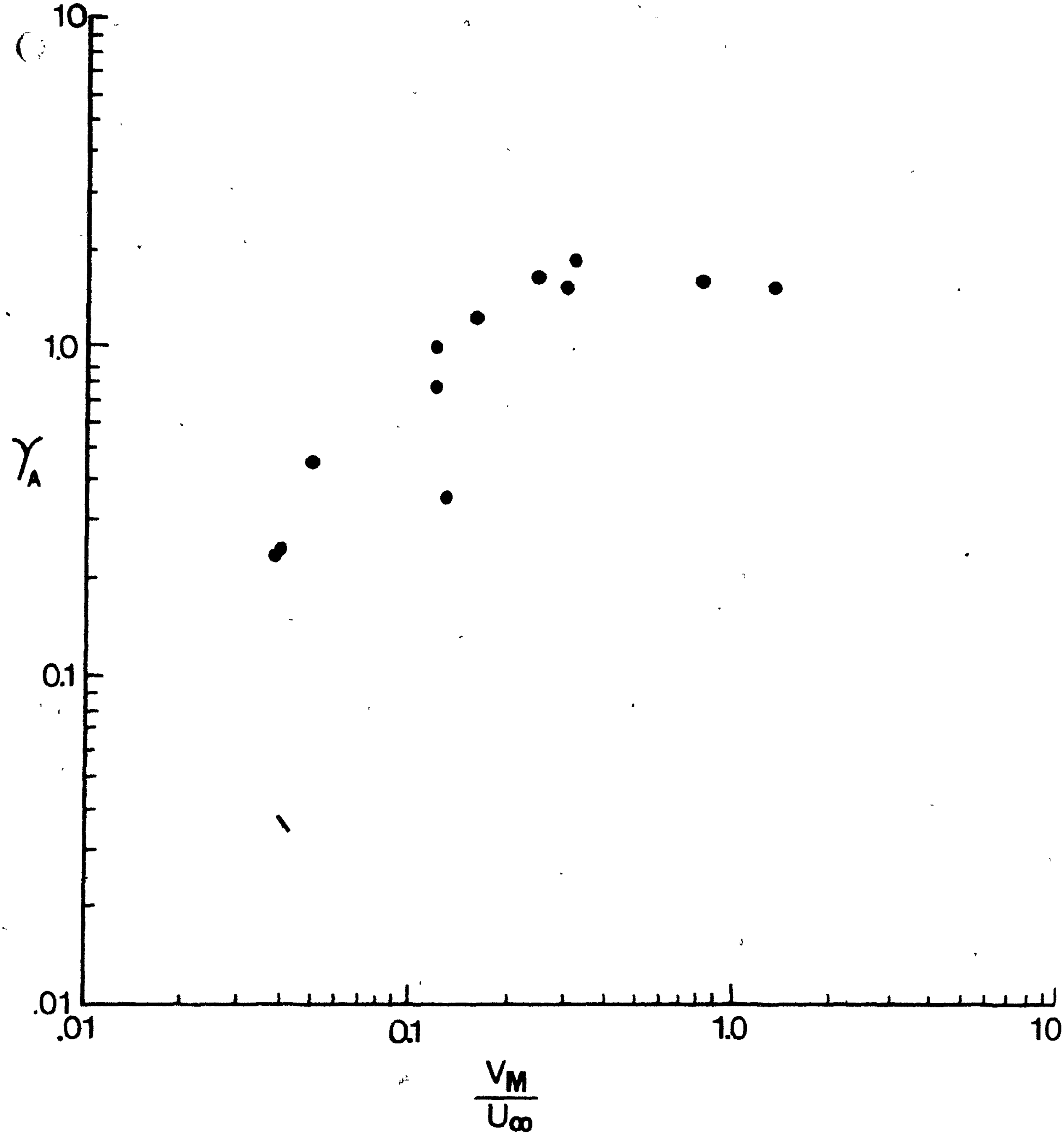

Fig.30 Graph Of Loading versus V_M/U_∞ For 23 μm Manganese Dioxide

TABLE 3

Experiment Two(a)

(23 μm manganese dioxide)

Area of Back Build-up Using the Digitizer

Area of the wire (Aw) = 1.57

Field 2.4 KOe

Flow Rate cm/s	Reynolds Number	V_m/U_∞	N_L	Area of Back Build-up (Ap) 15s	45s	120s	γ_A = Ap/Aw
0.62	5.58	1.33	136.5	0.78	1.63	2.39	1.52
7.1	63.58	0.12	3.52	0.98	1.40	2.39	0.99
18.9	170.1	0.04	0.81	-	-	0.38	0.24

Field 4.1 KOe

Flow Rate cm/s	Reynolds Number	V_m/U_∞	N_L	Area of Back Build-up (Ap) 15s	45s	120s	γ_A
0.62	5.58	3.87	398.2	-	-	-	-
7.1	63.58	0.34	10.28	1.68	2.59	2.9	1.84
18.9	170.1	0.13	2.37	0.4	0.52	0.55	0.35

TABLE 4

Experiment Two(b)

Area of Back Build-up Using the Digitizer

Area of the wire (Aw) = 0.73

2.4 KOe

Flow cm/s	Reynolds Number	V_m/U_∞	N_L	Area of Back Build-up 15s	45s	120s	γ_A
2.7	24.3	0.30	15.01	0.36	0.77	1.10	1.15
14.86	133.7	0.05	1.16	0.23	0.29	0.29	0.45
19.22	173.0	0.04	0.79	0.11	0.13	0.13	0.23

4.1 KOe

Flow cm/s	Reynolds Number	V_m/U_∞	N_L	Area of Back Build-up 15s	45s	120s	γ_A
2.7	24.3	0.89	43.8	0.28	0.71	1.15	1.58
9.54	85.8	0.25	6.6	0.46	1.13	1.17	1.60
14.86	133.7	0.16	3.4	0.18	0.70	0.89	1.22
19.22	173.0	0.12	2.31	0.43	0.52	0.55	0.75

TABLE 5

Experiment Two

Theoretical Build-Up Angles (θ_A) and Lengths L*

(see Equations 27 and 28)

Flow Rate cm/s	Reynolds Number (Re_w)	θ_A (Degrees)	L*	L = L* R (mm)
0.62	5.6	21.78	.008	.0036
2.70	24.3	46.5	2.17	1.21
7.10	65.1	59.6	6.40	2.88
9.54	85.9	62.7	9.55	4.30
14.86	133.7	67.3	15.30	6.88
18.90	172.1	69.8	19.96	8.98
19.22	173.0	69.9	20.00	9.00

TABLE 6

Experiment Two

Frequency of Vortex Shedding

Flow Rate cm/s	Reynolds Number	Strouhal Number (s)	Frequency of Shedding (n)	Experimental Build-up Length(mm)
0.62	5.6	0.0	0.0	-
2.70	24.3	0.0	0.0	-
7.10	65.1	0.140	14.84	7.0
9.54	85.9	0.158	16.75	7.0
14.86	133.7	0.173	28.56	5.0
18.90	172.1	0.184	38.64	2.0
19.22	173.0	0.185	40.54	3.0

build-up length decreases. Table 6 shows the rate of vortex shedding given by the Strouhal number, against build-up length. The increase in rate of shedding does correlate with the decrease in build-up length.

Experiment 3 - Cone #2 (22 μm Hematite)

Large amounts of front capture was seen in these photographs which unfortunately produced shadows, causing some loss of definition of the build-up profile.

At low flow rates (< 4.5 cm/s), large amounts of front capture were seen, for example, photograph P13. As the flow rate was increased however, back capture became the dominant capture mechanism as may be seen from the digitizer results in Table 7. Again, graphs of loading versus N_L and $\frac{V_M}{U_\infty}$ (Figures 31 and 32) were plotted. It is seen that back capture becomes the prominant capture mechanism at $\frac{V_M}{U_\infty} < 0.9$. At about this value also, back capture appears to reach its maximum.

It may be seen that loading versus N_L, fits the loading equation quite well for front and total capture with $\varepsilon = 1.3$ and 2.2 respectively.

The change from front to back capture dominance is illustrated in photographs P13 and P14. P13 shows a large amount of top build-up on the wire, with a shape agreeing with that predicted by Nesset(34). The bottom profile has build-up extending out horizontally from the base of the wire, in a manner unseen in experiment 2. This may be due to the protection from the fluid drag forces given by the copious front build-up.

Photograph P14 shows the top build-up to have decreased and to have lost its straight edged profile definition. The bottom build-up has increased markedly, now with more material than on the front of the wire.

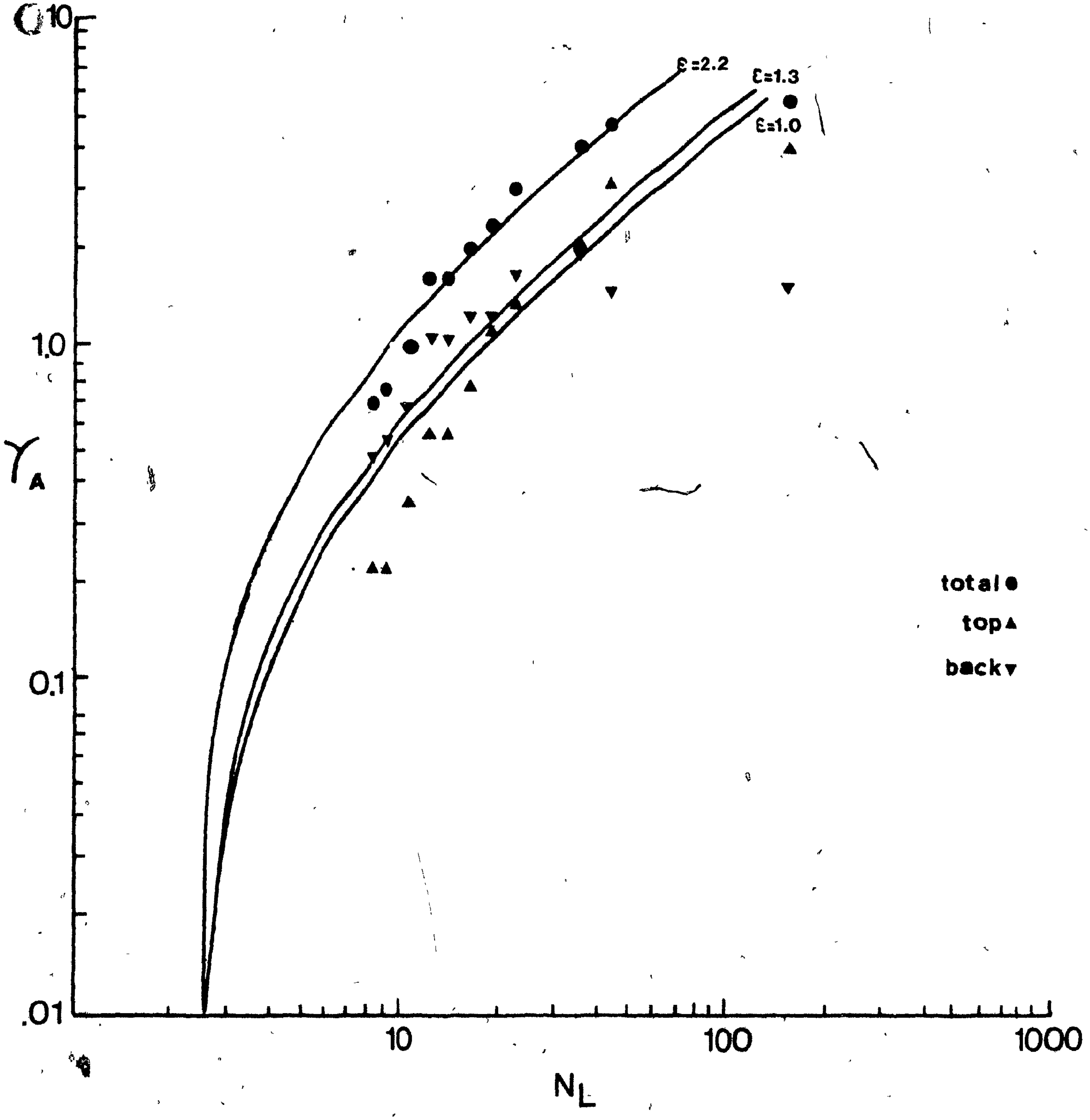

Fig.31 Graph Of Loading versus N_L For 22 μm Hematite.

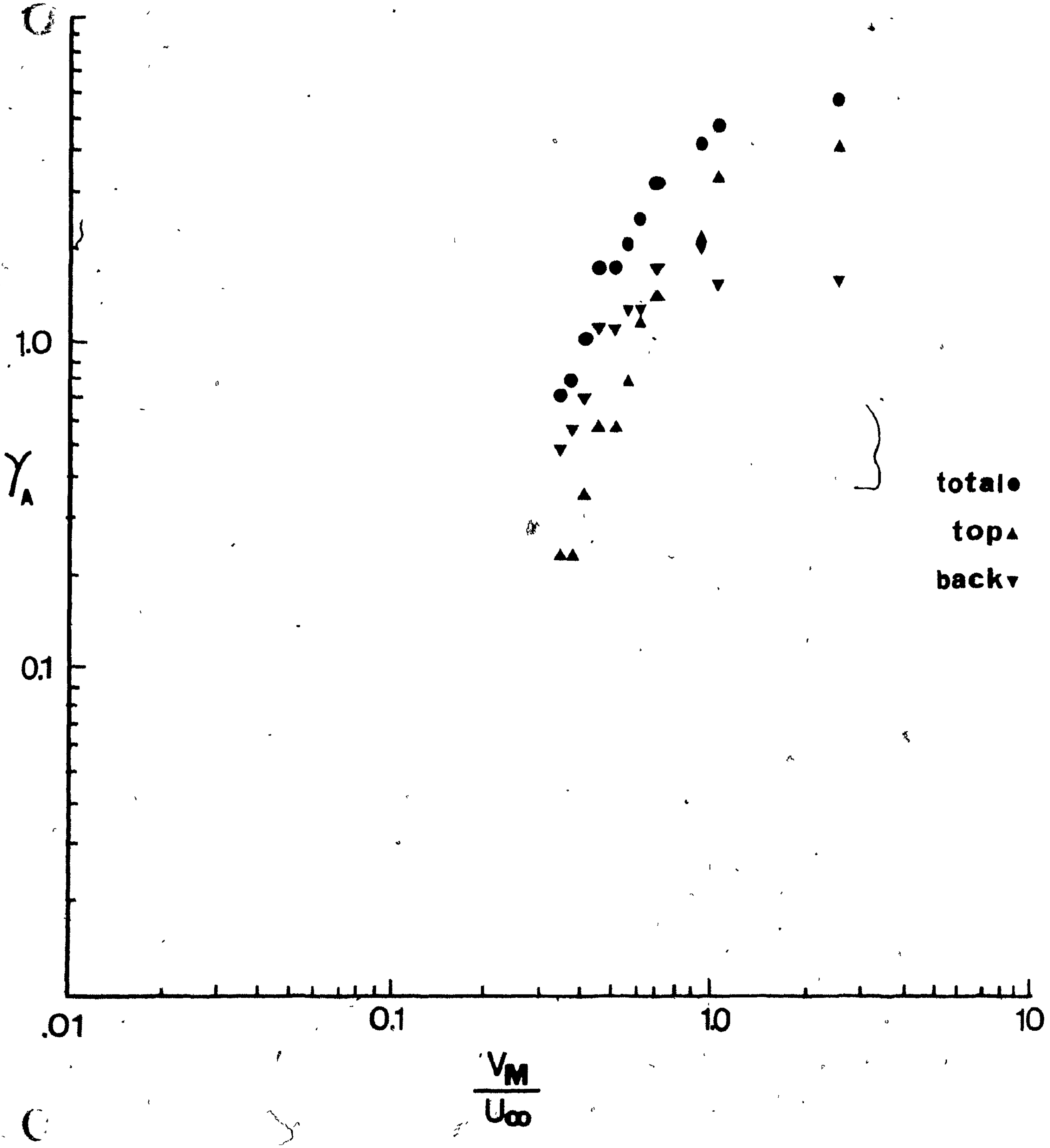

Fig.32 Graph Of Loading versus V_M/U_∞ For 22 μm Hematite.

TABLE 7

Experiment 3 (22μm hematite)

Area of the wire (Aw) = 3.64

3.5 KOe

Flow cm/s	Reynolds Number	V_m/U_∞	N_L	Area of Build-up (Ap) Front (Af)	Back (Ab)	γ_{AF}	γ_{AB}	γ_A	$\frac{Ab}{Ab + Af}$ %
1.79	16.1	2.43	150.9	14.4	5.6	3.96	1.54	5.50	28
4.09	36.8	1.06	43.69	11.43	5.41	3.14	1.49	4.63	32
4.78	43.0	.91	34.58	7.42	7.19	2.04	1.98	4.02	49
6.44	57.9	.67	22.11	4.89	6.08	1.34	1.67	3.01	55
7.22	64.9	.60	18.63	4.21	4.45	1.16	1.22	2.38	51
7.99	71.9	.54	16.0	2.76	4.51	0.76	1.24	2.00	55
8.89	80.0	.49	13.63	2.19	3.96	0.55	1.09	1.64	64
9.78	88.0	.44	11.82	2.01	4.09	0.55	1.12	1.67	67
10.48	94.3	.41	10.65	1.23	2.45	0.34	0.67	1.01	67
11.78	106.0	.37	8.94	0.8	1.98	0.22	0.54	0.76	67
12.78	115.0	.34	7.91	0.8	1.70	0.22	0.47	0.69	71

As the flow rate is increased, the back build-up shows similarities to the shapes obtained in experiment 2 i.e. the round profile and horizontal projection from behind the wire is lost and the edges become straighter projecting back behind the wire (e.g. P16 and P17).

The front build-up is seen to take on a more curved profile extending around the front of the wire, as the flow rate is increased (photographs P15 - P17). It may also be seen from the oblique angle shot, P16, that there is little end effect on the shape of the profiles.

Experiment 4 - 88 μm Manganese Dioxide

These photographs did not produce clear prints but they were sufficient to enable the large difference to be seen between them and those of the cone #2 manganese dioxide (Experiment 2). The larger particles appeared to produce profiles (P18 - P20) more similar to the cone #2 hematite (Experiment 3).

The front build-up profiles indicate a rounded shape similar to those at higher flow rates in experiment 3 (>6 cm/s). The back build-up is shown throughout the range of flow velocities to be limited to the area directly behind the wire, i.e. there is no horizontal build-up extending out from behind the wire.

The digitizer results shown in Table 8, illustrates that front capture was always the dominant capture mechanism. Figure 33, shows $\frac{V_M}{U_\infty} > 1.0$ in each run, which is greater than the 0.9 value when back capture became the dominant capture mechanism with 22 μm hematite.

Figure 34, shows that loading versus N_L produced a reasonable curve for front end total capture once more, but with $\epsilon = 0.5$ and 0.8 respectively.

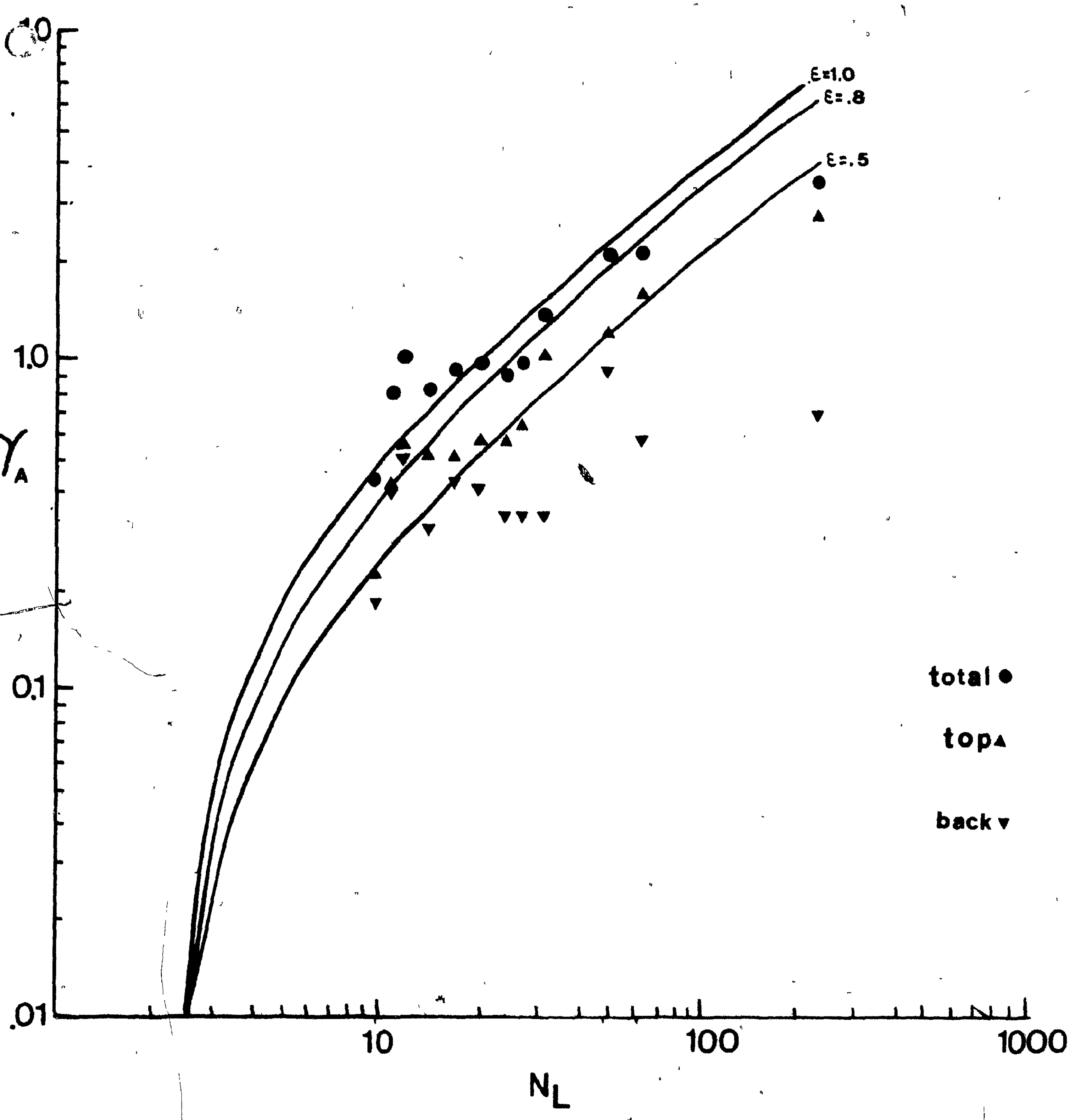

Fig.33 Graph Of Loading versus N_L For 88 μm Manganese Dioxide.

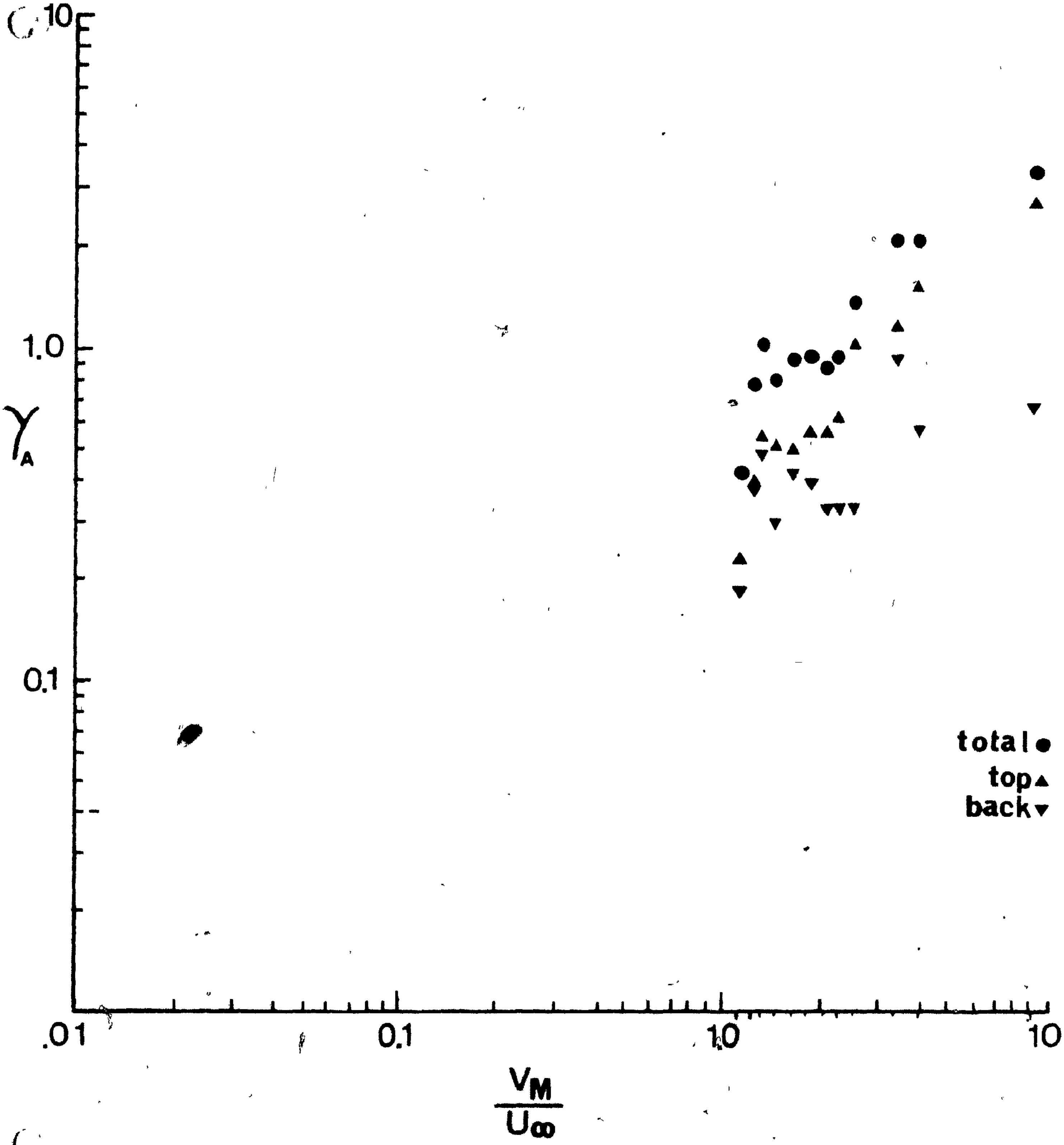

Fig.34 Graph Of Loading versus V_M/U_∞ For 88 μm Manganese Dioxide.

TABLE 8

Experiment 4 (88μm manganese dioxide)

Area of the wire = 2.90

3.5 KOe

Flow cm/s	Reynolds Number	V_m/U_∞	N_L	Area of Build-up (Ap) Front (Af)	Back (Ab)	γ_{AF}	γ_{AB}	γ_A	$\frac{Ab}{Ab + Af}$ %
1.79	16.1	8.87	215.9	8.01	1.92	2.76	0.66	3.42	19
4.09	36.8	3.88	62.5	4.37	1.63	1.51	0.56	2.07	28
4.78	43.0	3.32	49.5	3.39	2.66	1.17	0.92	2.09	44
6.44	57.9	2.46	31.6	2.94	0.97	1.01	0.33	1.34	25
7.22	64.9	2.20	26.7	1.79	0.96	0.62	0.33	0.95	35
7.99	71.9	2.04	23.8	1.59	0.95	0.55	0.33	0.88	37
8.89	80.0	1.79	19.5	1.61	1.14	0.56	0.39	0.95	41
9.78	88.0	1.62	16.9	1.41	1.23	0.49	0.42	0.91	47
11.17	93.3	1.42	13.8	1.48	0.84	0.51	0.29	0.80	36
12.38	111.4	1.28	11.9	1.56	1.41	0.54	0.49	10.3	47
13.17	118.5	1.21	10.8	1.14	1.12	0.39	0.39	0.78	50
14.21	127.9	1.12	9.6	0.71	0.52	0.24	0.18	0.42	37

The back capture did not appear to reach a maximum.

Experiment 5 - 5 μm Hematite

Photographs P21 - P24 illustrate the build-up profiles obtained with the 5 μm hematite. Hematite of this size has a $\frac{V_M}{U_\infty}$ range similar to that of the cone #2 manganese dioxide (Appendix 11). From the photographs it is seen that the capture is mostly at the back of the wire, and vastly different from the cone #2 hematite.

Unfortunately as may be seen in photographs P22 and P24, there were large end effects in these runs and consequently digitizer data would not give a realistic value for γ_A.

It is seen that the build-up in P23 extends further out from behind the wire than P21, even though it is at a higher flow rate. This may be due to the fact that P21 was taken after 60 seconds, not 120 seconds, so full loading may not have been achieved. P22 shows a side view taken after 120 seconds and shows a large amount of back build-up.

Front capture appears in each photograph, apparently to the same extent irrespective of the flow rate. The build-up also seems to project directly upstream with very straight sides in a manner not previously seen.

Experiment 6

Photograph P25 shows the "4 wire" single wire cannister within the confines of the gap between the pole pieces. Photograph P26 shows the build-up of manganese dioxide particles on the four wires very clearly. There would appear from the photograph to be more front build-up than would be predicted from the results of experiments two and three. This is explained by the fact that the build-up extends around to an angle ~45° on the wire and consequently from the side view more material appears to be present than there actually is.

On the photograph it is seen that there is considerable back build-up on the first wire but on the others, the top capture appears to be the dominant mode of capture.

Photographs P27 and P28 are taken with cone #2 hematite as the feed particles. It is again illustrated that the back capture is only present where there is no wire in close proximity.

It seems that when front and back capture are in competition with each other, or where another wire is in close proximity to back build-up, the back build-up will diminish in that region.

SECTION 7.1.1

PHOTOGRAPHS OF PARTICLE BUILD-UP ON THE SINGLE WIRE

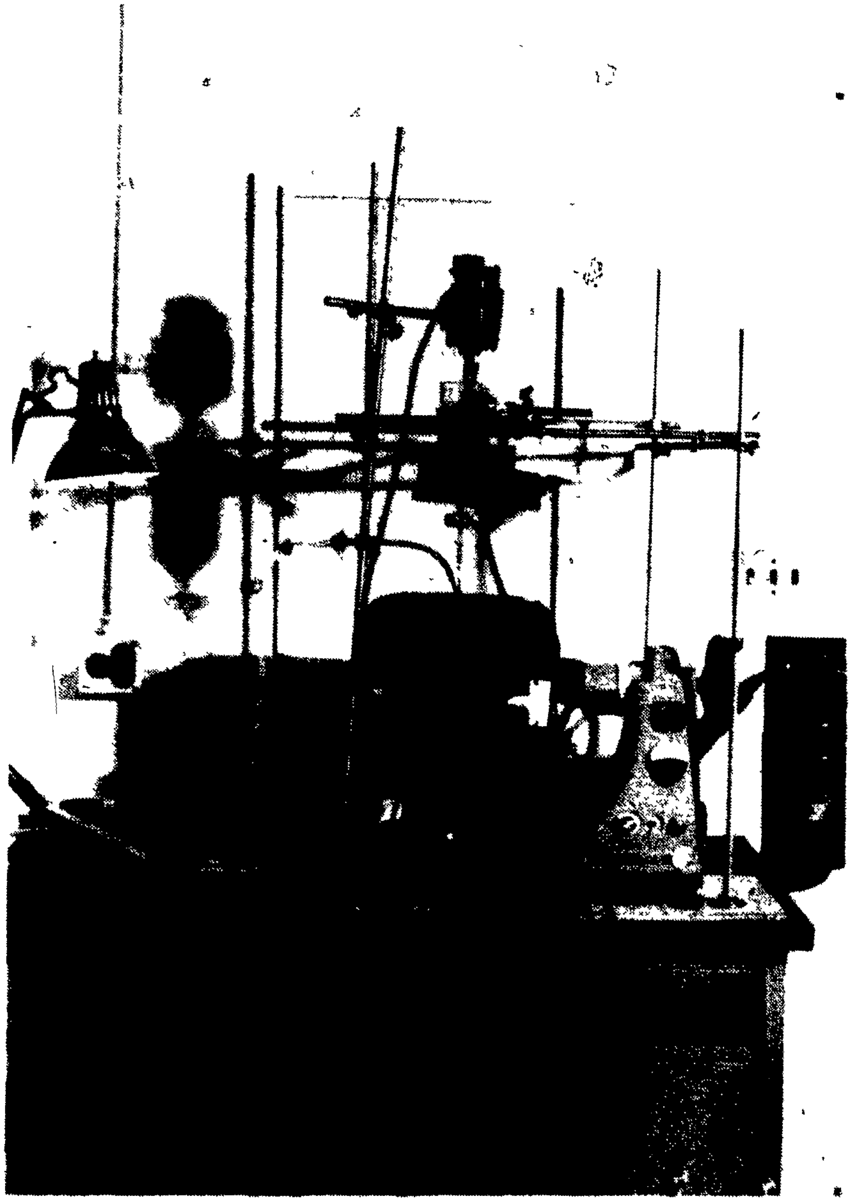

P1. THE APPARATUS USED IN THE SINGLE WIRE STUDY.

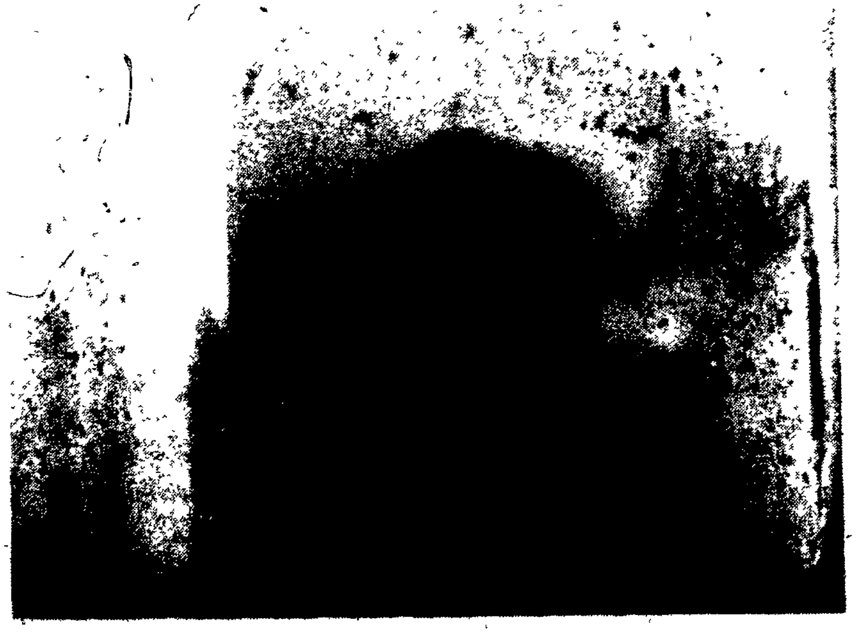

p2

p4

p3

THE SINGLE WIRE STUDY.

EXPERIMENT 2.

MATERIAL ; MANGANESE DIOXIDE.

2b ; 23.56 μm

Ha ; 2.4KOe

P2 – U_∞ – 0.61 cm/s.

P3 – U_∞ – 7.1 cm/s.

P4 – U_∞ – 18.9 cm/s.

P5

P7

P6

THE SINGLE WIRE STUDY.

EXPERIMENT 2.

MATERIAL ; MANGANESE DIOXIDE.

2b ; 23.56 μm

Ha ; 4.1 KOe

P5 – U_∞ – 0.61 cm/s.

P6 – U_∞ – 7.1 cm/s.

P7 – U_∞ – 18.9 cm/s.

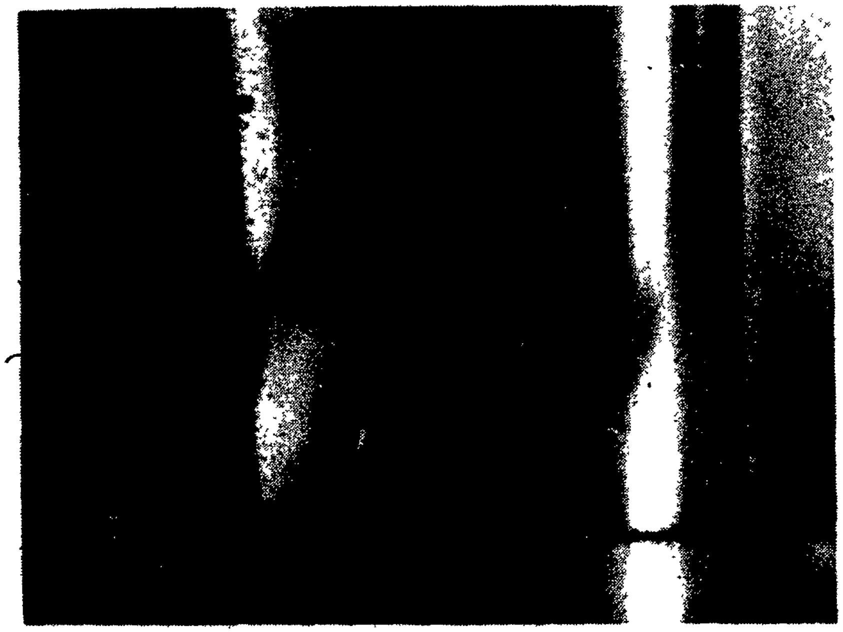

P8

P9

THE SINGLE WIRE STUDY.

EXPERIMENT 2.

MATERIAL ; MANGANESE DIOXIDE.

2b ; 23.56 μm

P8 - Ha ; 2.4 KOe. - U_∞ - 2.7 cm/s.

P9 - Ha ; 4.1 KOe. - U_∞ - 2.7 cm/s.

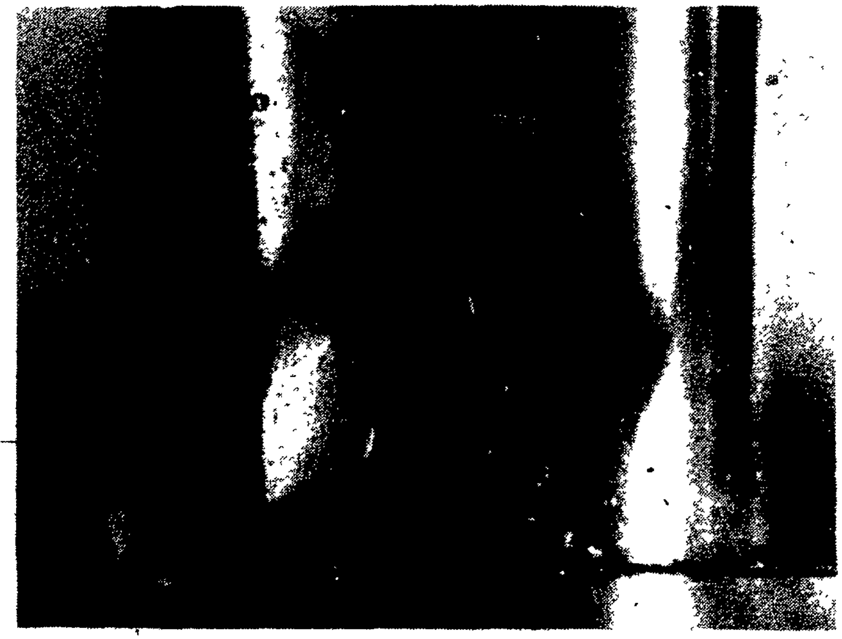

p_{10}

p_{12}

p_{11}

THE SINGLE WIRE STUDY.

EXPERIMENT 2.

MATERIAL ; MANGANESE DIOXIDE.

2b ; 23.56 μm

Ha ; 4.1 KOe.

P10 - U_∞ - 9.54 cm/s.

P11 - U_∞ - 14.86 cm/s.

P12 - U_∞ - 19.22 cm/s.

P13

P14

THE SINGLE WIRE STUDY.
EXPERIMENT 3.
MATERIAL ; HEMATITE.
2b ; 22.8 μm
Ha ; 3.5 KOe.
P13 – U_∞ – 4.09 cm/s.
P14 – U_∞ – 4.79 cm/s.

P_{15}

P_{17}

P_{16}

THE SINGLE WIRE STUDY.

EXPERIMENT 3.

MATERIAL ; HEMATITE.

$2b$; 22.8 μm

H_a ; 3.5 KOe.

P15 - U_∞ - 6.44 cm/s.

P16 - U_∞ - 8.89 cm/s.

P17 - U_∞ - 9.78 cm/s.

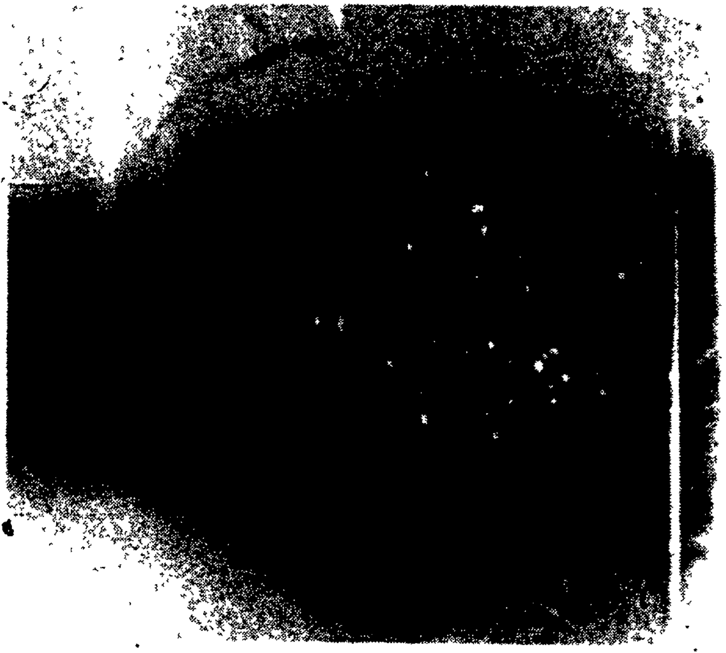

p18

p20

p19

THE SINGLE WIRE STUDY.

EXPERIMENT 4.

MATERIAL ; MANGANESE DIOXIDE.

2b ; 88.0 μm

Ha ; 3.5 KOe.

P18 - U_∞ - 6.44 cm/s.

P19 - U_∞ - 7.99 cm/s.

P20 - U_∞ - 8.89 cm/s.

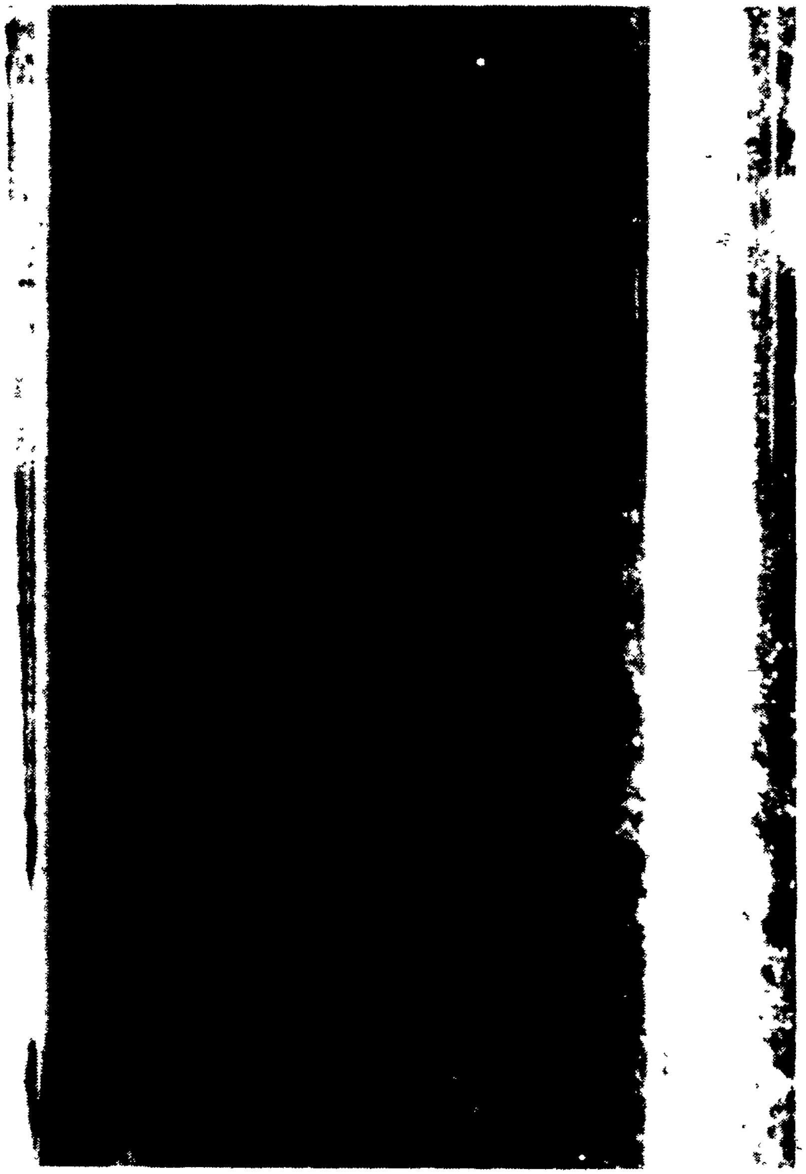

P22 SIDE VIEW

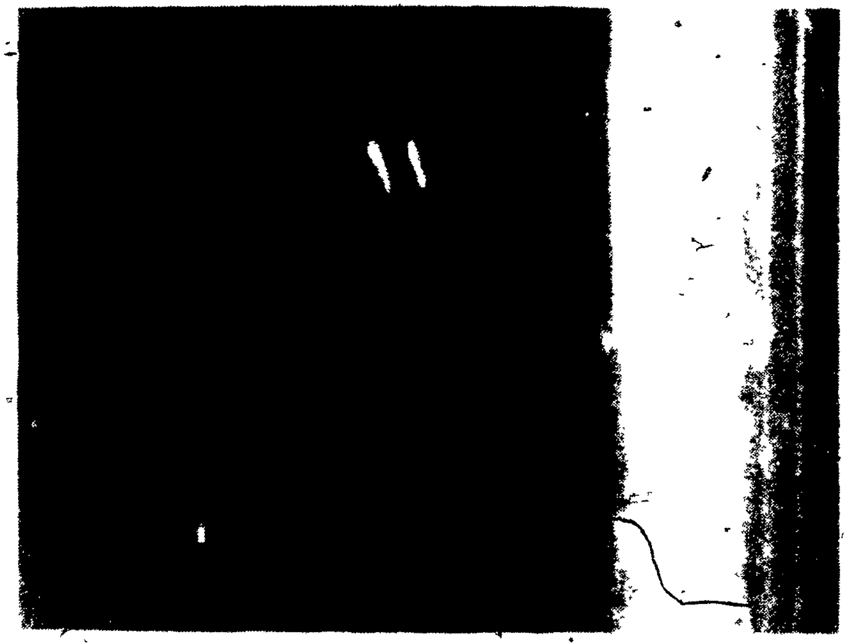

P21

THE SINGLE WIRE STUDY.

EXPERIMENT 5.

MATERIAL ; HEMATITE.

2b ; 5μm

Ha ; 3.5 KOe.

P21 - U_∞ - 7.99 cm/s.

N_L - 3.54

V_M/U_∞ - .06

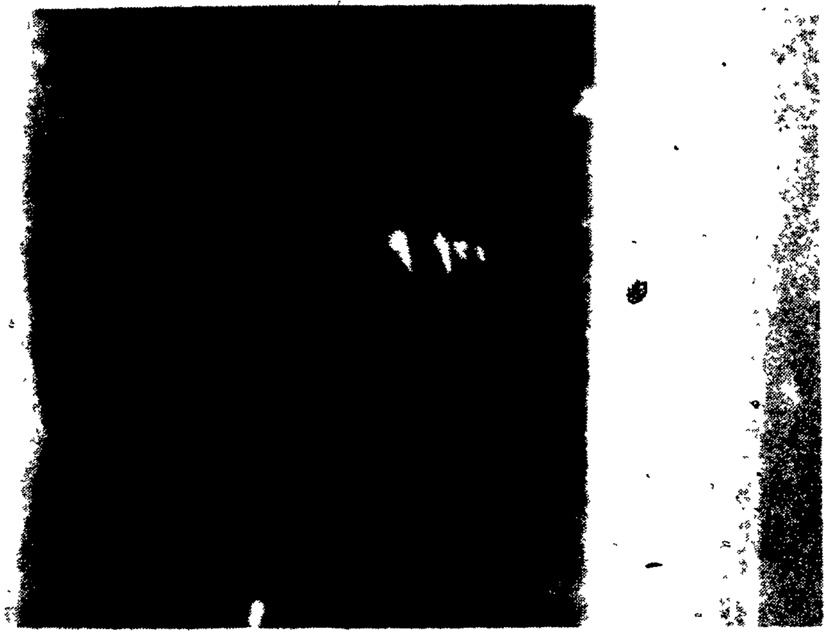

P23

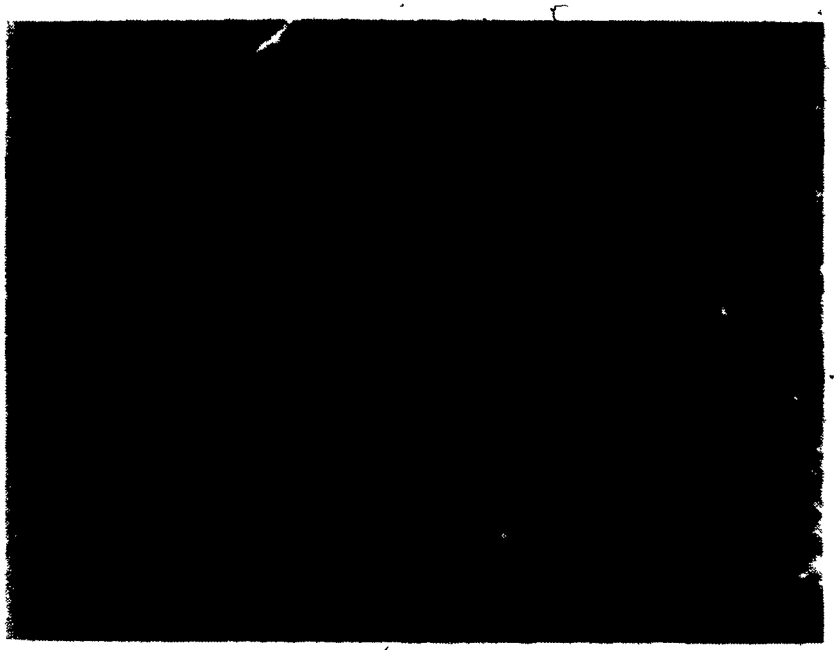

P24 SIDE VIEW

THE SINGLE WIRE STUDY.

EXPERIMENT 5.

MATERIAL ; HEMATITE.

2b ; 5μm.
Ha ; 3.5 KOe.

P23 - U_∞ - 11.17 cm/s.
N_L - 2.14
V_M/U_∞ - .04

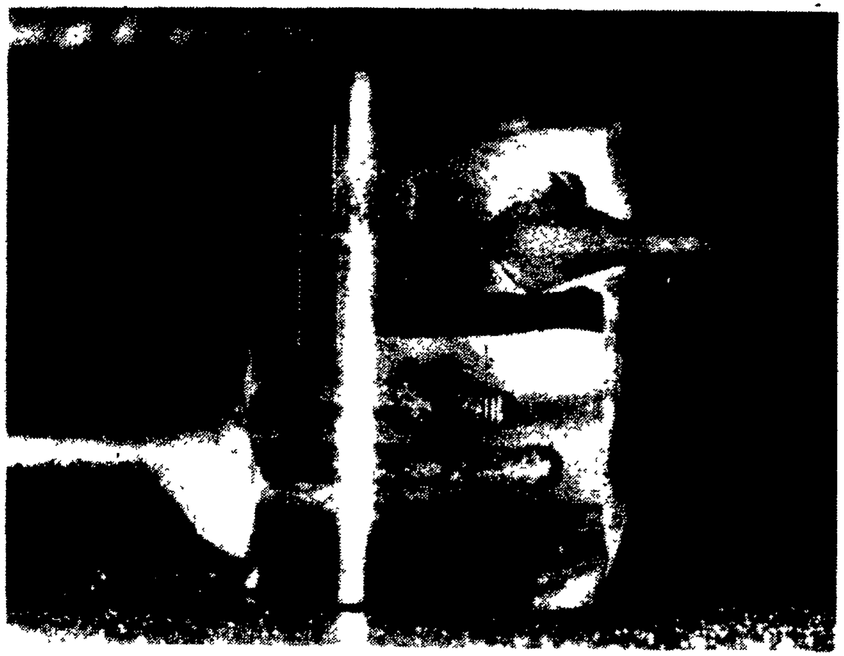

P25

P26

THE SINGLE WIRE STUDY.

EXPERIMENT 6.

MATERIAL ; MANGANESE DIOXIDE.

2b ; 23.56 μm

Ha ; 4.1 KOe.

P25 - BARE WIRE

P26 - U_∞ - 7.1 cm/s.

P_{27}

P_{28}

THE SINGLE WIRE STUDY.

EXPERIMENT 6.

MATERIAL ; HEMATITE.

2b ; 22.8 μm

Ha ; 3.5 KOe.

P27 - U_∞ - 4.79 cm/s.

P28 - U_∞ - 8.89 cm/s.

7.2 H.G.M.S. Results

Experiment 1

The results in Table 9 show a comparison of capture masses for the open (1) matrix and the closed matrix only. It is seen that the closed matrix caught more material than anticipated, by the loading equation using $\varepsilon = 0.7$. The open (1) matrix caught almost twice as much as predicted in some cases, and in every test, caught more material than the closed. Figures 35 and 36 show graphs of loading versus the Loading Number, N_L, and $\frac{V_M}{U_\infty}$, respectively for these results.

Table 10 and Appendixes 9a, 9b show the results of the comparison of all three matrices under the same conditions. It is seen that in all but two cases, the closed matrix caught more material than predicted using $\varepsilon = 0.7$. Under every test condition, the open matrices caught more than the closed, sometimes with up to three times as much captured than predicted.

On comparing the two open matrices, it is seen that at $N_L < 20$ the open (1) matrix captures slightly more material but above $N_L = 20$, the open (2) matrix generally captures more material.

Examining Figures 37 and 38, it is seen that γ_v for the closed matrix follows quite closely to the predicted value by the loading Equation with $\varepsilon = 0.7$. The open matrices follow a similar form to that of the closed but with $\varepsilon = 1.8$.

Experiment 2

On initial inspection of the weight of material caught (Table 11) it is seen that the open (1) matrix captures more material than the closed,

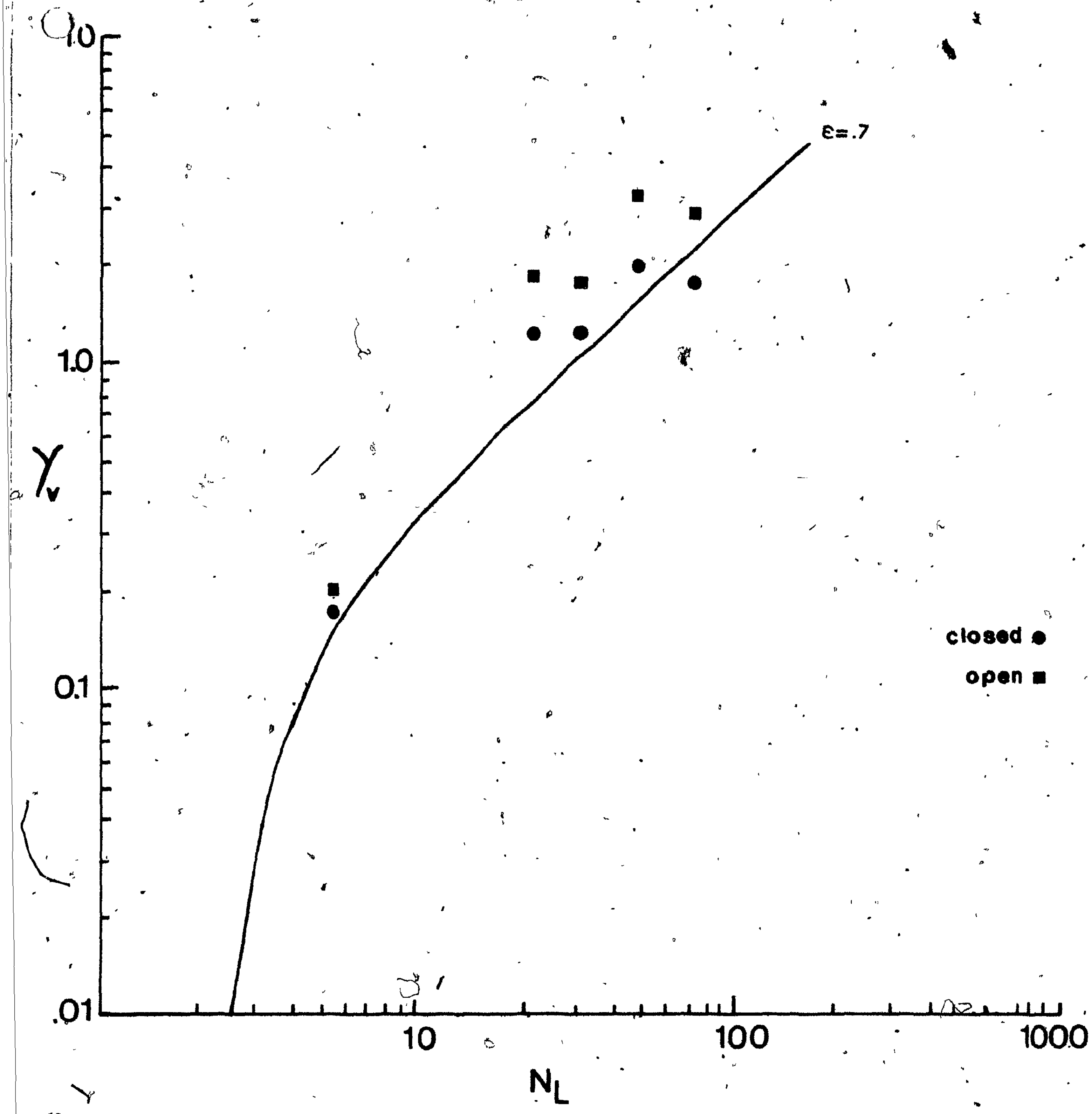

Fig.35 Graph Of Loading versus N_L.
A Comparison Of The Open(1) and The Closed Matrix.

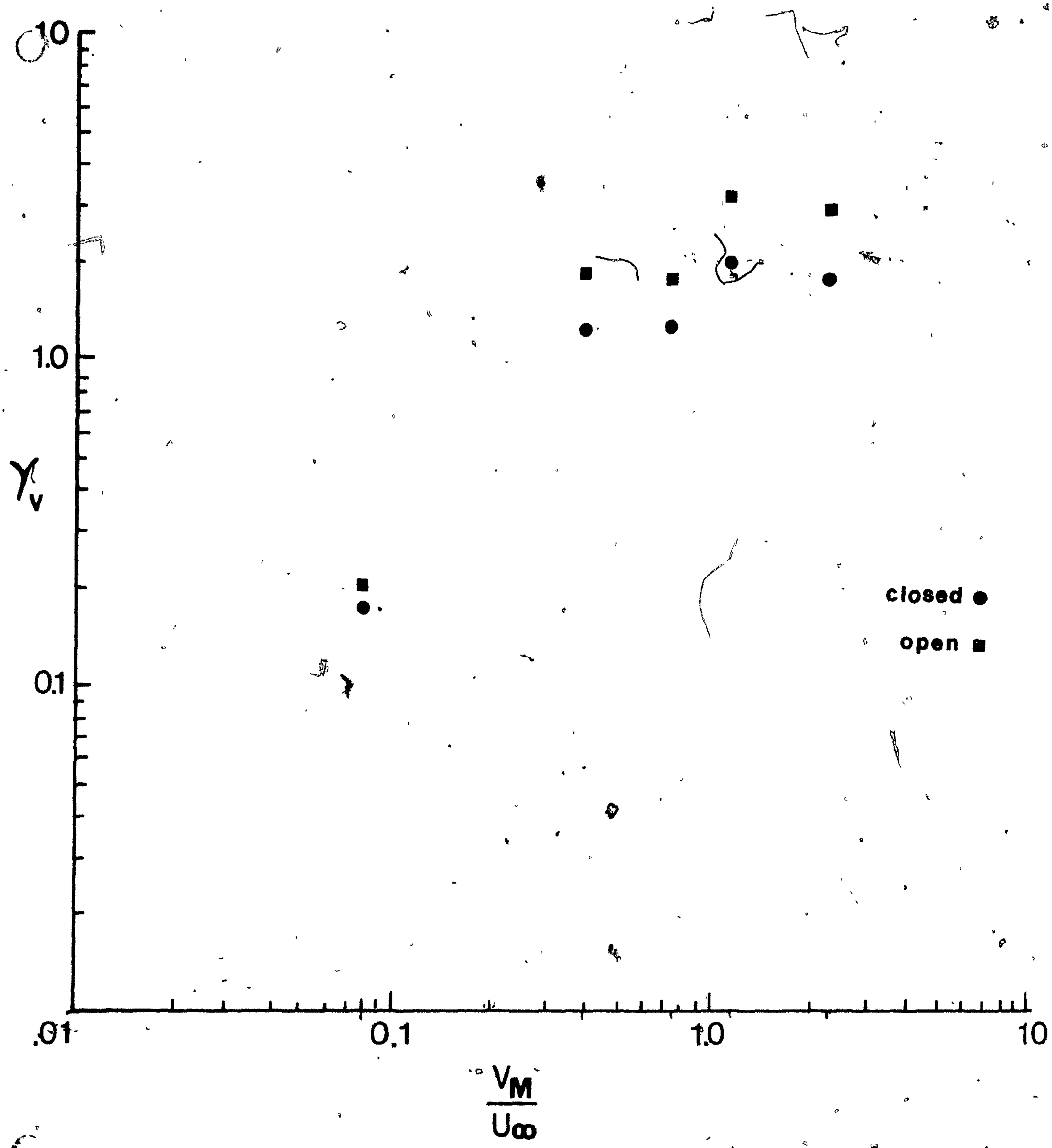

Fig.36 Graph Of Loading versus V_M/U_∞ .
A Comparison Of the Open(1) and the Closed Matrix.

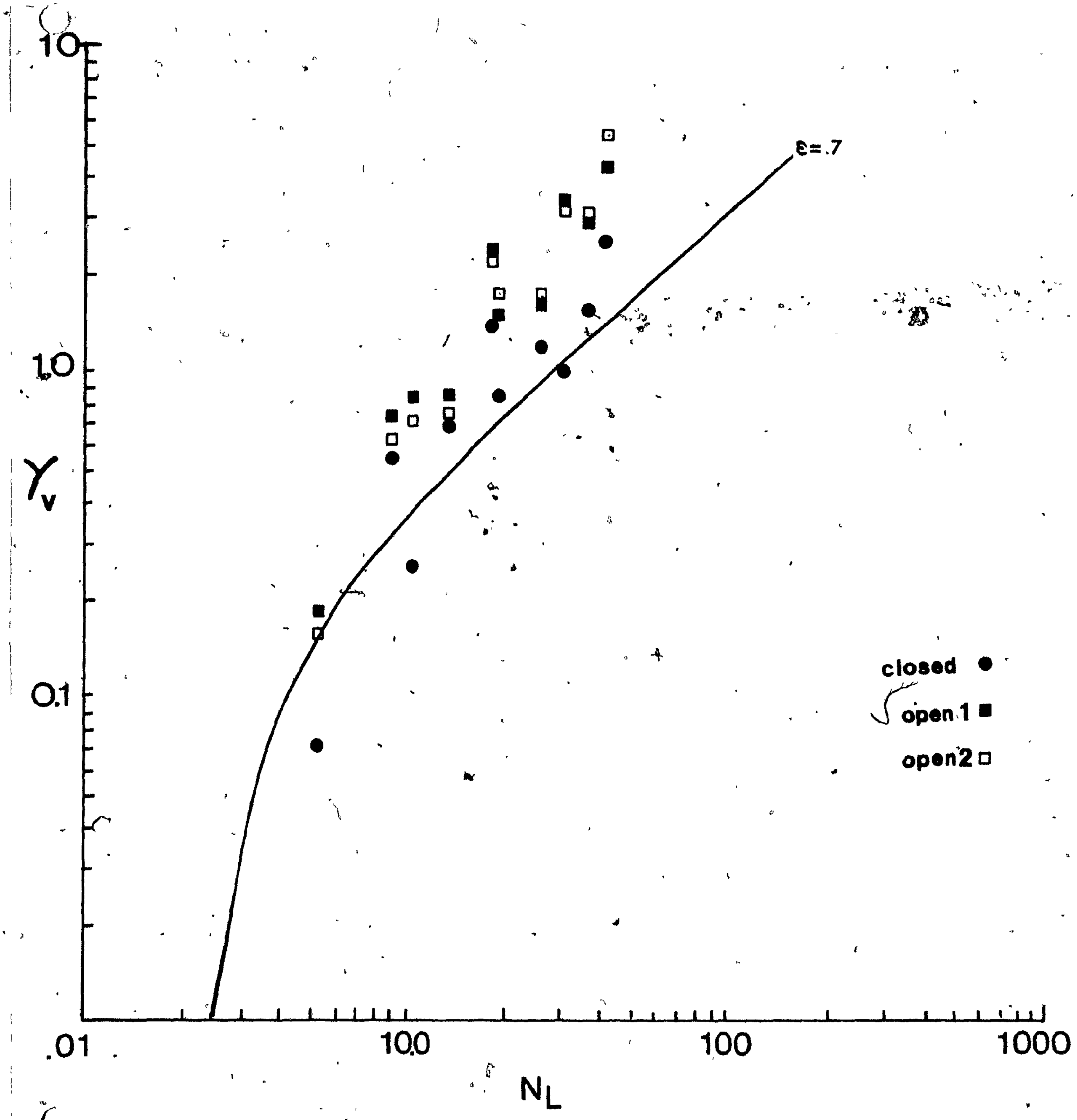

Fig.37 Graph of Loading versus N_L.
A Comparison of the Open(1),Open(2) and the Closed Matrices.

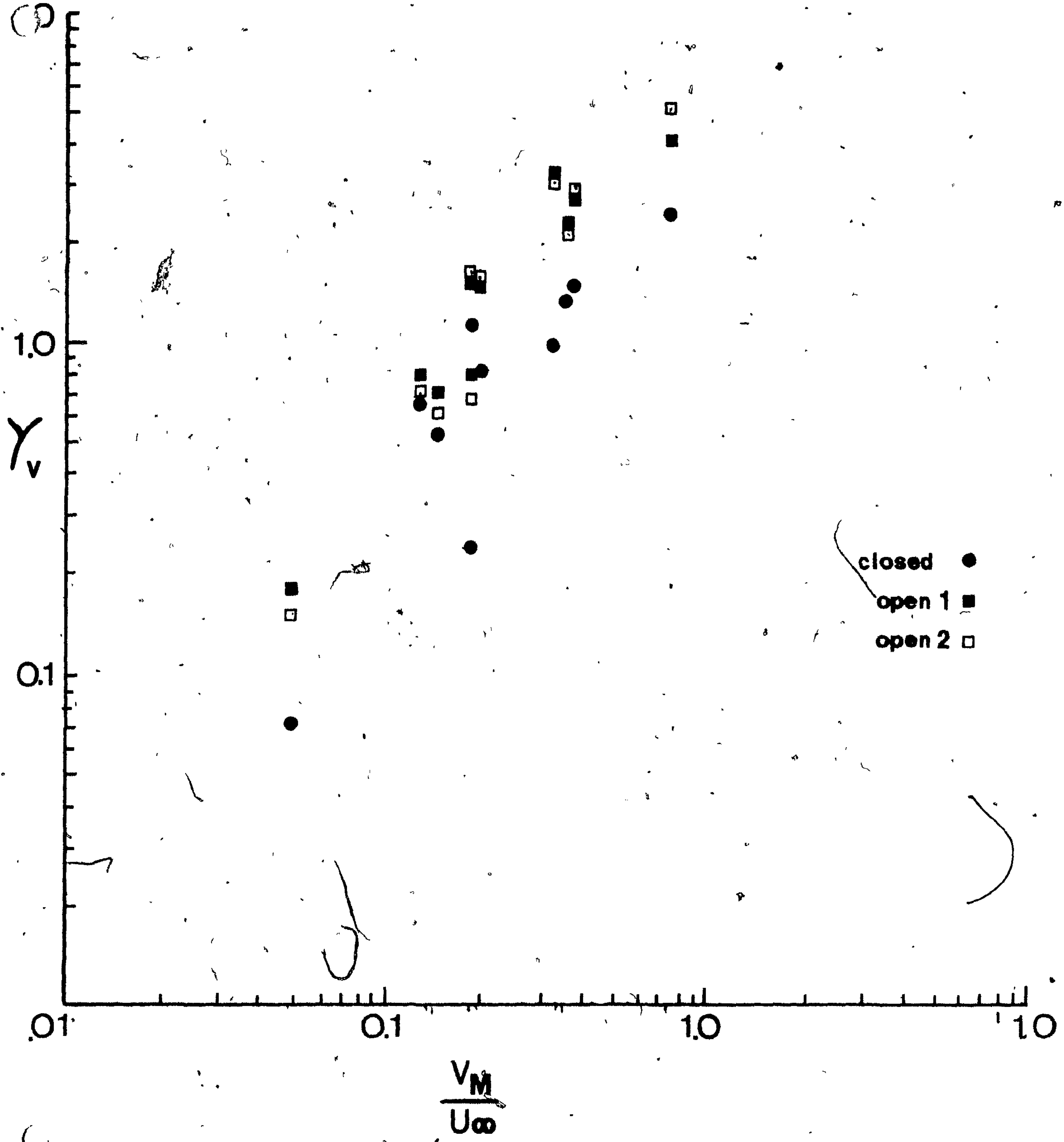

Fig.38 Graph of Loading versus V_M/U_∞ .
A Comparison of the Open(1),Open(2) and the Closed Matrix.

irrespective of the amount of material fed to the system. But, on considering the mass captured/unit volume of matrix it is seen that the closed matrix captures more (Figure 39). This figure also shows that both matrices capture their maximum amount of material at the same feed mass. Consequently the open matrix does not have a larger feed capacity than the closed matrix.

Experiment 3

As expected, the open matrix caught more material than the closed matrix (Table 12). The grade of this material appeared slightly lower, therefore recovery of hematite on each matrix was approximately the same. Therefore one could conclude that the open matrix caught more silica. However, the spread in the results (appendix 10) means that the difference is probably not significant.

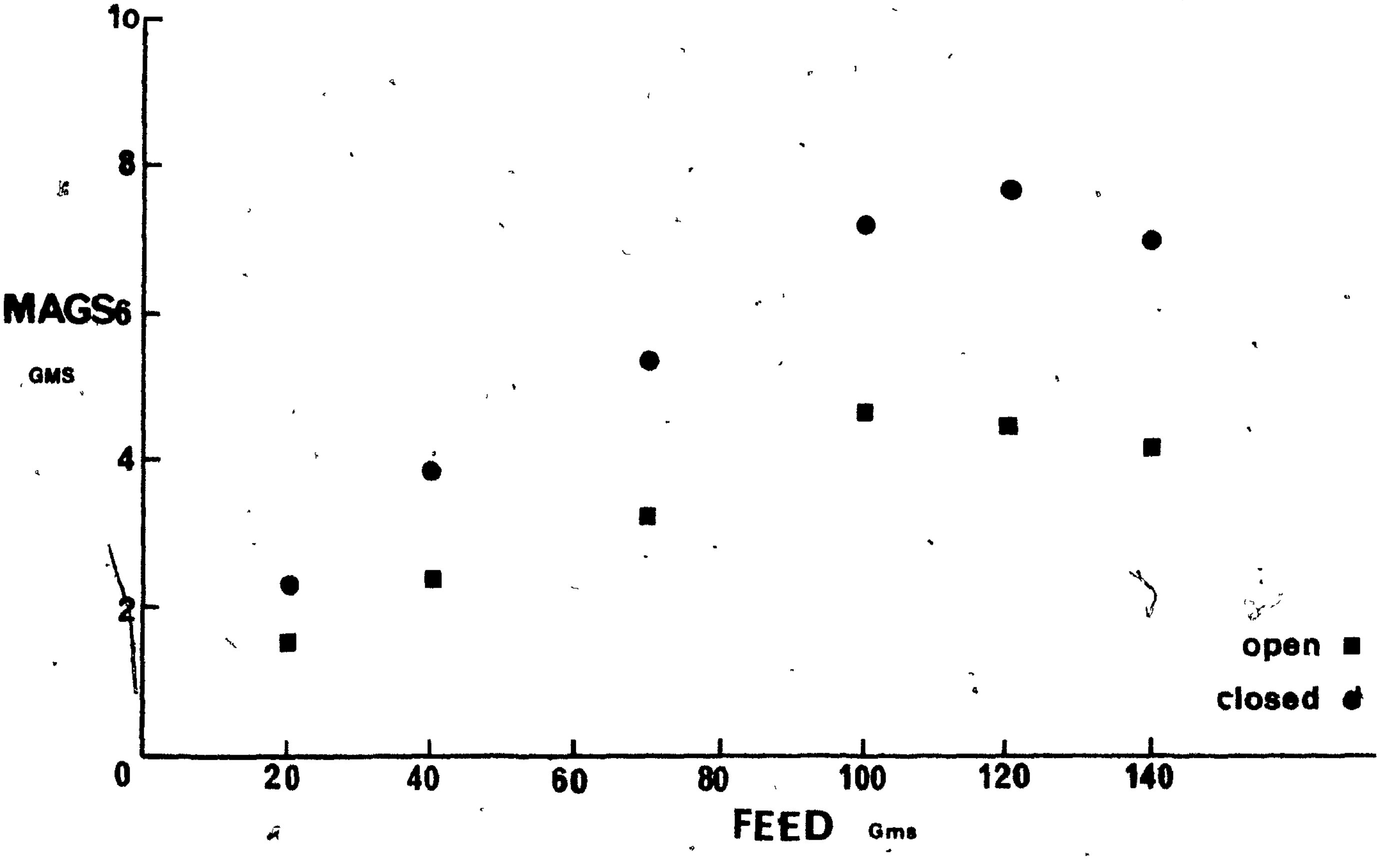

Fig.39 A Graph of Loading versus Feed Mass.

A Comparison of the Open (1) and the Closed Matrix (gms/cm^3 of matrix).

TABLE 9

Results - Experiment (1a)*

Material and Cone Size	Field KOe	Flow Rate (cm/s)	N_L	V_M/U_∞	$\gamma m \cdot W$ (gm)	Closed Matrix (gm)	Open Matrix (gm)
CuO #4	6.8	4.18	5.63	.08	.67	.78	.93
Fe_2O_3 #4	6.8	7.69	23.71	.40	3.36	4.6	6.91
MnO_2 #3	9.1	7.69	30.14	.76	4.03	4.5	6.23
Fe_2O_3 #3	9.1	7.69	47.25	1.16	6.33	7.4	11.83
MnO_2 #2	13.8	7.69	70.65	2.37	8.57	6.4	10.33

W = weight of matrix

$$\gamma m = \frac{\varepsilon}{4}\left\{\left(\frac{N_L}{2.5}\right)^{4/5} - 1\right\} \qquad (21)$$

where $\varepsilon = 0.7$

* all tests performed at CANMET, using a Sala Magnetics 10-15-20 laboratory unit.

TABLE 10

Experiment 1b

H.G.M.S. RUNS

MAGS - in grams

V_M/U_∞	N_L	γ_m	Closed	Open (1)	Open (2)
0.14	9.14	1.22	2.01	2.67	2.38
0.10	13.54	1.83	2.41	2.94	2.60
0.18	26.23	3.70	4.40	5.85	6.30
0.35	36.58	5.04	5.57	10.5	11.60

TABLE 11

Experiment Two

Feed Mass	MAGS Open (1) (gms)	MAGS Closed (gms)	Mass/Unit Vol. of Matrix Open (1)	Mass/Unit Vol. of Matrix Closed
20	4.18	2.32	1.39	2.32
40	7.09	3.92	2.36	3.92
70	9.53	5.35	3.18	5.35
100	13.89	7.20	4.63	7.20
120	13.10	7.66	4.37	7.66
140	12.40	6.96	4.13	6.96

TABLE 12

Grade Experiments

MATRIX	MAGS gms	NMAGS gms	GRADE	RECOVERY
Open	2.43 ±.15	3.25	79.8 ±.95	61.21 ± 2.24
Closed	2.24 ±.10	3.30	81.83 ±2.24	61.39 ± 2.94

(See Appendix 10)

VIII. DISCUSSION

The object of the study was to examine the build-up process of magnetic particles on a single wire in order to study front versus back capture and the profiles under various test conditions. This information was then correlated with previous work carried out by other workers, in order to try to obtain a definitive picture of the capture mechanisms involved in hgms.

8.1 The Build-Up Profile

8.1.1 Back Capture

Obtaining profiles consisting of mostly back capture was very unexpected in experiments two and five. Of the previous works, only the theoretical studies of Luborsky and Drummond(11), Stekly and Minervini(16) along with the photographic evidence of Friedlaender(30) had suggested that back capture would occur.

The shape of the back profile achieved under the various test conditions, could be correlated qualitatively with the fluid flow characteristics. The Reynolds Number of the wire was determined for each of the flow velocities used in the experiments, along with the corresponding θ_A and L* values as given by Brauer (39) (Table 5). Initially the values of θ_A and L* were compared with the angle and length of build-up observed. It may be seen that the angle of build-up predicted for a flow velocity of .71 cm/s is only 22° . In the corresponding photograph i.e. P2, the angle is seen to be nearer 80-90°. This may be explained by the fact that the Reynolds Number at .71 cm/s is only ~5.58

and the lower limit of the applicability of θ_A is $Re_w = 6.23$. This limit is due to there being no boundary layer separation from the wire at $Re_w < 6.23$ (39). In Clift, Grace and Weber,(38) a value of $Re_w \sim 5$ is given for the limit of boundary layer separation . Whether boundary separation occurs or not, it is apparent that the magnetic field dominates the shape of the build-up and not the fluid forces. Consequently, build-up extends out from behind the wire into the flow stream due to the attractive magnetic forces on the particles being much greater than the drag forces attempting to move the particles downstream.

Again, L* is only applicable once boundary separation has occurred. It is clearly seen, that the build-up extends further than .0036 mm (Table 5) downstream. Once again this is due to the magnetic force holding the particles at the wire being much greater than the drag force exerted by the fluid.

Two build-up profiles were obtained using a flow rate of 7.1 cm/s ($Re_w = 63.5$), one with a field of 2.4 KOe and another at 4.1 KOe. Examining photograph P3 (2.4 KOe) initially, there is a marked change in shape from photograph P2. The build-up length is slightly diminished behind the wire, and the rounder appearance of the profile has changed to one with straight sides.

The angle of boundary separation given by θ_A is 59° which appears to agree well with the downstream build-up angle. Thus, at angles greater than 59° , there are strong drag forces acting, which direct particles arriving at the wire, downstream. Within the area of boundary separation there exist oscillating vortices, some of which will be breaking free to travel downstream.

Consequently, the shape of the build-up may be explained by assuming at angles of $\theta > 59^{o}$, the fluid drag force acting on the particles is greater than the attractive magnetic force holding the particles at the wire. Therefore, the particles are carried away downstream, around the perimeter of the boundary layer.

At $\theta < 59^{o}$, the magnetic field holds the particles in place, unless vortex shedding disturbs the fluid in the wake behind the wire. In P3, there is a slight decrease in build-up length possibly correlating with the onset of vortex shedding. Vortex shedding could cause particles to overcome the magnetic force holding them in position so allowing them to travel downstream.

Considering photograph P6 (4.1 KOe) a similar shape is obtained to P3, but the sides of the build-up are not as straight. It would appear with the higher magnetic field, the magnetic force is strong enough to hold the particles in position at $\theta > 59^{o}$, i.e. the magnetic force attracting the particles is now resisting the fluid drag force, to a certain extent, outside the protective wake area.

The same qualitative conclusion may be arrived at on comparing P4 and P7, which are both taken at 18.9 cm/s ($Re_w = 172$) with P4 at 2.4 KOe and P7 at 4.1 KOe. Here the flow conditions behind the wire are more turbulent. θ_A is about 70^{o}, but at $Re_w > 160$, the instationary double vortex in the wake breaks down and instationary single vortices form, accompanied by turbulent fluctuations associated with the vortex shedding. The build-up length downstream is therefore decreased drammatically due to this turbulence. (As mentioned earlier, L* does not control the build-up profile as it increases as the build-up length decreases).

From P4 and P7, it is seen that the straight sided build-up associated with θ_A, is seen in both cases; the higher field strength profile again apparently showing more resistence to the drag force outside the boundary layer.

Photographs P8 - P12 were used for verification of two points:

a) At higher magnetic fields, the attractive force holding the particles to the wire could overcome the drag forces acting outside the boundary layer, and

b) The length of back build-up could be correlated with the rate of vortex shedding given by the Strouhal number.

Photographs P8 and P9 illustrate the first point very well, with the back build-up extending out from behind the wire at the higher field strength.

Photographs P10 - P12 show the profiles observed at 4.1 KOe and flow rates of 9.5, 1.48 and 19.2 cm/s.

In each of these photographs the build-up angle is approximately the same, corresponding to a range in theoretical θ_A from 62.7° - 69.8°. Whether the build-up angles conform to θ_A or the limiting angle given by the magnetic force, is therefore inconclusive.

The area of the build-up downstream in addition to the build-up length decreases as expected with increasing flow rate. This does appear to be due to the increasing rate of vortex shedding (point b). The value of the Strouhal number and therefore the rate of vortex shedding is shown in Table 6 for each of the flow rates used in experiment two, and appears to correlate very well with the decreasing build-up length.

The effect of the vortex oscillations and increasing shedding is shown on each of the photographs by the movement of large amounts of particles apparently shedding from their capture positions on the back of the wire. As this occurs more frequently with increasing Strouhal number, the build-up at the back of the wire decreases. Another reason suggested for the decreasing back build-up is that the higher the flow rate, the less chance the particles have of getting into the downstream capture region. This is due to the increasingly strong drag forces outside the boundary layer region which drags them strongly downstream.

In experiment five, P21 - P24, the shapes of the back profiles have unfortunately become masked due to end effects. Consequently, this made analysis of the shape of the back profile impossible. It is interesting to note, however, that the presence of the end effects allow back build-up to extend out from behind the wire at higher flow rates than in experiment two.

The use of θ_A, the boundary layer separation angle, in predicting the angle of back build-up appears to be inconclusive in this study. However, on calculating θ_A for some runs carried out by Friedlaender, it is seen that the separation angle can influence the back build-up, even to limiting the build-up angle to 28° (Figure 40).

8.1.2 The Effect of Front Build-Up on the Back Build-Up Profile

The effect of front build-up on the back build-up profile is very dependent on the extent to which the front build-up is present.

a/

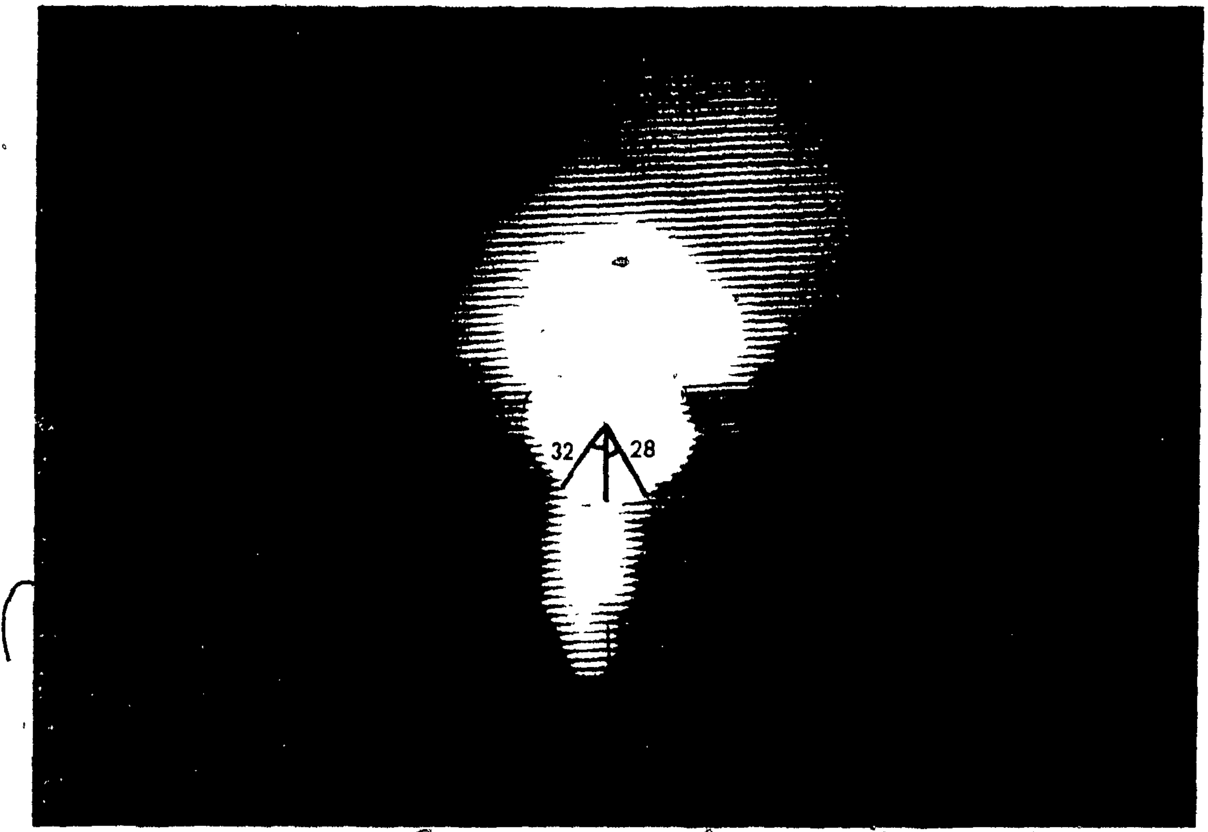

Fig.40 Correlation of θ_A and Friedlaenders Observed Profiles.

Test Conditions:- Ha = 5 KOe ; κ = 307.9 emu/cm^{3}Oe ; ρ_p = 3.71 g/cm^3

ν = 0.01 cm^2/s ; 2b = 8 μm ; 2a = 125 μm ; M_s = 484 emu/cm^3; K = 34.9 Oe^{-1};

U_∞ = a/ U_∞ = 7.9 cm/s, θ_A = **28°**

b/ U_∞ = 2.9 cm/s, θ_A = — Re . 6.23

c/ U_∞ = 23.3 cm/s, θ_A = **49°**

(SEE OVERLEAF)

b/

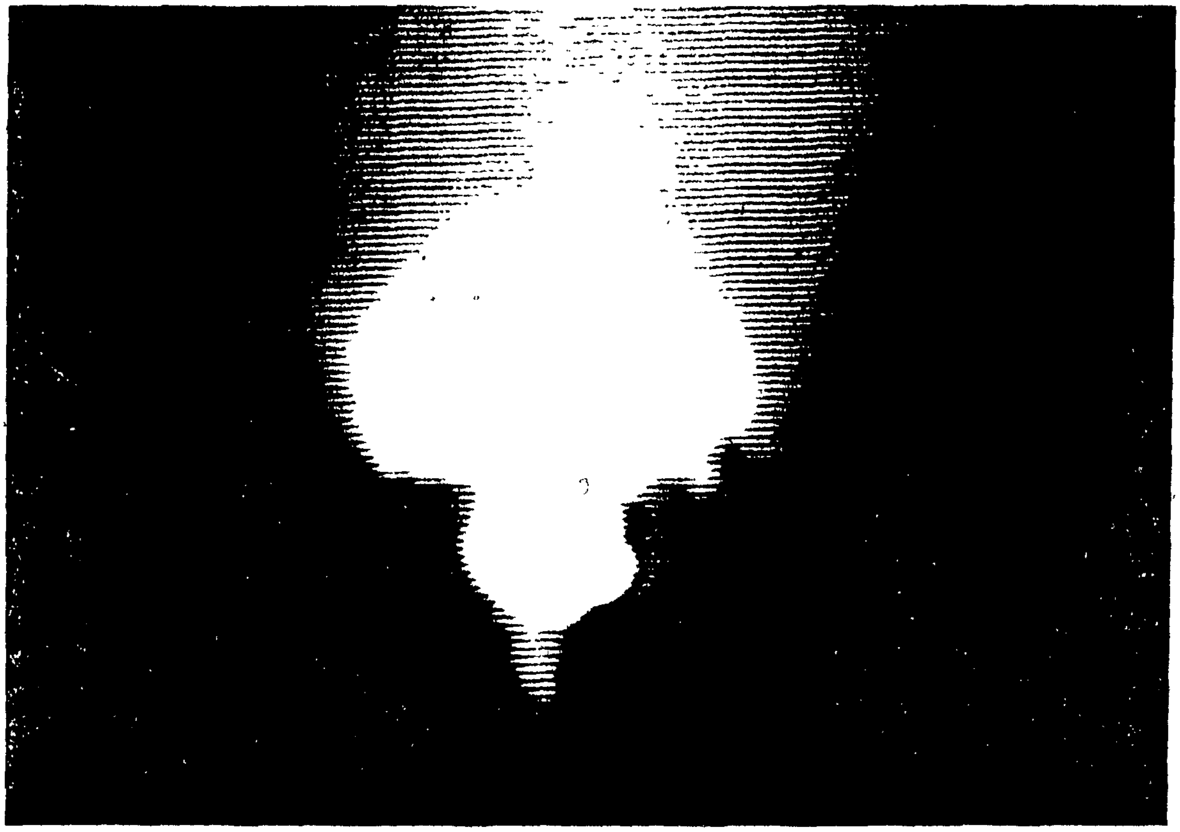

c/

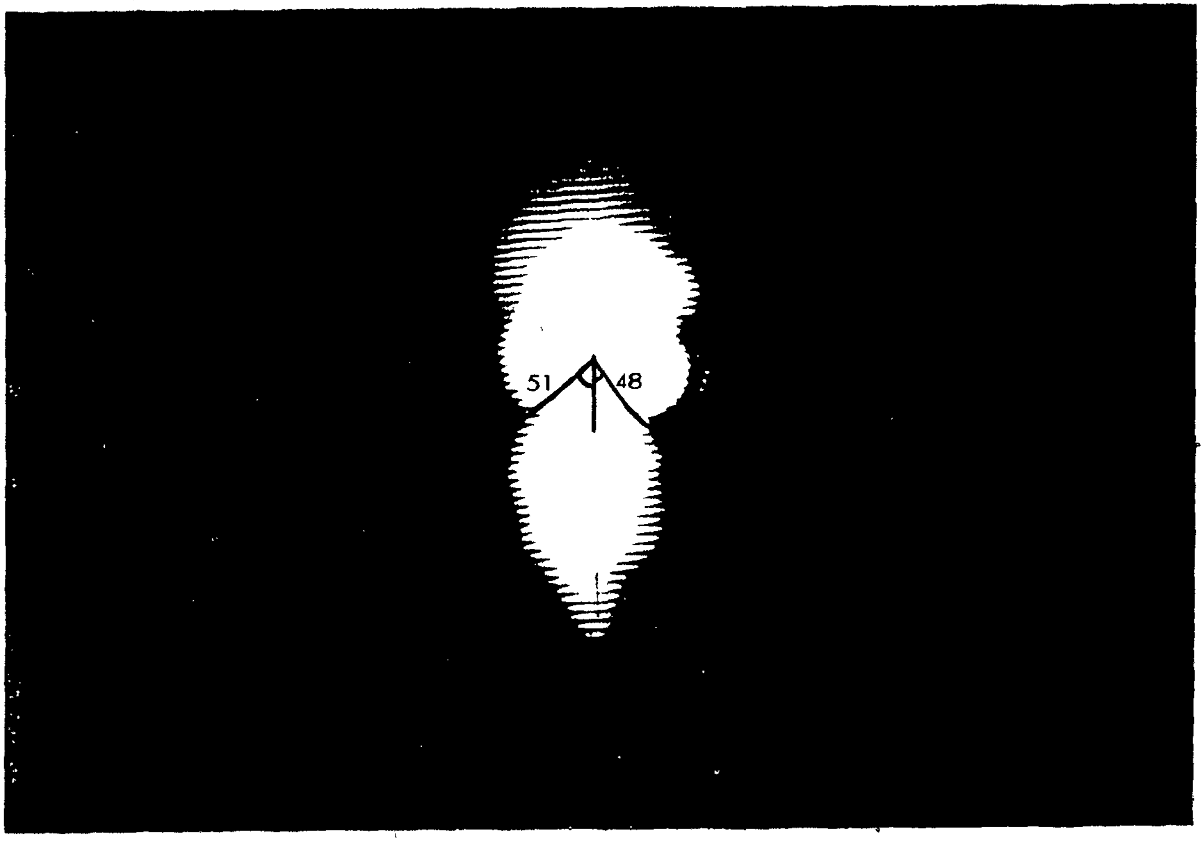

Photograph P13 shows a rounded back build-up extending horizontally out from the back of the wire. This is a very different profile to that of, for example, P6 which is taken under similar conditions but with no front capture present. This is because the wake formed by the front build-up protects the back build-up from the fluid drag forces. Consequently, the back build-up can extend out from behind the wire at much higher flow rates than is possible when no front build-up is present.

In photograph P14, the extension of the back build-up from behind the wire is even greater, although the amount of front build-up has decreased to a position where capture occurs evenly on both the front and back of the wire. It is noted, however, that the back build-up does not extend out further than the front profile, the depth of the build-up accommodating most of the extra capture.

On increasing the flow rate from 4.79 cm/s (P14) through to 9.78 cm/s (P17) a distinct change appears in the shape of the back profile, the decreasing amount of front capture affording the back build-up less shelter from the fluid forces as the velocity increases. Consequently, it is seen that the back build-up profile extends a shorter distance from behind the wire in P15 and P16. In photograph P17, the protection afforded by the front build-up is minimal and the more straight-sided profile is seen once again on the back build-up.

In experiment four, using the large 88μm manganese dioxide, the front capture never extended out very far from the edge of the wire and therefore gives the back build-up very little protection (P18 - P20). Consequently, the back profile does not extend out from behind the wire and appears very straight edged conforming to the shape of the wake.

It may again be seen in these three photographs, how the back build-up length decreases as the flow rate increases.

8.2 Mechanism of Back Capture

Stekly and Minervini(16) were the first workers to predict copious amounts of back capture in an hgms. Although not describing the method by which particles arrive at the back of a wire, from Figure 6, it may be seen that the particle trajectories that lead to back capture originate in the void regions at the sides of the wire.

In their work, Luborsky and Drummond(11) predict large amounts of back capture without defining the mechanism with which the particles arrive there. They do suggest that the particles arrive by being swept off the front build-up or by being caught up in the turbulent wake of the wire.

Friedlaender concluded from his photographic studies(30) that the particle profiles, both upstream and downstream, were dependent on the slurry velocity. At a slow velocity, particles would collect only on the upstream side of the wire. As the slurry velocity increased, particles would also collect on the downstream side and if the flow rate was higher enough, particles would not collect on the upstream side at all. No suggestion as to the mechanism of these capture modes was suggested.

Birss, Dennis and Gerber (18) concluded from their study, that particles could only be caught on the back of the wire if they could be brought out of their expected positions at the front of the wire into the void regions. From this new position, trajectories could carry the particles to the back of the wire. (Figure 9)

This study supports two mechanisms suggested for back capture, which appear to operate under conditions given by the $\frac{V_M}{U_\infty}$ ratio :

a) At low $\frac{V_M}{U_\infty}$ ratio ($\leqslant .8$), the mechanism for capture appears to be one of direct trajectory to the back of the wire. For example, in experiment two and in some runs of experiment six, no top capture was seen at all, all particles being caught on the back of the wire.

b) At a $\frac{V_M}{U_\infty}$ rate $\geqslant 0.8 - 1.0$, particles do appear to be lost from the front of the wire, to be caught again on the back. A good example of this are photographs P13 and P14.

Photograph P13 shows a well defined front build-up with straight edges. An increase in flow velocity of only $\simeq 0.7$ cm/s result in photograph P14 where the straight, well defined perimeter of the front build-up appears to have had particles removed and there has been a marked increase in back capture.

It would consequently appear that both Luborsky and Drummond, and Birss, Dennis and Berber were correct in their assumptions, although neither postulated that capture on only the downstream side of the wire would occur.

The grade experiments were dissappointing in fact they did not help in deciding whether back capture was a magnetic or flow phenomenon.

A drop in grade on the open matrix would have suggested that the particles were indiscriminately caught at the back of the wire, indicating the fluid carried the particles there.

An increase in grade would suggest the particles were magnetically carried to their positions at the downstream side of the wire.

8.3 The Profile of Front Capture

The profiles of the front capture observed in the experiments may be divided into two cases.

i) A prominent fan shaped build-up with well defined build-up angles e.g. P13.

ii) A more rounded "collar" shaped build-up, with poorly defined build-up angles e.g. P18 - P20.

The well defined fan shaped build-up (P13) is very similar to the theoretical shape predicted by Nesset for the same conditions shown in Figure 41a. He predicted the build-up angles at the front of the wire to be somewhat greater than 90° when the field is below that for wire saturation. In photograph P13, the angle of build-up is approximately 120° which supports this prediction.

In photograph P14, the fan shaped build-up may be seen to be breaking down. This photograph is taken at a slightly higher flow rate than P13. The fan shaped build-up is not seen again at higher flow rates. Consequently, with the 20μm (cone #2) hematite, fan shaped build-up is seen at flow rates <4 cm/s but above this velocity, the sharp definition of the profile is lost.

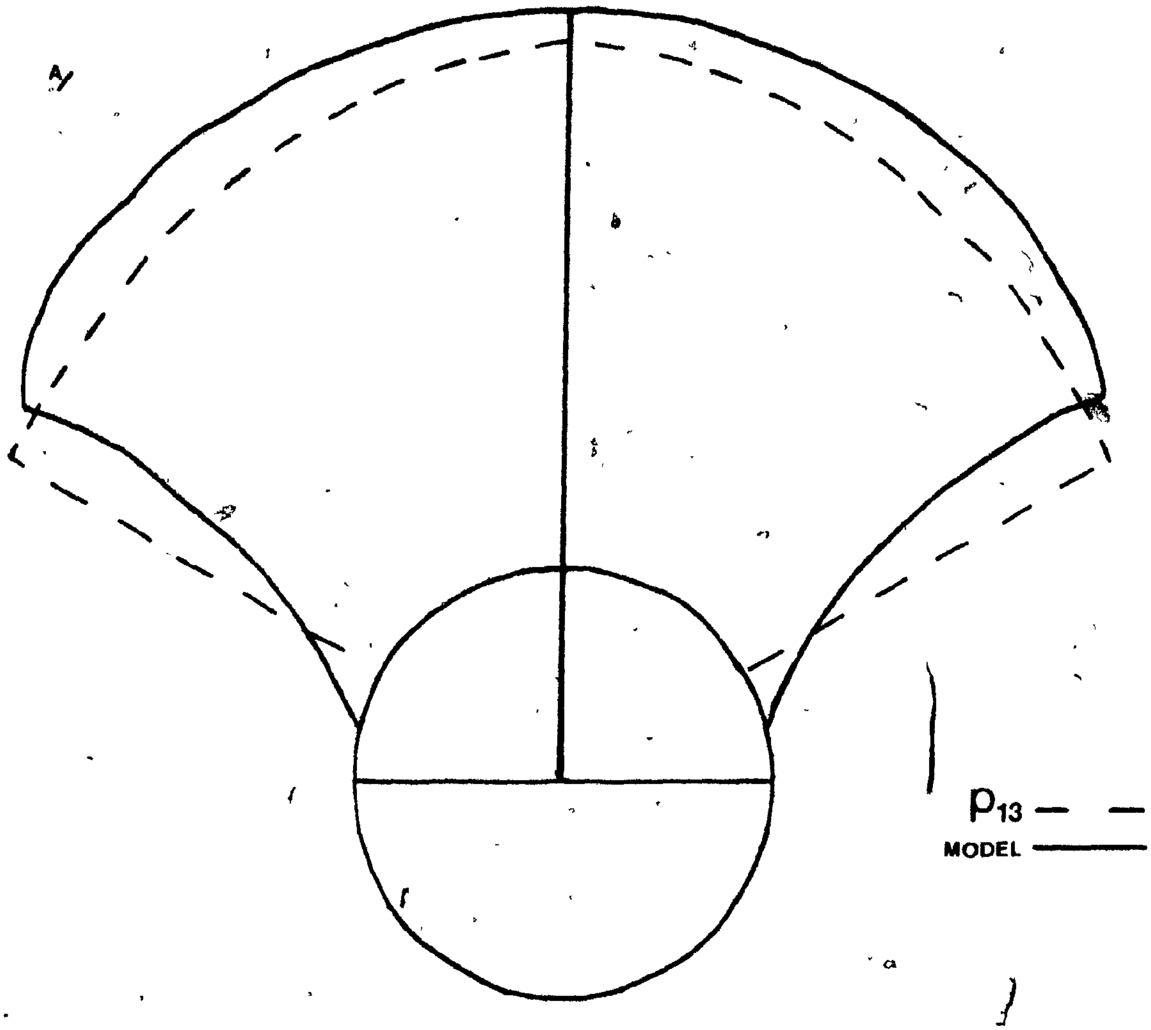

Fig.41 Nesset's Model Prediction For the Profiles of Photographs P13 & P17 and for a Theoretical Flow Rate of 18.9 cm/s,(Front Build-up only).

(See Overleaf)

B/

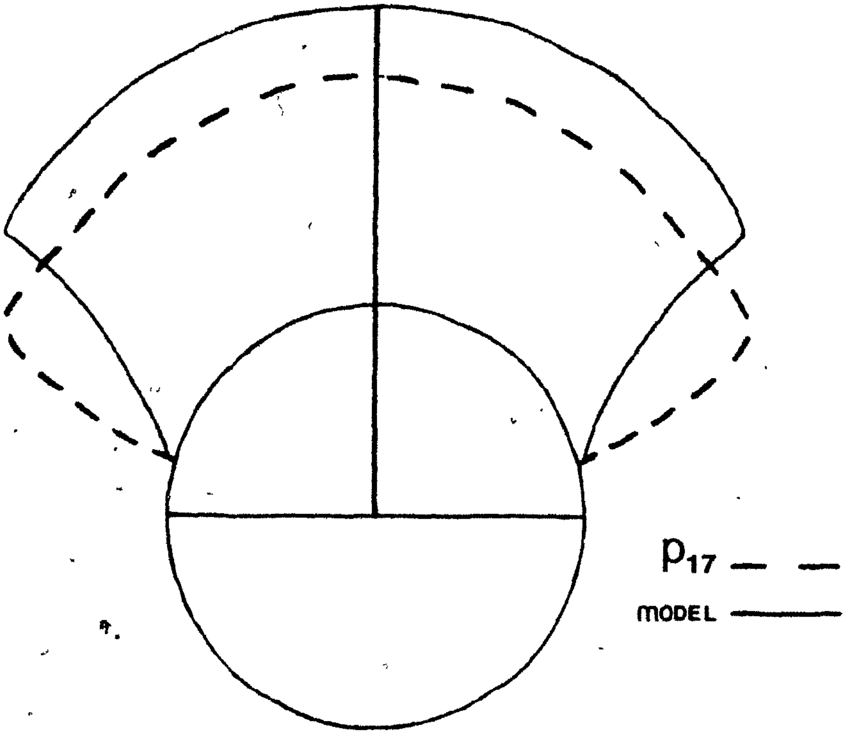

C/

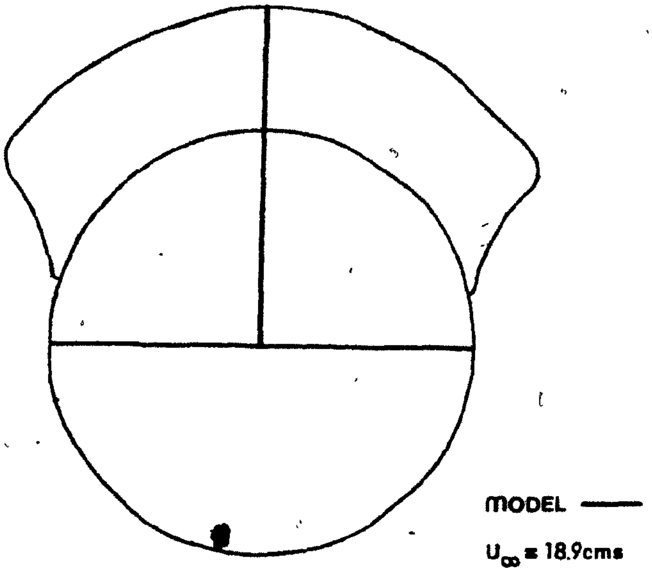

As the fan shaped build-up breaks down, the outer edge of the build-up becomes rounded and appears as a 'collar' around the top of the wire. Nesset predicted a less fan shaped build-up at higher flow rates, as is seen from Figures (41b) and (41c), but the actual build-up is more rounded than he predicted. This occurence was suggested by Nesset due to the 'fan shape' being a theoretical build-up shape with no allowance for flow instabilities which would occur in a real system.

The photographs also agree well with the photographic evidence of Friedlaender et al(31) which also shows a more rounded build-up at higher flow rates or lower field strengths (Figure 40).

8.4 Front Versus Back Capture

It is seen that for cone #2 manganese dioxide (experiment two), the build-up is dominated by back capture; indeed front capture while present (see P2, P3) was too small to conveniently quantify. Although not applicable to back capture, loading was plotted against N_L (Figure 29), as well as $\frac{V_M}{U_\infty}$. Figure 30 shows that correlation is better with $\frac{V_M}{U_\infty}$. For example, significant back loading occurs below the theoretical minimum N_L of 2.5. Also, the amount of back capture is approximately constant over a wide range of N_L, i.e. $6 < N_L < 150$. It should again be noted that the loading equation was derived assuming no back capture occured.

Figure 30 shows that when plotted against $\frac{V_M}{U_\infty}$, the loading follows a reasonably smooth curve, build-up reaching a maximum at a value of $\frac{V_M}{U_\infty} \simeq 0.25$.

In experiment three (22μm, cone #2, hematite), N_L may be seen to predict the loading curve for both front and total capture if ϵ is fitted to the experimental data and is not used as a packing fraction (Figure 31). Consequently, if $\varepsilon \neq 1.0$ (as for the packing fraction shown on the prints) but equals 1.3 and 2.2, the resulting curves describe front and total build-up well.

Considering Figure 32, it is seen that >50% of capture is on the downstream side of the wire when $\frac{V_M}{U_\infty} < 0.9$. As the value of $\frac{V_M}{U_\infty}$ decreases, the % of the total capture on the back of the wire increases much more.

In experiment four (88μm manganese dioxide), it may be seen from Table 8 that front capture is always the dominant (> 50% capture) capture mode. By plotting a graph of % front capture for experiment two, three and four against the $\frac{V_M}{U_\infty}$ ratio, a curve is obtained as Figure 42. It is seen that there appears to be a value for all the experiments which govern whether front or back capture will be dominant (and also perhaps to what extent). This value would appear to be ~ 0.9.

The only exception to this is that of P2, which has a flow velocity of 0.61 cm/s which produces a Re_w of ≈ 5.5. At such a value, the flow conditions are uncertain about the wire and therefore parameters affecting the build-up may be very different to those at higher flow rates.

A maximum amount of back capture does not appear to be achieved in experiment four, although the $\frac{V_M}{U_\infty}$ value is greater than those in the previous experiments where a maximum was obtained. It is believed that a maximum amount of back capture is achieved but as yet is not correlated with either N_L or $\frac{V_M}{U_\infty}$.

The front and total build-up of material is again reasonably described using the Loading Equation with ε as a fitted parameter. With

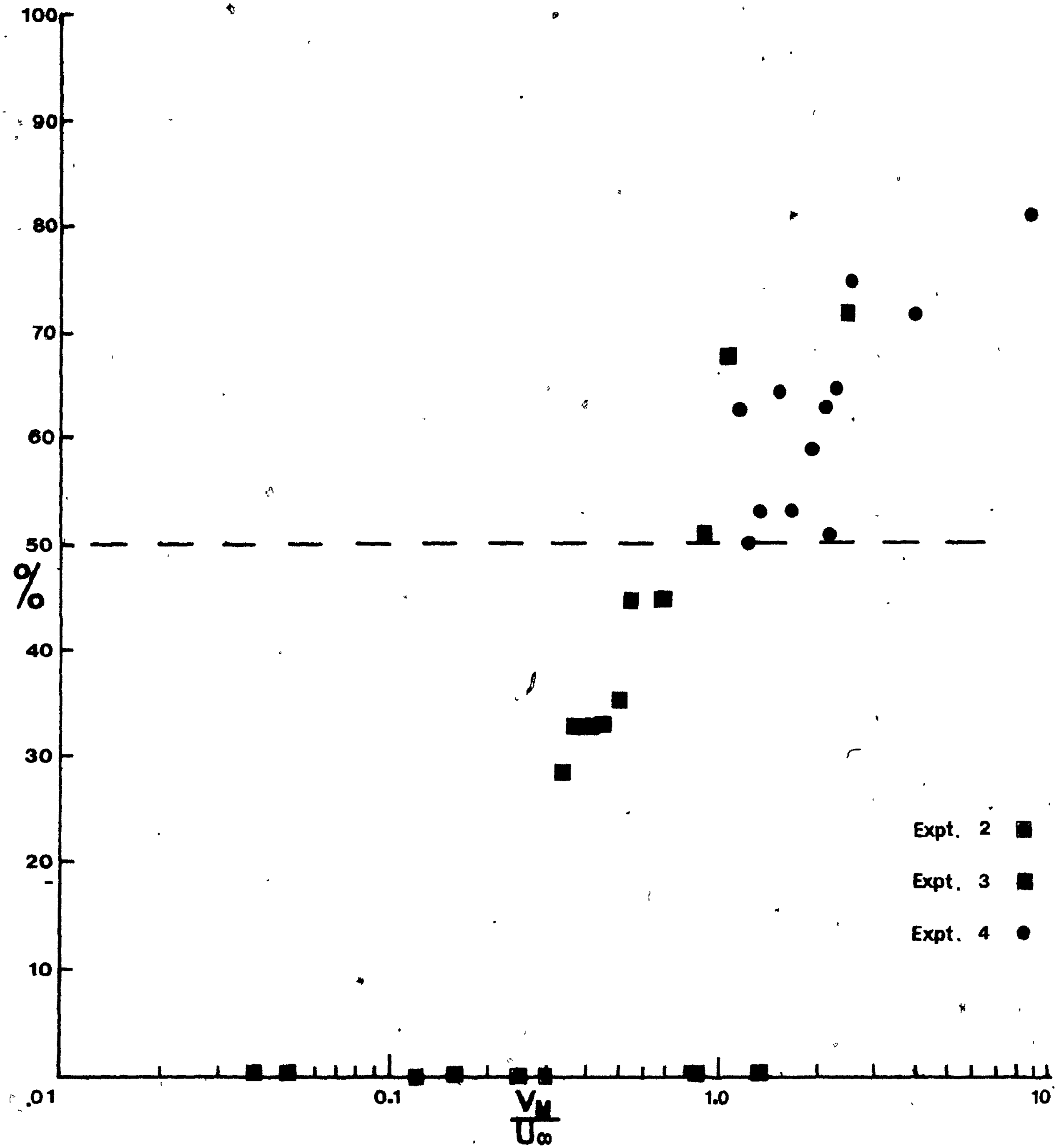

Fig.42 A Graph of % Front Capture versus V_M/U_∞ .

$\varepsilon = 0.5$ and 0.8 respectively, the form of the graphs are adequately described for front and total capture.

Figure 43 and 44 show plots of front and total capture respectively , for the 22 μm hematite and 88 μm manganese dioxide. The estimates by Nesset of 1.0 appears adequate for describing the front capture but total capture may be seen to fitted better with data-fitted values of ε.

In summary, it would appear that above a value of $\frac{V_M}{U_\infty} = 0.9$, front capture is the dominant mechanism whereas if $\frac{V_M}{U_\infty} < 0.9$, back capture assumes dominance. The Loading Number, although not allowing for back capture, describes front and total capture very well when using ε as a data fitted constant.

8.5 The Effect of the Presence of Other Wires on Build-Up Profiles

It is apparent from experiment six that front capture is the dominant capture mode when in competition with back capture. Using Hayashi and Uchiyama's(19) conclusions, the presence of other wires substantially affect the particle trajectories as they pass by the wires. Therefore, it may be that particles are not arriving at the back of the wire due to other wire's influences on the particle trajectories (Figure 10).

Alternatively it may be that the capture radius of the front of the second wire overlaps with that of the back of the first wire. Perhaps just the particles initial direction toward the top of the second wire on entering both capture radii, determines that the particle is

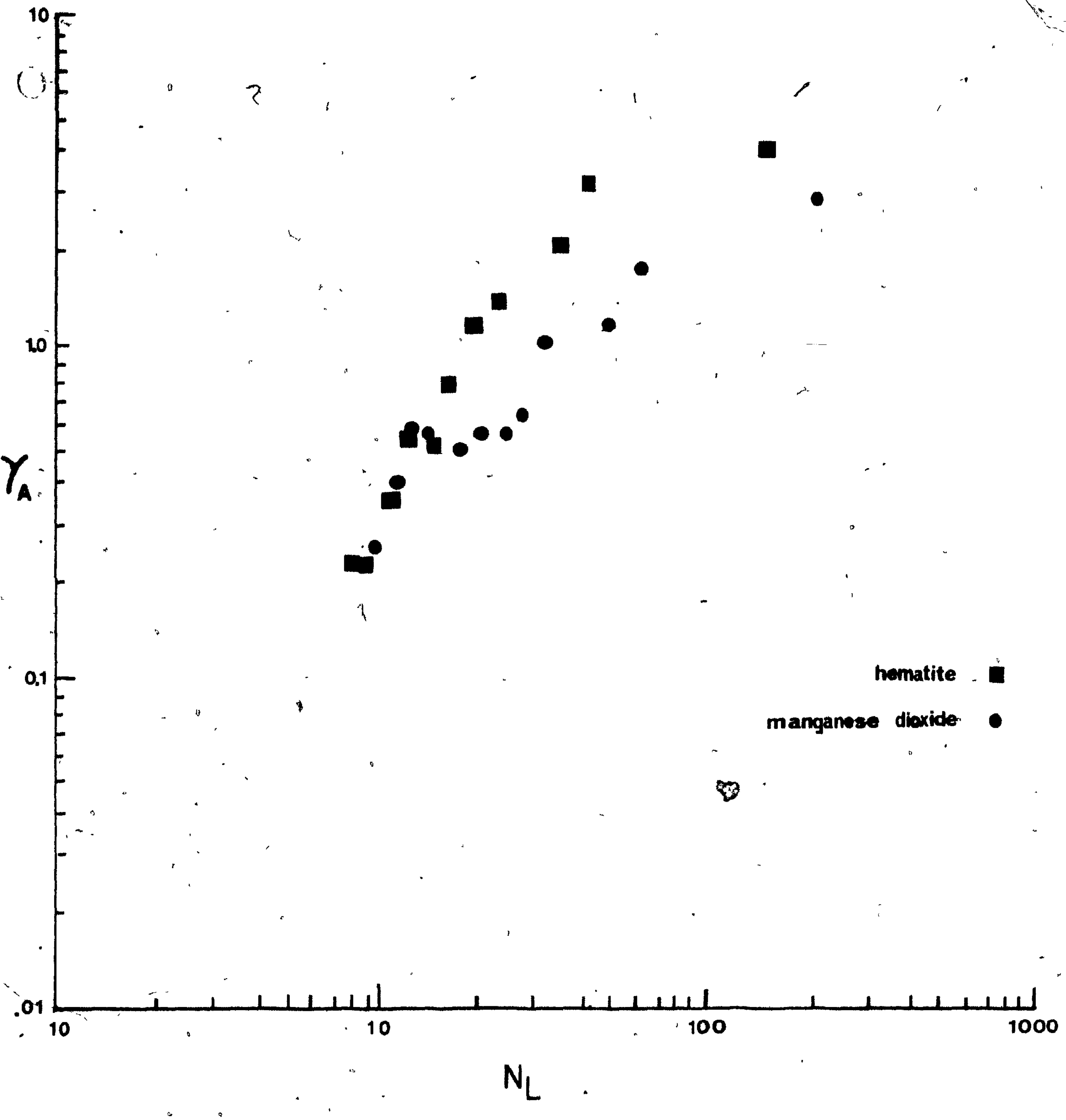

Fig.43 A Graph of Front Capture versus N_L For 22 μm Hematite and 88 μm Manganese Dioxide.

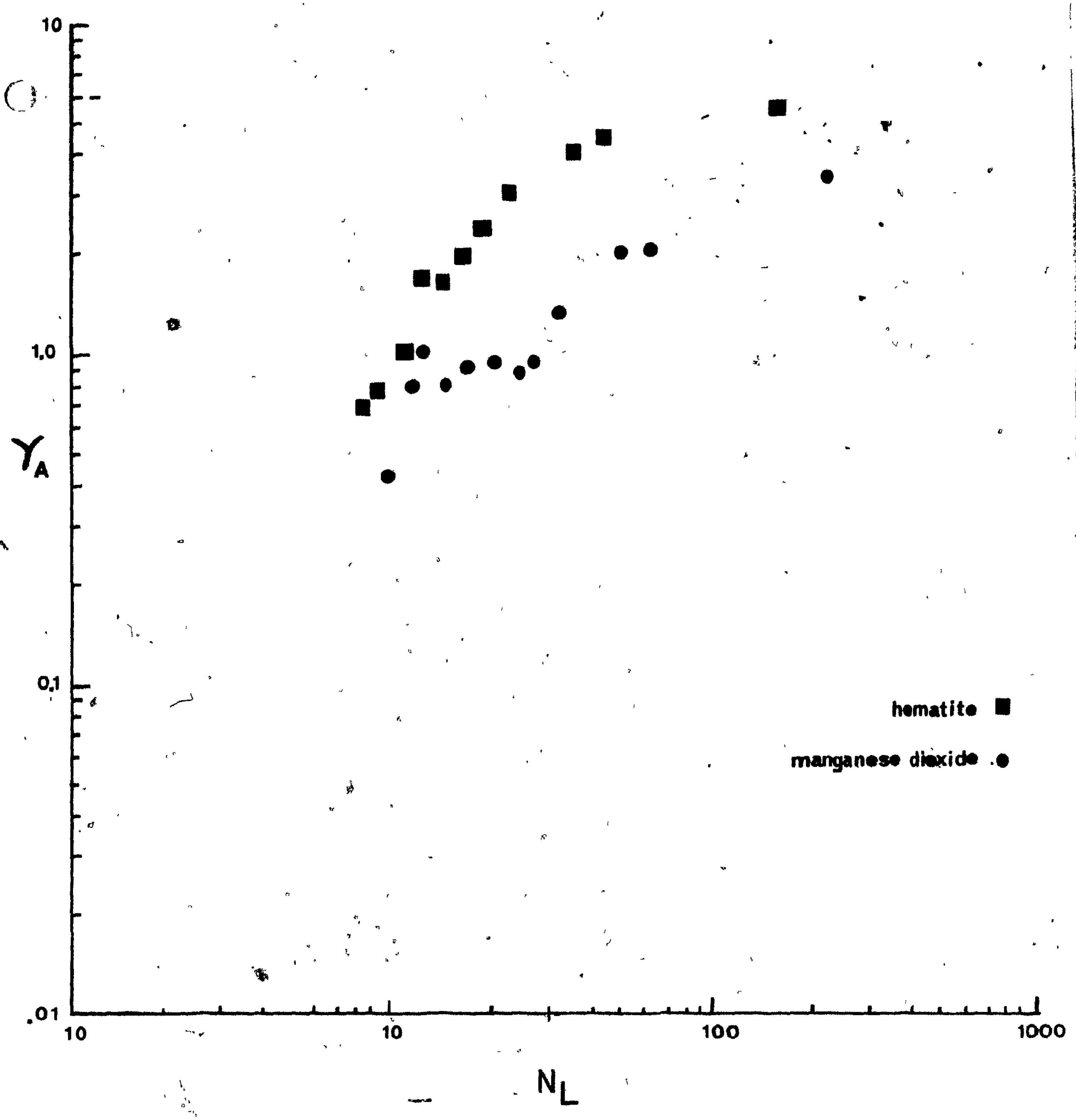

Fig.44 A Graph of Total Capture versus N_L For 22 μm Hematite and 88 μm Manganese Dioxide.

caught on the front of the second wire and not on the back of the first.

8.6 Results of the hgms and Correlation with the Single Wire Work

8.6.1 H.G.M.S.

The hgms results are shown figuratively in Figures 30 and 37, plotted against the Loading Number. The curves drawn on both figures are of the capture predicted by Nesset's Loading Equation with $\varepsilon = 0.7$ (equation 20). The results for the closed matrix, show more material was caught than predicted but they do follow the curve quite well. The open matrices follow a similar type curve but now $\varepsilon \simeq 2.0$, gives a good fit.

Figures 36 and 38 show the loading plotted against $\frac{V_M}{U_\infty}$. The points are slightly more spaced apart yet a reasonable curve could be drawn for each of the matrices. The main disadvantage is that there is no loading equation, consequently once a value of $\frac{V_M}{U_\infty}$ has been found a calibration curve is required to predict loading.

In experiment two, the feed capacity of the closed and open matrices were found to be the same. Irrespective of the amount of material fed to the system the open matrix always caught more material, but on a mass captured/unit volume basis, the closed matrix was the most efficient. There is a suggestion that an open matrix with a very small gap between each layer (e.g. 1 mm) may be more efficient that a closed matrix.

If the grade or recovery of material had been substantially increased, there would have been a good reason for using open matrices and would have helped illuminate the mechanism by which particles are caught at the back of the wire (Section 8.2). Unfortunately, the results suggested no significant difference in grade or recovery.

8.6.2 Correlation Between the HGMS results and the Single Wire Observation

Results obtained in the comparisons of the closed, open (1) and open(2) matrices illustrate that more capture occurs on the open matrices than on the closed matrix under all conditions.

Obviously, correlation between the single wire studies and the hgms results is difficult in a theoretical sense due to the large differences in conditions which exist between the two studies. However, some hypotheses may be put forward.

The reason more capture occurs on an open matrix than on a closed may be because the open matrix more closely approximates a number of single wires. Consequently, one obtains both front and back capture on the wire so increasing total capture. On the closed matrix, it is suggested that little or no back capture occurs due to the close proximity of other wires. It was seen in the "4 wire" single wire study that when front and back capture are in competition, the back capture is diminished (Section 8.4), which is analagous to the conditions existing in the closed matrix.

An alternative suggestion for the increased capture mass is that no physical masking of wires occurs in an open matrix. As discussed by Nesset(34), masking may account for approximately 6% of the capture area, but this would not account for the whole difference in capture between the open and closed matrices.

Another reason for suggesting the open matrix acts as a number of single wires is by considering capture when $\frac{V_M}{U_\infty}$ is greater than 1.0. In the single wire study, all the experiments were at, or approaching a maximum amount of back capture at $\frac{V_M}{U_\infty} > 1$. Only two runs in the hgms experiment had $\frac{V_M}{U_\infty} > 1$, (see Table 9 and Figure 36), these also suggested an apparently constant amount of back capture, by the difference of the open (1) and closed matrices being the same.

Unfortunately, in experiment (1b), $\frac{V_M}{U_\infty} > 1$ was never achieved (Figure 38), so this result was not confirmed. It would appear quite logical that once back capture is fully achieved, increased capture will occur identically on the open and closed matrix and correspondingly there will be a constant difference in the amount of material caught.

IX. CONCLUSIONS AND SUGGESTIONS FOR FUTURE WORK

9.1 Conclusions

1. Both front and back build-up occurs in a single wire study of h.g.m.s.
2. Occurence of front and back capture is governed by the $\frac{V_M}{U_\infty}$ ratio. If $\frac{V_M}{U_\infty} > 0.9$, front capture is the dominant capture mechanism; if $\frac{V_M}{U_\infty} < 0.9$, back capture dominates the capture process.
3. A maximum amount of back capture appears to be obtained, probably governed by $\frac{V_M}{U_\infty}$ or N_L. Above this value, additional capture occurs only on the front of the wire.
4. The loading number, N_L, describes front and total build-up reasonably well, using ϵ as a fitted parameter, not as a packing fraction.
5. The downstream build-up profile may be qualitatively correlated with the fluid behaviour in the wake behind the wire.
6. The front build-up profile is seen to be generally as predicted by Nesset (34).
7. A spaced matrix will catch more material per unit mass of matrix than a closed matrix, but, on a volume of matrix basis, efficiency is lower.
8. The feed capacity of the spaced matrix is no larger than that of a closed matrix.

9.2 Suggested Future Work

1. An attempt to use slow exposure times should be made in order to track particle trajectories as they move toward the wire, in order to examine the mechanisms of back capture.
2. More hgms work should be carried out in correlation with the single wire studies, e.g. investigation of the $\frac{V_M}{U_\infty}$ region which produces the maximum back build-up on the single wire.
3. Grade/Recovery work should be further investigated, under various test conditions, in order to examine the mechanism of back capture. Larger matrices and feed masses should be used.

ACKNOWLEDGEMENTS

The author wishes to express his sincere appreciation to Prof. J.A. Finch for all his guidance, patience and support throughout this research study.

Special thanks are also due to Mr. R. Selback and J. Goldsmith of the Instructional Communications Centre (I.C.C.), here at McGill, without whose assistance this research would not have been possible.

In addition, the technical assistance of M. Leroux, M. Riendeau, M. Knopfel and other staff members of the Department of Mining and Metallurgical Engineering, McGill University, is gratefully acknowledged.

Finally, the use of the Sala 10-15-20 laboratory separator at CANMET, Ottawa and financial assistance from the ALCAN Scholarship are also gratefully acknowledged.

REFERENCES

1. Watson, J.H.P., J. Appl. Phys., 44, 1973, p. 4209.
2. Nesset, J.E., Finch, J.A., A Loading Equation for High Gradient Magnetic Separators and Application in Identifying the Fine Size Limit of Recovery, Fine Particles Processing, Vol. 2, Somasundaran, P., (Ed.) AIME, 1980, pp. 1217 - 1241
3. Oberteufer, J.A., Wechscer, I., Recent Advances in High Gradient Magnetic Separation, Industrial Applications of Magnetic Separation, Lui, Y.A., (Ed.) IEEE Publication No. 78CM1447 - 2 Mag., New York, (1979), pp 1178 - 1179.
4. Yano, J., Eguchi, I., as Ref. 3, pp. 134 - 136
5. Oberteuffer, J.A., Wechsaer, I., Marston, P.G., McNallon, M.J., IEEE Trans. Mag., Vol. Mag - 11, No. 5, Sept. 1975, p. 1591.
6. Oder, R.R., Proc. HGMS Symposium, M.I.T., May 22, 1973, (Eds.) Oberteuffer, J.A., Kelland, D.R., p. 55.
7. Price, C.R., Abercrombie, W.F., as Ref 3, pp. 14 - 16.
8. Melville, D., Paul, F., Roath, S., IEEE Trans. Mag. Vol. Mag - 11, 1975, p. 1701.
9. Zebel, G.J., Colloid Sci., <u>20</u>, 1965, p. 522.
10. Luborsky, F.E., Drummond, B.J., IEEE Trans. Mag. Vol. Mag - 11, 1975, p. 1696.
11. Luborsky, F.E., Drummond, B.J., IEEE Trans. Mag. Vol. Mag - 12, 1976 p. 463.
12. Cummings, D.L., Prieve, D.C., Powers, G.J., IEEE Trans. Mag. Vol. Mag - 12, 1976, p. 471.

13. Clarkson, C.J., Kelland, D.R., King, T.B., IEEE Trans. Mag. Vol. Mag - 12, 1976, p. 901.

14. Clarkson, C.J., Kelland, D.R., IEEE Trans. Mag. Vol. Mag - 14, 1978, p. 97.

15. Lawson, W.F., Simons, W.H., Treat, R.P., J. Appl. Phys., <u>48</u>, 1977, p. 3213.

16. Stekly, Z.J.J., Minervini, J.V., IEEE Trans. Mag., Vol. Mag - 12, 1976, p. 463.

17. Cummings, D.L., Himmelblau, D.A., Oberteuffer, J.A., Powers, G.J., ALCHE Journal, <u>22</u>, No. 3, May 1976, p. 569.

18. Birss, R.R., Dennis, B.J., Gerber, R., IEEE Trans. Mag, Vol. Mag - 15, Sept. 1979, p. 1362.

19. Hayaski, K., Uchiyama, S., IEEE Trans. Mag., Vol. Mag - 16, Sept. 1980.

20. Watson, J.H.P., IEEE Trans. Mag., Vol. Mag - 15, November, 1979.

21. Himmelblau, D., Observation and Modelling of Paramagnetic Particle Theses, June, 1973. (From Ref. 10)

22. Schlichting, H., 'Boundary Layer Theory', McGraw-Hill, 1968, p. 26.

23. Watson, J.H.P., Filtration and Separation, May/June, 1977, p. 242.

24. Watson, J.H.P., presented at 'A Symposium on Deposition and Filtration of Particles from Gas and Liquids' at Loughborough University, England, Sept. 1978.

25. Cowen, C., Friedlaender, F.J., Jaluvia, R., IEEE Trans. Mag., Vol. Mag - 11, 1975, p. 1600.

26. Cowen, C., Friedlaender, F.J., Jaluvia, R., IEEE Trans. Mag., Vol. Mag - 12, 1976, p. 466.

27. Cowen, C., Friedlaender, F.J., Jaluvia, R., IEEE Trans. Mag., Vol. Mag - 12, 1976, p. 898.

28. Cowen, C., Friedlaender, F.J., Jaluvia, R., IEEE Trans. Mag., Vol. Mag - 13, 1977, p. 1483.

29. Friedlaender, F.J., Takayasu, M., Rettig, J.B., Kentzer, C.P., IEEE Trans. Mag., Vol. Mag - 14, Sept. 1978.

30. Friedlaender, F.J., Takayasu, J., Rettig, J.B., Kentzer, C.P., IEEE Trans. Mag., Vol. Mag - 14, Nov. 1978.

31. Friedlaender, F.J., Takayasu, M., 'Video Recording of Particle Trajectories and Build-up of Single Wires in High Gradient Magnetic Separation', preprint of paper, 1979.

32. Liu, Y.A., Oak, M.J., Lin, C.J., paper for publication in the Chemical Engineering Progress Technical Manual, 'Coal Processing Technology' presented at Symposium on Novel Separation Techniques, Seventh Annual AIChE Meeting, Nov. 13-17, 1977, N.Y.

33. Nesset, J.E., Todd, I.A., Hollingworth, M., Finch, J.A., IEEE Trans. Mag., Vol. Mag - 16, Sept. 1980.

34. Nesset, J.E., 'A Static Model of High Gradient Magnetic Separation', McGill Masters Theses, March 1980.

35. Th. Von Karman, Uber den Mechanismus des Widerstandes, der ein bewegter Korper in Einer Flussigkert erzeugt. Nachr. Ges. Wiss. Gottingen, Math. Phys. Klasse (1911), 509-517 and (1912), 547-556; also Coll. Works 1, 324-338.

36. V. Strouhal, Uber eire besondere Art der Tonerregung. Ann. Phys. and Chemie. New Series, vol 5, pp. 216-251, (1978)

37. Roshko, A., On the Development of Turbulent Wakes from Vortex Streets. NACA Rep. 1191, (1954).

38. Clift, R., Grace, J.R., Weber, M.E., Bubbles, Drops and Particles, Academic Press Inc., 1978.

39. Brauer, I.H., Movement of Single Particles in Various Flow Fields, pre-print 1980, to be published in 'Advances in Transport Processes'.

APPENDIX Ia - THEORY OF THE HALL PROBE

This device is one of the most common and versatile devices for measuring magnetic fields (Figure 45). On insertion of the Hall probe into the unknown magnetic field, a constant current is fed into two of the four wires, attached across the probe. The "Hall potential" is measured across the remaining two wires, caused by the deflection of electrons in the conductor by the magnetic field.

With the field vector, $\hat{B}$, making an angle, θ , with the unit vector normal to the plate, $\hat{n}$, when a current, I_c, is applied to the conductor, the Hall potential would be given by:

$$V_H = \frac{R_H}{t} \quad I_c(\hat{n} \quad \hat{B}) \qquad \text{(in volts)} \tag{29}$$

where R_H = Hall constant.

For a given Hall crystal, i.e. with fixed R_H , t and I_c, this voltage becomes a measure of the magnetic field strength. Thus, by rearranging equation (29):

$$H = \frac{V_H}{K_1 \quad I_c \quad \cos\theta} \tag{30}$$

Consequently, before measurement of an unknown magnetic field can be carried out, it is necessary to calibrate the Hall Probe against a known magnetic field in order to determine K_1 (Figure 46).

The Hall probe was positioned in the gap between the pole of a magnet such that θ was equal to zero, Equation (30) becoming:

$$H = \frac{V_H}{K_1 \quad I_c} \tag{31}$$

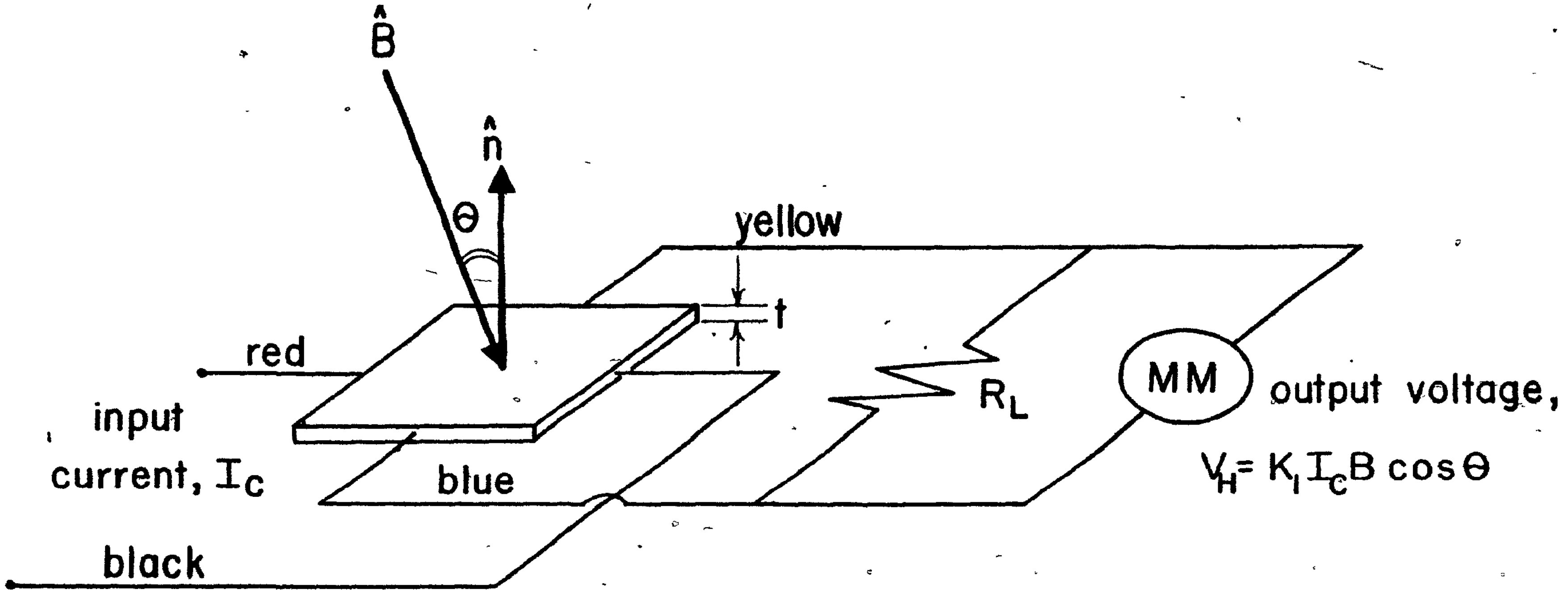

Fig.45 The Hall Effect Probe.

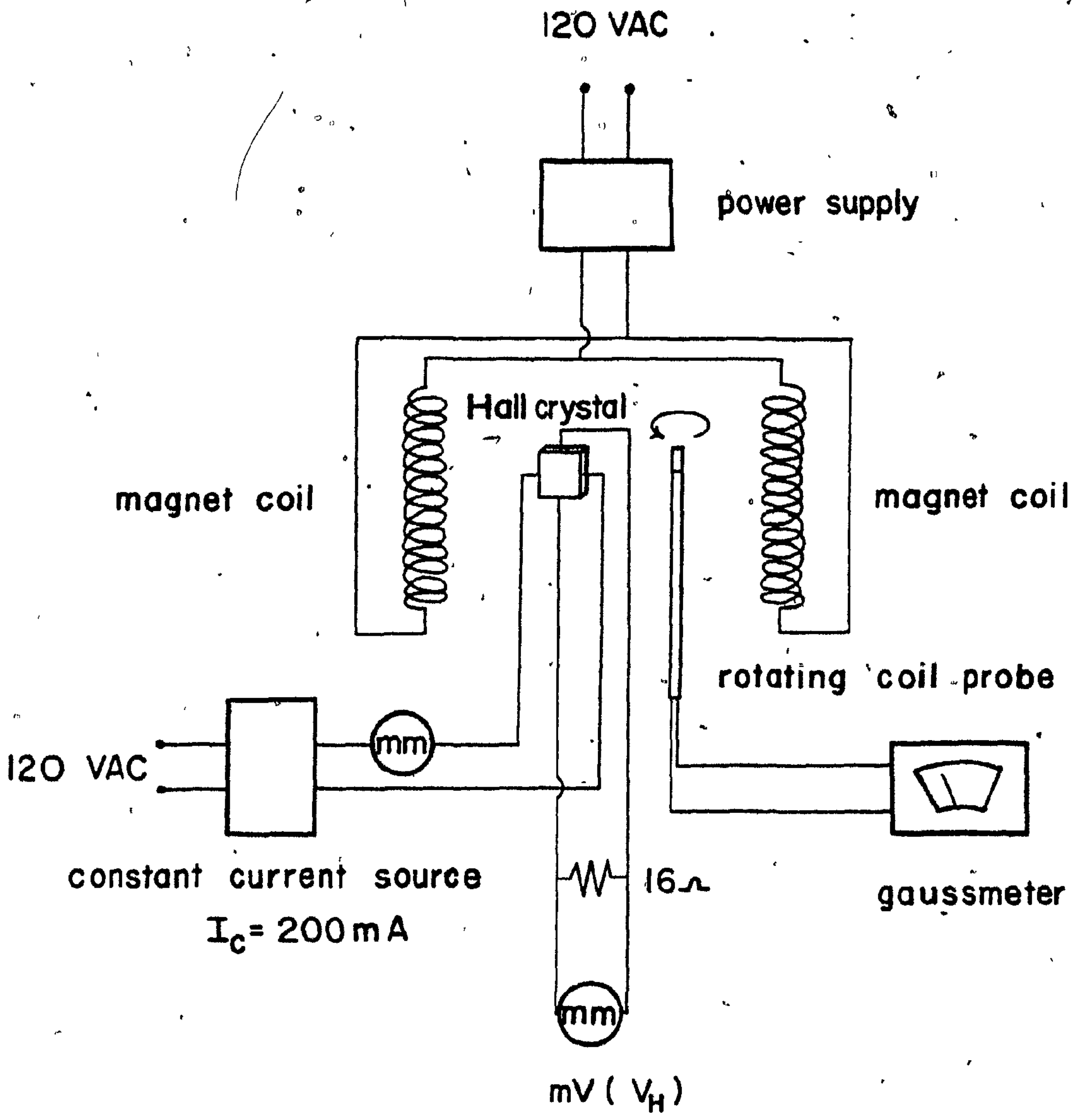

Fig.46 Schematic of Calibration Set-up for the Hall Probe.

A direct current, I_c, of 200(±1) mA was applied to the probe and the field between the poles was increased while V_H was measured on a voltmeter applied across the probe. The value of the field was measured accurately using a moving coil gaussometer. By linear regression, the relationship is:

$$H(Oe) = 24.16 \times \text{volts} \quad (\pm 28.84) \qquad (32)$$

This linearity between V_H and H is generally good to within 1%, up to 10 KOe, well within the range of this investigation.

Having obtained the value of K_1, the Hall probe was used in order to calibrate the value of the magnetic field between the two newly designed pole pieces attached to the Frantz.

APPENDIX Ib – CALIBRATION OF THE MAGNETIC FIELD USING THE HALL PROBE (AT THE CENTRE OF THE DRILLED HOLE)

Input Current To The Frantz mA	Magnetic Field KOe
100	.48
200	.87
300	1.28
400	1.69
500	2.12
600	2.52
700	2.94
800	3.33
900	3.73
1000	4.14

APPENDIX II - PARTICLE SIZING USING THE WARMAN CYCLOSIZER

The Warman Cyclosizer is a hydraulic cyclone elutriator which consists of five cyclones in series which separates the feed material into a roughly $\frac{1}{\sqrt{2}}$ decreasing series of five sizes, in the sub-sieve range (80-5μm) (Figure 47).

The unit is pre-calibrated to produce a cut-off size for each cyclone, d_∞ , based on a silica sample, infinite elutriation time and a set of standard operating conditions for the equipment.

Correction factors are then necessary for particular operation conditions, viz, water temperature (f_1), specific gravity (f_2), flow rate ($f3$) and operation time (f_4). The correction factors then produce a set of actual cut-off diameters, d_a , for each of the cones, under any conditions viz;

$$d_a = d_\infty \; f_1 \quad f_2 \quad f_3 \quad f_4$$

A geometric mean size is obtained for each cyclone, defined as:

$$dgm_{(n)} = \left[da_{(n)} \times da_{(n-1)} \right]^{\frac{1}{2}} \qquad (34)$$

where n =cyclone number

Method of Operation

About 50 grams of material may be run through the cyclosizer at one time, ensuring less than 15 grams of material are sized into any one core.

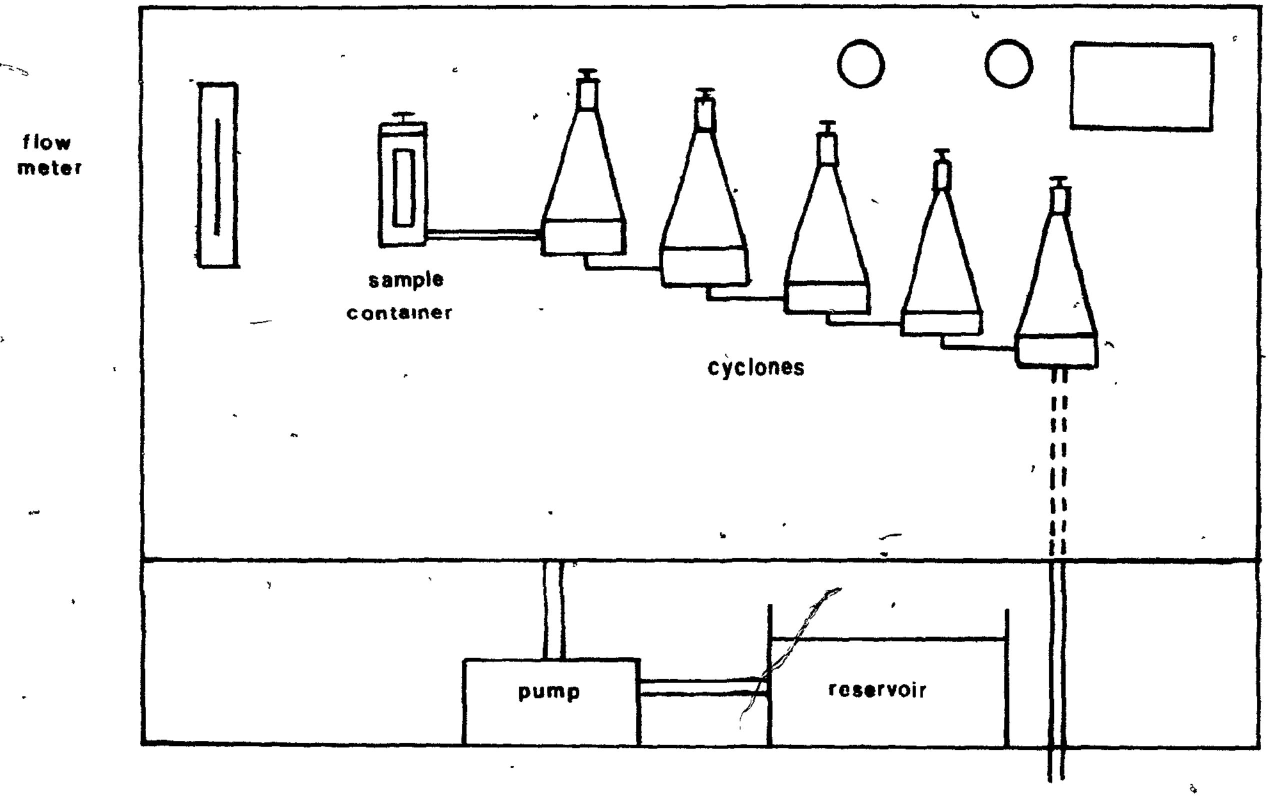

Fig.47 The Warman Cyclosizer.

The sample was first pulped with 50 - 150 mls. of water, and was then poured into the sample container (Figure 46). The container was then filled up to a level of half-way up the outside taper to ensure no air was allowed in the system.

The container valve was then closed and it was returned to the holder on the cyclosizer. The cyclosizer pump was turned on and with the flow control valve fully open, all air was removed from each cyclone by opening the apex valves.

Then, with the control valve remaining fully open, the sample container valve was slowly opened. Consequently, the sample was then allowed to completely empty from the container.

After a period of approximately three minutes, the control valve was closed until the flow meter indicated the required elutriating flow.

The cyclosizer was then left for 15-20 minutes. The control valve again fully opened. Beginning at cyclone 5, the apex valve was opened on each cyclone and the solid discharges were collected in a beaker. All 5 cyclones were treated similarly.

This procedure was repeated a number of times, until sufficient material had been prepared for all the experiments

APPENDIX III - OPERATION OF THE DAVIS TUBES

The Davis tube uses magnet pole pieces which generate about 1 KOe magnetic field. On passing slurried particles between these pole pieces in an agitated glass tube, the field is strong enough to capture magnetite but the hematite flows past.

The water in the tube is kept at a constant height, above the pole pieces, by a feed pipe placed in the end of the tube. If the water level drops below the pole pieces, the magnetite tends to be dragged downstream.

The sample is fed into the tube by means of a funnel in the top end of the tube. The agitator is then started as the particles flow down toward the pole pieces. This prevents physical trapping of hematite within the captured magnetite.

The cleaned hematite is consequently collected in a bucket, decanted, and dried.

APPENDIX IV

The preparation of the 5 μm hematite for experiment five, required previously prepared cone #5 material to be ground in a wet ball mill for four hours in order to achieve the required size range.

Separation of a size range of 3 - 7 μm particles was achieved by allowing the particles to settle out. This separation was carried out using the equation:

$$D = KV^{\frac{1}{2}} \qquad (35)$$

where D= Diameter of the particle

V= velocity

and

$$K = \left[\frac{18\eta}{(\rho - \rho_o)g}\right]^{\frac{1}{2}} \qquad (36)$$

where η = .01

ρ = 5.25

ρ_o = 1.00

g = 9.80

Thus,

$$D = .006571 \ V^{\frac{1}{2}} \qquad (37)$$

<u>For 7 μm Material</u>

$$7.10^{-4} = .006571 \ . \ V^{\frac{1}{2}}$$

giving

$$V = .011348 \text{ cm/s}$$

Consequently, any material that has not settled 13.6 cm in 20 minutes is < 7 μm , and was collected.

For 3 μm Material

$$3.10^{-4} = .06571 \; . \; V^{\frac{1}{2}}$$

giving

$$V = .006571 \text{ cm/s}$$

Consequently, material collected of size <7μm and >3μm would have settled lower than 7.5 cm in 60 minutes and so, material of 3 - 7 μm was obtained.

APPENDIX V - TECHNICAL PHOTOGRAPHIC DATA

A Nikon F camera was used with a Nikon PB bellows set at a 1:2 magnification ratio. The lens used was Nikkor 3.5 Macro lens set at infinity. Ilford H.P.5, 35 mm film rated at 650 ASA and shot at $^1/8$ - $^1/15$ seconds at F.32 or .22.

The lighting consisted on a 100 watt fill light, with a total light at 1000 wats angled at the side.

APPENDIX VI - CALIBRATION OF THE PERISTALTIC PUMP

The pump was calibrated by setting the "Masterflex" control to 5.0, and then by the amount of water pumped in a certain time with the variation of the variac controller. This was done before each experimental series, therefore, slight variations will exist in the flow rate in each series.

Variac Position	Volume of Water (ml)	Time (s)	Flow Rate cm/s
30	1215	145	13.17
28	945	120	12.38
26	888	125	11.17
24	840	135	9.78
22	865	170	7.99
20	738	180	6.44
19	730	240	4.78
18	625	240	4.09
17	410	360	1.79

APPENDIX VII - THE DIGITIZER

The Digitizer basically consists of four components, (Figure 48):

a) The display console which houses most of the electronic circuits for translation and calculation of data.

b) The reading head contains the carriage and the optical pick-up system for detecting carriage movement along the x-axis.

c) The traverse arm, which is moved by the operator in the y-axis. The magnifying cursor is attached to the end of the traverse arm.

d) The keyboard which controls the operation of the Digitizer.

In order to measure the area of build-up on the wire, a trace of the profile was first made as definition was lost on looking at the photograph directly through the magnifying glass.

The cross-wires were then positioned on a selected starting point. Button "A" was then pressed on the keyboard in order to zero the area register.

The Digitizer now measures any movement of the cursor. Consequently, the area of build-up was then traced. On reaching the starting point once more "Y" and "A" were pressed simultaneously to display the measured area.

The bare wire area, top build-up and back build-up were consequently easily measured.

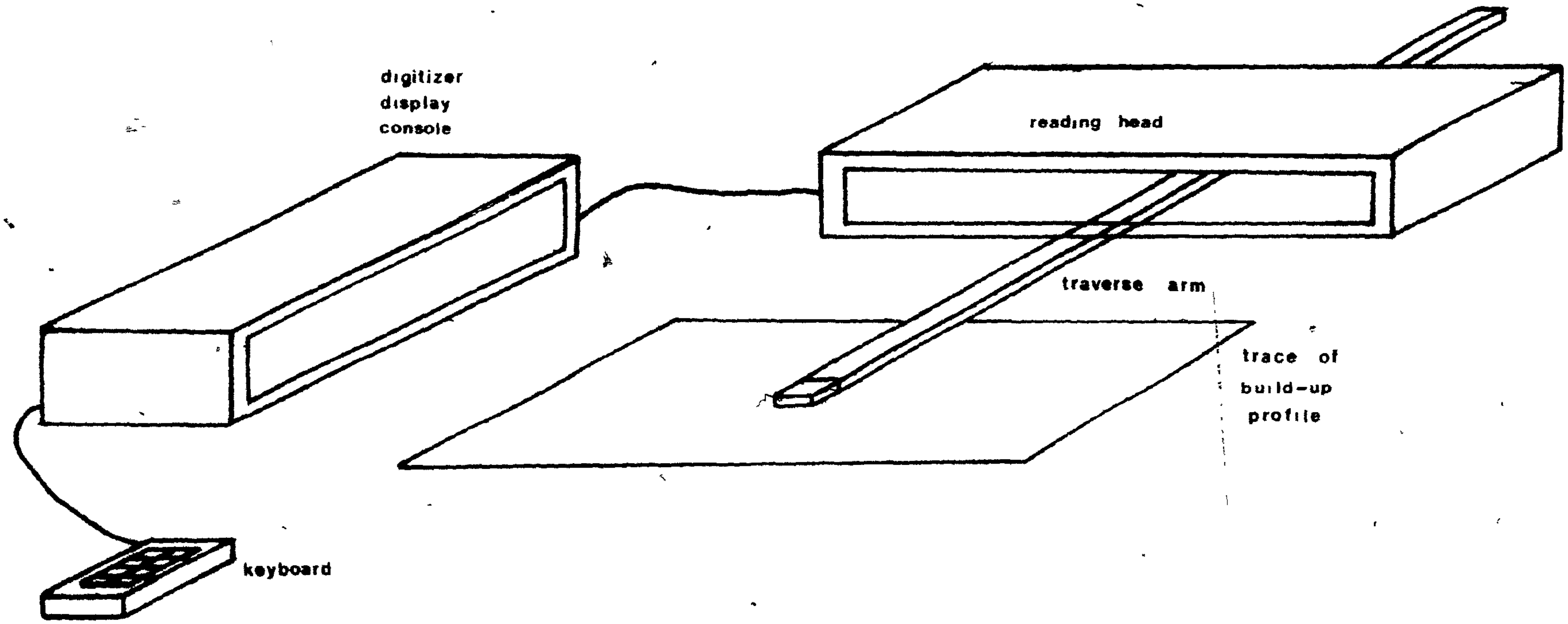

Fig.48 The Electronic Digitizer.

APPENDIX VIII - RESULTS OF THE QUANTITATIVE SINGLE WIRE ANALYSIS

Material and cone size	Field KOe	Flow cm/s	MASS COLLECTED (grams)				
			30s	60s	90s	120s	180s
MnO_2 #4	1.2	.62	–	.0023	–	.0037	.0026
	2.4	.62	–	–	.0089	.0039	.0020
	3.5	.62	–	.0046	.0181	.0066	.0167
	3.5	7.1	.0024	.0088	.0046	.0047	–
	4.6	.62	–	.0092	.0064	.0047	–
	4.6	7.1	–	.0106	.0024	.0043	–
MnO_2 #2	3.5	7.1	.0095	.0102	.0081	–	–
	4.6	7.1	.0071	.0057	.0150	.0110	–
Fe_2O_3 #4	0.6	.61	.0020	.0043	–	.0080	–
	1.2	.61	–	.0027	–	.0053	.0065

APPENDIX IX - EXPERIMENT ONE (b)

MATERIAL AND CONE SIZE	Flow Rate cm/s	Field Strength KOe	N_L	$\gamma_m \cdot W$ (gms)	Closed Matrix (gms)	Open (1) Matrix (gms)	Open (2) Matrix (gms)
MnO_2 #4	2.17	1.69	5.34	0.53	0.26	0.64	0.54
Fe_2O_3 #4	2.17	0.89	9.14	1.22	2.01	2.67	2.38
MnO_2 #2	2.17	1.69	10.41	1.28	0.88	2.94	2.49
Mno_2 #2	0.81	0.89	13.54	1.83	2.41	2.94	2.60
Fe_2O_3 #2	2.17	0.89	18.56	2.64	5.1	8.68	8.37
MnO_2 #3	1.15	1.69	19.44	2.66	3.02	5.23	5.86
Fe_2O_3 #4	1.15	0.89	26.23	3.70	4.4	5.85	6.30
Fe_2O_3 #3	2.17	1.69	31.96	4.46	3.79	12.35	12.06
Fe_2O_3 #3	1.15	0.89	36.58	5.04	5.7	10.45	11.6
Fe_2O_3 #2	2.17	1.69	42.45	5.76	9.41	15.71	20.18

APPENDIX IX (b) - EXPERIMENT ONE (b)

Material and Cone Size	Flow Rate (cm/s)	Field Strength KOe	V_M/U_∞	γ_V		
				Closed Matrix	Open (1) Matrix	Open (2) Matrix
MnO_2 #4	2.17	1.69	.05	.07	.18	.15
MnO_2 #2	0.81	0.89	.10	.66	.81	.70
Fe_2O_3 #4	2.17	0.89	.14	.53	.71	.61
MnO_2 #2	2.17	1.69	.18	.24	.81	.70
Fe_2O_3 #4	1.15	0.89	.18	1.15	1.55	1.63
MnO_2 #3	1.15	1.69	.19	0.83	1.44	1.8
Fe_2O_3 #3	2.17	1.69	.33	0.99	3.27	3.11
Fe_2O_3 #2	2.17	0.89	.34	1.34	2.30	2.16
Fe_2O_3 #3	1.15	0.89	.35	1.49	2.77	2.99
Fe_2O_3 #2	2.17	1.69	.75	2.47	4.16	5.21

APPENDIX X - EXPERIMENT THREE
GRADE EXPERIMENTS

OPEN MATRIX

	MAGS	N-MAGS	GRADE % Fe_2O_3	RECOVERY % Fe_2O_3
1)	2.63	3.56	78.52	58.31
2)	2.46	3.14	80.62	63.87
3)	2.36	3.21	79.64	62.05
4)	2.27	3.21	80.42	60.60

CLOSED MATRIX

	MAGS	N-MAGS	GRADE % Fe_2O_3	RECOVERY % Fe_2O_3
1)	2.33	3.29	79.28	64.42
2)	2.32	3.28	81.11	63.30
3)	2.11	3.40	84.78	59.67
4)	2.20	3.35	82.17	58.20

APPENDIX XI - V_m/U_∞ CALCULATIONS

The aim of experiment five, was to obtain build-up profiles under conditions such that the V_m/U_∞ ratio would be similar to or less than that of experiment two.

23μm Manganese Dioxide

$$V_M/U_\infty = \frac{4}{9}\ \frac{b^2\ Ha^2\ A\ \kappa}{U_\infty\ \eta\ \rho a}$$

$$= \frac{4}{9}\ \frac{(11.78.10^{-4})^2\ \ 4100^2\ \ .89\ \ .000117}{U_\infty\ \ .01\ \ .045}$$

Consequently:

$$V_M/U_\infty = 2.40/U_\infty$$

.5 Hematite

$$V_M/U_\infty = \frac{4}{9}\ \frac{(2.5.10^{-4})^2\ \ 3500^2\ \ .89\ \ .000308}{U_\infty\ \ .01\ \ .045}$$

Therefore:

$$V_M/U_\infty = 0.21/U_\infty$$